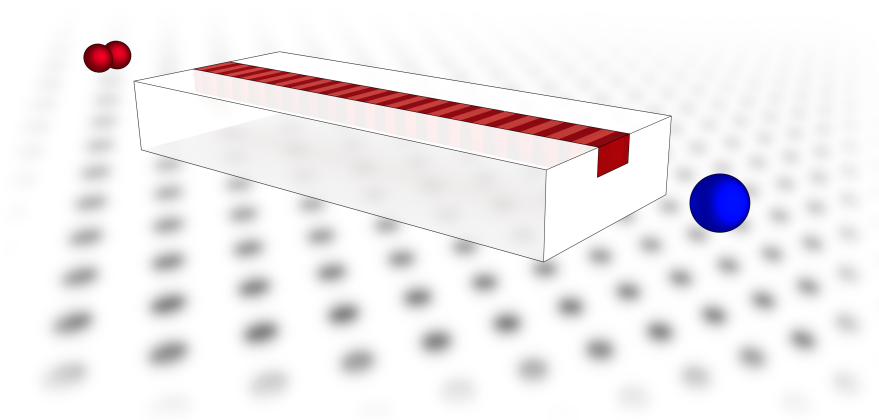


Periodically Poled Waveguides in Potassium Titanyl Phosphate:

From Technology Development to Applications



Der Naturwissenschaftlichen Fakultät
der Universität Paderborn
zur Erlangung des Doktorgrades
Dr. rer. nat.
vorgelegt von

CHRISTOF EIGNER

aus Brilon

2019

Contents

1	Summary	1
2	Zusammenfassung	3
3	Preface	5
4	Introduction	9
5	Fundamental Theory	13
5.1	Nonlinear Optics	13
5.1.1	Nonlinear Polarisation	14
5.1.2	Second Order Nonlinearity	14
5.1.3	Coupled Wave Equations	15
5.2	Phase Matching	17
5.2.1	Birefringent Phase Matching	17
5.2.2	Quasi-Phase Matching	18
5.2.3	Second Harmonic Generation	21
5.3	Potassium Titanyl Phosphate	23
5.3.1	Crystallographic Structure	23
5.3.2	Non-stoichiometric KTP	25
5.3.3	Ionic Conductivity	26
5.4	Domain Inversion	27
5.4.1	Curie Temperature	27
5.4.2	Spontaneous Polarisation and Optical Nonlinearity	28

5.4.3	Polarisation Reversal and Ferroelectric Domains	29
5.4.4	Coercive Field Strength	31
5.5	Rubidium Doping of KTP	32
5.6	Optical Properties	34
5.6.1	Gray Tracking	35
5.6.2	Material Dispersion	36
6	Technology	39
6.1	State of the Art: Periodically Poled Waveguides in KTP	39
6.1.1	Poling Techniques	40
6.1.2	Waveguide Fabrication Techniques	45
6.1.3	Characterisation Techniques	46
6.2	In-house Processing	48
6.2.1	Chosen Technologies	48
6.2.2	Periodic Poling	48
6.2.3	Waveguide Fabrication	53
6.2.4	Channel Waveguides	56
6.2.5	Ridge Waveguides	60
6.3	Poled Waveguide Results	61
6.3.1	Doped and Undoped Bulk KTP Properties	61
6.3.2	Sequence of Sample Fabrication	69
6.3.3	Poling after Waveguide Fabrication	69
6.3.4	Poling prior to Waveguide Fabrication	78
6.3.5	Comparison of the Fabrication Results	83
7	Coatings	85
7.1	Optical Dielectric Coatings	85
7.2	Optical Coating Designs	87
7.3	Optical Coating Techniques	89
7.4	Our Coating Facility	92
7.4.1	Broad Band Monitoring	93
7.4.2	Realised Coatings	95
7.4.3	Novel Types of Dielectric Coatings	100

8	Applications	105
8.1	Spatial Single Mode Sources at 800 nm	105
8.1.1	KTP Sources in the Visible Regime	106
8.2	Ridge Waveguides	106
8.2.1	State of the Art: Ridge Waveguides	106
8.2.2	Ridge Waveguide Modelling	107
8.2.3	Ridge Waveguide Fabrication	110
8.2.4	Optical Characterisation of Ridge Waveguides	111
8.3	Channel Waveguides	119
8.3.1	Channel Waveguide Modelling	119
8.3.2	Channel Waveguide Fabrication	121
8.3.3	Optical Characterisation of Channel Waveguides	123
8.4	Application Discussion	131
9	Summary and Outlook	133
9.1	Summary	133
9.2	Outlook	134
10	Acknowledgements	137
A	Appendix	139
A.1	Patents	139
A.2	Publications	139
A.3	Conference Contributions	142
B	References	143

Summary

Integrated quantum optics is an emerging research field that offers scalable approaches towards exciting new applications such as quantum simulation. The basis for all integrated quantum optics applications is, obviously, the integrated devices, which must exhibit supreme sample quality and replicability.

In this thesis, we developed and established a novel technology for the fabrication of tailored, periodically poled waveguides in potassium titanyl phosphate (KTP), a material that is of high interest due to its unique dispersion properties and, at the same time, exquisitely challenging for fabrication. We conducted detailed studies of the properties of KTP, which led to a better understanding of the material behaviour during the manufacturing. These results allowed us to fuse electric field-enhanced domain inversion and potassium-rubidium-exchanged waveguides to enable the production of periodically poled KTP waveguides.

We further established a coating technology, which facilitates the deposition of engineered dielectric coatings on waveguide end facets and other substrates. The coatings are based on oxygen ion assisted electron beam evaporation and integrated broadband monitoring, and we demonstrate tailored, multifunctional coatings.

We used the new technologies to realise two new devices for frequency conversion between UV and visible wavelengths: periodically poled KTP ridge and channel waveguides. Both devices were thoroughly characterised, and we demonstrated both second harmonic generation and parametric down-conversion with high efficiencies. The results of our thesis will help to advance the field of integrated quantum optics by providing important progress in the technology, which lies at the heart of all applications.

2

Zusammenfassung

Die integrierte Quantenoptik ist ein aufstrebendes Forschungsfeld, das skalierbare Ansätze für neue Anwendungen wie die Quantensimulation bietet. Die Basis für alle Anwendungen der Quantenoptik sind die integrierten Bauelemente, die höchste Probenqualität und Reproduzierbarkeit aufweisen müssen.

In dieser Arbeit wurde eine neuartige Technologie zur Herstellung maßgeschneiderter, periodisch gepolter Wellenleiter aus Kaliumtitanylphosphat (KTP) entwickelt und etabliert, ein Material, das aufgrund seiner einzigartigen Dispersionseigenschaften von großem Interesse ist aber gleichzeitig eine besondere Herausforderung an die Herstellung stellt. Es wurden detaillierte Untersuchungen zu den Eigenschaften von KTP durchgeführt, welche zu einem besseren Verständnis des Materialverhaltens während der Prozessierung führte. Diese Ergebnisse erlaubten es, die durch elektrische Felder erzeugte Domäneninversion und durch Kalium-Rubidium ausgetauschte Wellenleiter zu kombinieren, um die Herstellung periodisch gepolter KTP-Wellenleiter zu ermöglichen.

Des Weiteren konnte eine Beschichtungstechnologie etabliert werden, die die Abscheidung dielektrischer optischer Beschichtungen auf Wellenleiter-Endflächen und anderen Substraten ermöglicht. Die Beschichtungen basieren auf Sauerstoffionen-unterstützter Elektronenstrahlverdampfung und integrierter Breitbandüberwachung. Es konnten maßgeschneiderte multifunktionale Beschichtungen hergestellt werden.

Unter Verwendung der neuen Technologien wurden zwei neuartige Bauelemente für die Frequenzkonversion zwischen UV- und sichtbaren Wellenlängen realisiert: periodisch gepolte KTP Rippen- und Kanalwellenleiter. Beide Bauelemente wurden optisch charakterisiert, und zeigen sowohl in der Erzeugung der zweiten Harmonischen als auch der parametrischen Fluoreszenz einen hohen Wirkungsgrad. Die Ergebnisse dieser Arbeit werden dazu beitragen, das Gebiet der integrierten Quantenoptik voranzubringen, indem wichtige Fortschritte in der Technologie erzielt werden, die im Mittelpunkt aller Anwendungen steht.

3

Preface

This work has been performed during the years 2013-2018 in the integrated quantum optics group of Prof. Christine Silberhorn at Paderborn University. The original theme of this thesis and the starting point of the work was the fabrication of tailored periodically poled waveguides in KTP, which were not commercially available.

The technology lays the foundation for any quantum optics application that uses samples for implementing various tasks. In particular, future quantum networks will rely on robust integrated devices. The technological fabrication and optimisation of such integrated optical devices is a challenge. However, far more complex and time consuming is the development of the underlying technology. Exactly this has been the major result of my thesis work. A multitude of challenges and questions, which were not anticipated at the beginning of this work, arose and called for a solution. Countless process steps had to be developed and revised in order to be able to produce high performance devices. Just to name a small selection: lithography, waveguide production and modelling, exchange melt composition, exchange procedure, and finally polishing. In addition to the process control and optimisation for the periodic poling, a deep understanding of the material and in particular the poling properties of the material is needed, in order to achieve a homogeneous, efficient periodic poling. During this thesis, I developed and established this technology.

I want to highlight here that, in order to overcome the above mentioned technological challenges, a thorough knowledge of the fundamental physics underlying the sample fabrication process, as well as a careful sample characterisation are indispensable. These two challenges were tackled with the help of in-house collaborations at Paderborn University. Ab initio modelling of KTP was performed in the group of Prof. Wolf Gero Schmidt [1], whereas the group of Prof. Artur Zrenner developed a novel sample characterisation method which was successfully applied to my PPKTP waveguide samples [2].

In cooperation with the group of Prof. Detlef Kip (Helmut Schmidt University, Hamburg), we fabricated a novel type of KTP waveguides applying a dicing technique to our samples to form ridge waveguides [3]. This technique is not available in our in-house cleanroom and represents an alternative fabrication method, which has been receiving significant attention recently.

This thesis focuses on the technological development of KTP processing and the applications I have directly developed and implemented, namely frequency conversion between UV and NIR wavelengths around 800 nm [4].

Eigner *et al.* Opt. Express 26(22), 28827-28833 (2018)

We have demonstrated for the first time the combination of periodic poling and ridge waveguides in KTP. Furthermore, this work presents the first single mode ridge waveguides around 800 nm. I fabricated the periodic poling and the planar rubidium exchange and performed the linear and nonlinear optical characterisation of this device.

Volk *et al.* Opt. Mater. Express 8(1), 82-87 (2018)

This work presents the first realisation of Rb-exchanged ridge waveguides in c-cut KTP. Here, the waveguides were single mode at 1550 nm, making them attractive for telecommunications applications. I fabricated the waveguide sample and characterised the Rb-exchange.

Rüsing *et al.* J. Appl. Physics 119, 044103 (2016)

We used Raman spectroscopy to visualise the domain walls in PPKTP. A major step in this work was to identify the exact vibrational modes in the Raman spectrum that are sensitive to the domain walls. I fabricated the PPKTP sample that was used in this work.

Going far beyond the scope of this thesis are the applications that arose due to the novel technology capabilities established during this work. They can coarsely be separated into two groups: work that is based on the unique dispersion properties of the KTP waveguides I fabricated, and work that benefits from or was enabled by dielectric coatings I designed and (partially) applied. Regarding the related work, results from following publications are partly presented here since they benefit from the technology.

Waveguide Fabrication

Ansari *et al.* Opt. Express 26(3), 2764-2774 (2018)

We implemented a parametric down conversion source based on asymmetric group velocity matching in KTP waveguides. In this configuration, the complex temporal shape of the pump pulse is imprinted onto one of the photons, facilitating the generation of heralded single photons in arbitrary complex pulse shapes. I modelled and fabricated the KTP waveguide sample.

Rüsing *et al.* Physical Review Materials 2 (10), 103801 (2018)

We investigated the origin of the Raman spectroscopy signal in PPKTP domain walls. In simple words, the Raman signal is generated by changed selection rules due to the presence of the domain wall. I fabricated the periodically poled KTP sample that was investigated in this work.

Luo *et al.* in preparation (2019)

We demonstrate the generation of counter propagating photon pairs in parametric down conversion, where one photon travels in the direction of the pump while the other photon travels in the opposite direction. This is enabled by very short (down to sub-micron) poling periods. Here, the poling technology I developed for KTP was transferred to lithium niobate, facilitating the fabrication of shorter poling periods than would have been possible with traditional techniques. This paper highlights the versatility of the new technology, which is not limited to a specific material system.

Coatings

Luo *et al.* Science Advances 5, 1451 (2019)

We developed a complete toolbox for on-chip quantum circuits and used it to demonstrate an integrated version of the seminal Hong-Ou-Mandel interference experiment. I designed the tailored dielectric optical coatings for this device.

Meyer-Scott *et al.* Opt. Express 26(25), 32475-32490 (2018)

We implemented a source of polarisation entangled photon pairs based on type-II parametric down conversion in a Sagnac loop configuration. I have designed the antireflective end facet coatings, which increased the state fidelity from around 87% to over 99.9%.

Stefszky *et al.* J. Opt. 20, 065501 (2018)

We built an integrated, monolithic waveguide resonator tailored for second harmonic generation from 1550 nm to 775 nm. The end mirrors were directly deposited onto the waveguide end facets. This compact design allowed high conversion efficiencies of 75% for cw laser light. I designed the HR/AR coatings and matched the reflectivity to the waveguide losses and calculated reflection phases to realise an ideal resonator.

Allgaier *et al.* Appl. Phys. Lett. 112, 031110 (2018)

We used a so-called quantum pulse gate to perform mode-selective conversion of telecom single photons to the green wavelength regime. Upon conversion, the duration of the photons was increased such that they could then be measured with a streak camera supplied by our collaborators from the University of Dortmund. I designed the HR/AR coatings, which, in this case, were exceptionally demanding as they needed to operate at three specified wavelengths from the visible to the NIR.

Allgaier *et al.* Quantum Sci. Technol. 2, 034012 (2018)

We used a group-velocity matched sum-frequency generation process to perform sampling of the temporal waveform of telecom single photons with a resolution far beyond standard detector capabilities. I designed the multi-band dielectric coating that was applied to the sample end facets and yielded a significant improve in sample performance.

Stefszky *et al.* Phys. Rev. Applied 7, 044026 (2018)

We deployed a monolithic waveguide resonator phasematched for single-mode squeezing-generation at 1550 nm to generate squeezed light in a robust integrated experiment. As a result of the exceptional sample quality, we could generate up to 4.9 dB of squeezing. I designed the tailored end facet coatings, which had to meet fabrication specifications to within less than 1% reflectivity.

Sansoni *et al.* Quantum Information 3, 5 (2017)

We used our integrated optics toolbox to build an on-chip networked source of polarisation-entangled photon pairs, based on two waveguided PDCs followed by a polarising beamsplitter. I designed antireflective and highreflective end facet coatings to improve the generated state's fidelity by reducing reflection losses.

Allgaier *et al.* Nat. Commun. 8, 14288 (2017)

We used a quantum pulse gate to demonstrate the simultaneous frequency conversion and bandwidth compression of telecom single photons. Due to the tailored group velocity relationships, we could demonstrate a bandwidth compression by a factor of 7, whilst achieving conversion efficiencies of more than 60%. I designed the dielectric end facet coatings, which had to be anti-reflective around 557 nm and 1550 nm, and high-reflective around 860 nm.

Allgaier *et al.* arxiv.org/abs/1812.07904

We implemented a so-called quantum pulse shaper, a device capable of reshaping pulsed single photons into user-chosen pulse shapes. We demonstrated the operation principle of this device with single-photon level coherent light pulses. I designed the end facet coatings of the sample, which had to fulfil stringent reflectivity requirements for different, widely spaced wavelengths.

4

Introduction

The field of integrated optics revolves around reducing the footprint of optical setups and apparatuses, whilst at the same time increasing their performance, by providing on-chip platforms for integration [5, 6]. The resulting integrated devices comprise several individual components, such as modulators [7], converters [8], lasers [9], and photodetectors [10], interconnected via optical waveguide structures [11, 12]. Waveguides are key components of integrated optical devices. They confine light into small cross-sections, preventing diffraction losses, and thereby facilitate the efficient low-loss routing of light within the structure. Tailoring of specific device properties, e.g. the width of the waveguides, allows for the fabrication of specialised building blocks such as polarisation converters [13], Mach-Zehnder-type modulators [14], frequency converters [15], or resonators [16].

In particular, the use of integrated technologies for applications in the field of quantum optics and communications has made great progress [17]. Quantum optics focusses on exploiting the quantum nature of light to realise novel applications that go far beyond the capabilities of their classical counterparts. One prominent example are quantum simulators, where one uses a well-controllable quantum system, e.g. photons in a linear optical network, to simulate classically intractable systems like phonons in a solid state [18]. Two major challenges connected with the above application appear: first, one must be able to generate high-quality single photons; second, one needs a way of characterising the quantum properties of the optical systems. In many cases, such effects are studied in the context of fundamental research, where the efficient characterisation of quantum systems [19, 20] and the verification of the operations of quantum devices [21–23] represent a central challenge for quantum technologies [24–26]. The above exemplary mentioned applications will typically comprise several building blocks. This includes sources that produce single photons, devices that implement the optical networks and finally, some way of detecting the photons. The state-of-the-art for the generation of single photons to date is parametric down-conversion (PDC) and it is the workhorse of many quantum optical laboratories around the world [27–30]. Besides the heralded generation of single photons, PDC can also generate more complex quantum states with e.g. polarisation or spatial-mode entanglement [31]. The combination of quantum optics concepts with integrated optics technologies has been very fruitful, and in particular quantum optical applications can benefit from the increased robustness and low losses of integrated optics platforms. From these considerations the field of integrated quantum optics emerged.

Typical platforms for these kind of devices are crystalline materials like silicon [32, 33], which lends to high-density fabrication of linear optical elements. However, a large advantage comes from using nonlinear materials, like lithium niobate (LiNbO_3 , LN) [11, 34], a key component

in classical integrated telecommunication, or potassium titanyl phosphate (KTiOPO₄, KTP), mainly used for frequency conversion in laser applications [35]. KTP has unique dispersion properties that allow for the generation of spectrally pure heralded single photons in the telecommunication wavelength regime [36, 37], which are the backbone of practical quantum optics applications, and therefore is fundamental for telecom based quantum optics. It would be highly desirable to have waveguides in KTP, however the material possesses unique challenges for fabrication, so we need to study in detail the fabrication of KTP waveguides.

KTP is a well known and established material in bulk optics. The typical application for bulk KTP crystals is frequency doubling, for example in Nd:YAG lasers from 1064 nm to 532 nm [35]. Besides that, KTP offers the advantage of a wide transparency range (365-4300 nm), which, in combination with the large nonlinear coefficients of the material, allows for applications with high power densities and therefore high efficiencies in the visible wavelength range. The high mechanical and chemical resistance and the low refractive index change with temperature render devices based on KTP stable against temperature fluctuations and changes in humidity [38]. The coercive field-strength of KTP, that is, the electric field strength required to invert the spontaneous polarisation of the crystal, is one order of magnitude lower than for congruent LN ($E_c^{(KTP)} = 2.1$ kV/mm, $E_c^{(LN)} = 21$ kV/mm [39]). This means that some of the fabrication steps required to build working quantum devices are, in principle, easier accomplished in KTP than in LN. KTP also offers excellent potential for classical integrated optical applications. A key property is the high resistance to photo refraction at room temperature, which enables high pump powers also in the visible wavelength regime, without the need for thermal stabilisation at high temperatures. These properties make KTP an attractive candidate for integrated optics in general [40].

To exploit the benefits of tightly confined fields for long propagation lengths and routing in integrated nonlinear optical devices, reliable fabrication techniques for waveguide structures are required. Several attempts have been made to fabricate waveguides in KTP, but the outstanding challenge that remains is the development of a repeatable fabrication process for homogeneous waveguides, which is compatible with periodic poling.

In this thesis, we present the development of periodically poled, single-mode waveguides for near infrared (NIR) wavelengths around 800 nm. Preliminary fundamental studies on, e.g. coercive field strength, ionic conductivity and gray tracking were performed, to increase the understanding of the material platform. With this knowledge we found new possibilities to overcome technological challenges like the exchange process and the poling behaviour in pure KTP and rubidium-doped substrates. After successfully implementing the new technology, we demonstrated periodically poled waveguides in KTP for frequency conversion in the NIR region. The devices are the very first periodically poled ridge waveguides in KTP. Additionally, we realised the first NIR single-mode waveguides in KTP ridges. The second device is geared towards the same application, but is based upon different fabrication techniques. We realised NIR single-mode, rubidium-exchanged, periodically poled waveguides as a new kind of nonlinear device in KTP. We succeeded in fabricating waveguides that guide light with a symmetric mode shape in the fundamental mode. Both devices are designed for type-II conversion from 400 nm to 800 nm, a highly interesting wavelength for quantum optics [8].

Optical dielectric coatings play a key role to improve and optimise the performance of integrated devices. Applying dielectric coatings on integrated devices can, e.g. suppress the pump [41], in-

crease the outcoupling of single photons by using anti-reflection coatings, [31, 37, 42–44], and realise integrated cavity systems depositing partially high reflective coatings [45, 46].

Structure of the Thesis

The thesis is divided into four parts. Chapter 5, provides the theoretical background of the thesis. In the first part, we start by introducing the theory of nonlinear optics and integrated optics by using the example of frequency conversion. The second part of this chapter is dedicated to the material platform KTP. We give an overview over the crystallographic structure and the inherent material properties required for the understanding of periodic poling and rubidium exchange for waveguide fabrication.

Chapter 6 focuses on the technology part of the thesis. We introduce the state of the art of periodic poling and waveguide fabrication to realise integrated devices in KTP. We then combine this knowledge with the experience from our in-house technology, to develop novel techniques for fabricating periodically poled waveguide structures in KTP. To gain a deeper understanding of the material, we start with preliminary studies of the KTP material. In the main part of this chapter, we critically compare two different fabrication sequences: first, we start with the waveguide fabrication followed by the periodic poling; second, we invert the sequence and fabricate waveguides in previously poled KTP. We conclude this chapter by identifying and discussing the fabrication procedure that is best suited for the fabrication of periodically poled waveguides in KTP.

Chapter 7 gives insight into our dielectric coating technology. Optical dielectric coatings enhance the performance of integrated devices and play a key role in device size reduction. Applying dielectric coatings on integrated devices can achieve, e.g. pump suppression or lossless transmission of light in optical network interfaces. This technology is not limited to the KTP platform but can readily be transferred to LN, glasses and other materials. First, we give an overview about dielectric coatings and the design ideas behind specific coatings. In the next section, we show different coating techniques and discuss their respective advantages and disadvantages. This is followed by a detailed overview over our coating facilities and our broadband monitoring technique for in-situ characterisation of the applied coatings. After the technical explanations, we showcase a few exemplary coatings, which we realised on different material platforms. We conclude this chapter with novel ideas and prospects of dielectric coatings and applications. All these coatings increase the efficiency of the components and allow previously infeasible applications.

In chapter 8, we report on a recent source we developed using the previously described technology. The basic idea is the realisation of a conversion device operating in the single-mode regime at NIR wavelengths around 800 nm. First of all, we discuss recent sources and the state of the art of converters operating in the visible regime. Then, we show the results of the two different sources, namely ridge and channel waveguides, that we realised so far. First, we explain the fabrication of such ridge devices, and discuss the linear and nonlinear optical properties. The second kind of devices are Rb-exchanged channel waveguides. Here as well, we show the technological fabrication and give an overview of the linear and nonlinear optical properties. Finally, in chapter 9, we give an outlook on possible progress and technological improvements.

5

Fundamental Theory

Contents

5.1 Nonlinear Optics	13
5.2 Phase Matching	17
5.3 Potassium Titanyl Phosphate	23
5.4 Domain Inversion	27
5.5 Rubidium Doping of KTP	32
5.6 Optical Properties	34

This chapter is dedicated to the theoretical introduction to nonlinear optics, the nonlinear material KTP, and its properties. We briefly revisit the ideas of integrated nonlinear optics and provide a common basis for the theoretical concepts which we need as a background of this thesis. First, we introduce the nonlinear polarisation and its effect on the second order nonlinearity and the coupled wave equations.

Then, we concentrate on the phase matching, starting with the common case of birefringent phase matching and extend this concept to the powerful case of quasi-phase matching and, finally, discuss the example of second harmonic generation. The second part of this chapter, deals with the nonlinear material KTP. We start with a discussion of the KTP material itself, give a brief introduction into the crystallographic structure, the non-stoichiometric material and its ionic conductivity. Insight into these properties is of great importance to understand the technological behaviour of KTP and the results we achieved. In the following, we concentrate on the properties which are relevant for the periodic poling to achieve quasi-phase matching, namely the Curie temperature, the spontaneous polarisation with its possibility of a reversal and the coercive field strength which is needed for the domain inversion. After this, we focus on the doping of KTP crystals to create waveguide structure. Finally, we discuss the optical properties of KTP and doped materials, which defines the nonlinear optical properties.

5.1 Nonlinear Optics

Nonlinear optics is a part of optics that studies the interaction of light with matter in the regime where the response of the material system to the applied electromagnetic field shows a nonlinear behaviour. For low optical intensities, which are typically produced by non-laser sources, the properties of materials remain independent of the intensity of illumination and the nonlinear effects are very weak. The superposition principle holds true in this regime, and light waves can pass through a material or be reflected without interacting with each other. In the regime of high optical intensities, which can be easily produced in laser sources, the electromagnetic field can modify the optical properties of a material. Here, electromagnetic waves can interact with each

other, i.e. exchanging momentum and energy, and the superposition principle is no longer valid. This interaction can result in the generation of new optical fields at new frequencies, which opens the field for new applications, like nonlinear frequency conversion. Nonlinear interactions are also very important for many experiments in quantum optics. e.g. the generation of quantum states via parametric down conversion. [47–49]

5.1.1 Nonlinear Polarisation

An electromagnetic wave passing through a dielectric material induces a polarisation in the material by a displacement of the valence electrons from their stationary orbits. The induced polarisation depends on applied electric field, and can be expanded in a power series:

$$\vec{P} = \epsilon_0 \chi^{(1)} \vec{E} + \epsilon_0 (\chi^{(2)} \vec{E}^2 + \chi^{(3)} \vec{E}^3 + \dots) = \vec{P}^L + \vec{P}^{NL}, \quad (5.1)$$

ϵ_0 represents the permittivity of the vacuum, \vec{E} is the electric field strength and $\chi^{(m)}$ is the susceptibility tensor. Here, $\vec{P}^L = \epsilon_0 \chi^{(1)} \vec{E}$ represents the linear response of the polarisation and $\vec{P}^{NL} = \epsilon_0 (\chi^{(2)} \vec{E}^2 + \chi^{(3)} \vec{E}^3 + \dots)$ corresponds to the nonlinear part. In most cases, the electric field strength is relatively small and the induced polarisation is proportional to the electric field. Here, the material response is well described by the linear term \vec{P}^L . For high intensities, the relative displacement of the electron from its nucleus is nonlinear with the electric field and \vec{P}^{NL} cannot be neglected anymore. [47, 50]

5.1.2 Second Order Nonlinearity

For some cases, the expansion in equation 5.1 can be terminated with the first nonlinear term. The corresponding contribution to the polarisation is given by $\vec{P}^2 = \epsilon_0 \chi^{(2)} \vec{E}^2$, which is only present in media without a centre of inversion in the point-symmetry group. In symmetric media the second order nonlinearity $\chi^{(2)}$ is zero. Often, the d-tensor is used instead of the second order nonlinear susceptibility. The relation between both is defined as [50]:

$$d_{ijk} = \frac{1}{2} \chi_{ijk}^{(2)}. \quad (5.2)$$

The d-tensor can be simplified by using the crystal symmetry. The Kleinmann symmetry is based on transparent materials, in which χ depends very little on the wavelength, but very strongly on the direction [51]. This means that the value of χ_{ijk} is the same for every permutation of i, j and k. If the Kleinmann symmetry applies for specific frequencies, i.e. all interaction frequencies are far away from resonances, the tensor can be reduced to a 3×6 -element matrix given as

$$\begin{pmatrix} (P_{\omega_3}^{(2)})_x \\ (P_{\omega_3}^{(2)})_y \\ (P_{\omega_3}^{(2)})_z \end{pmatrix} = 2\epsilon_0 K \begin{bmatrix} d_{11} & d_{12} & d_{13} & d_{14} & d_{15} & d_{16} \\ d_{21} & d_{22} & d_{23} & d_{24} & d_{25} & d_{26} \\ d_{31} & d_{32} & d_{33} & d_{34} & d_{35} & d_{36} \end{bmatrix} \begin{pmatrix} (E_{\omega_1})_x (E_{\omega_2})_x \\ (E_{\omega_1})_y (E_{\omega_2})_y \\ (E_{\omega_1})_z (E_{\omega_2})_z \\ (E_{\omega_1})_y (E_{\omega_2})_z + (E_{\omega_1})_z (E_{\omega_2})_y \\ (E_{\omega_1})_x (E_{\omega_2})_z + (E_{\omega_1})_z (E_{\omega_2})_x \\ (E_{\omega_1})_x (E_{\omega_2})_y + (E_{\omega_1})_y (E_{\omega_2})_x \end{pmatrix}. \quad (5.3)$$

Using the notation according to Voigt [52], in which the last two indices are combined into one and using the Kleinmann symmetry, which links the different entries and combines them to 10 independent components, one obtains

$$\begin{pmatrix} (P_{\omega_3}^{(2)})_x \\ (P_{\omega_3}^{(2)})_y \\ (P_{\omega_3}^{(2)})_z \end{pmatrix} = 2\epsilon_0 K \begin{bmatrix} d_{11} & d_{12} & d_{13} & d_{14} & d_{15} & d_{16} \\ d_{16} & d_{22} & d_{23} & d_{24} & d_{14} & d_{12} \\ d_{31} & d_{32} & d_{33} & d_{23} & d_{13} & d_{14} \end{bmatrix} \begin{pmatrix} (E_{\omega_1})_x (E_{\omega_2})_x \\ (E_{\omega_1})_y (E_{\omega_2})_y \\ (E_{\omega_1})_z (E_{\omega_2})_z \\ 2(E_{\omega_1})_y (E_{\omega_2})_z \\ 2(E_{\omega_1})_x (E_{\omega_2})_z \\ 2(E_{\omega_1})_x (E_{\omega_2})_y \end{pmatrix}. \quad (5.4)$$

A further reduction of the number of components is possible by applying the Neumann principle, which states that a crystal property must have at least the symmetry of the crystal. The higher the symmetry group of the crystal, the higher must be the symmetry of the susceptibility tensor.

Using equation 5.4, we can describe different types of nonlinear processes. The most prominent is second harmonic generation (SHG). In this case, two fields with the same frequency ω combine into one field with twice the fundamental frequency, ω_2 . We will use SHG as an example for further calculations. In addition to SHG, other three-wave mixing processes can be achieved (compare to figure 5.1), like sum and difference frequency mixing, and parametric down conversion, which is in principle the reverse process of the SHG.

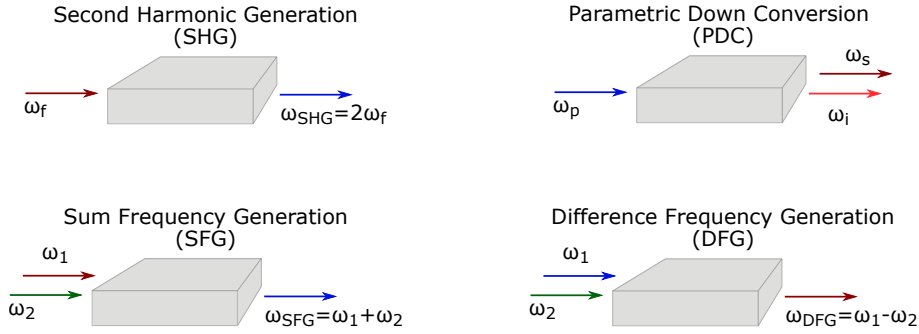


Figure 5.1 – Overview of different types of three-wave mixing processes.

5.1.3 Coupled Wave Equations

Assuming a nonlinear medium, which is non-magnetic, without free charges and currents, the wave equation can be written as

$$\nabla^2 \vec{E} = \mu_0 \sigma \frac{\partial \vec{E}}{\partial t} + \mu_0 \epsilon_0 \frac{\partial^2 \vec{E}}{\partial t^2} + \mu_0 \frac{\partial^2 \vec{P}}{\partial t^2}. \quad (5.5)$$

Here, μ_0 is the permeability of the vacuum and σ describes the losses of the material.

Further assuming quasi-plane and quasi-monochromatic electro-magnetic waves of \vec{E} and \vec{P} travelling in the z -direction, we can write vectors as:

$$\vec{E}(z, t) = \frac{1}{2} [\vec{E}(z, \omega) \exp\{i(kz - \omega t)\}] + c.c. \quad (5.6)$$

$$\vec{P}(z, t) = \frac{1}{2}[\vec{P}(z, \omega)\exp\{i(kz - \omega t)\}] + c.c. \quad (5.7)$$

where ω is the frequency of the waves and k denotes the wavenumber, represented by

$$k = \frac{n(\omega)\omega}{c} \quad (5.8)$$

with the speed of light in vacuum c , and

$$n = \sqrt{\frac{\epsilon(\omega)}{\epsilon_0}} \quad (5.9)$$

being the refractive index of the materials at the frequency ω .

Under the assumption that the envelopes of the fields $\vec{E}(z, \omega)$ and $\vec{P}(z, \omega)$ vary slowly in space and time compared to the wavelength, it is possible to apply the "slowly varying envelope approximation" (SVEA) [53]. By using the SVEA on equation 5.5, it reduces to:

$$\frac{\partial \vec{E}(z, \omega)}{\partial z} = -\alpha \vec{E}(z, \omega) + \frac{i\mu_0 c \omega}{2n} \vec{P}^{NL}(z, \omega). \quad (5.10)$$

In this case, $\alpha = \frac{\mu_0 c \sigma}{2}$ describes the loss coefficient of the electric field.

In second order nonlinear processes all fields mix with each other. This results in three waves, which couple to each other through the polarisations and end up in three coupled wave equations:

$$\begin{aligned} \frac{\partial E_1}{\partial z} &= -\alpha_1 E_1 + \frac{i\omega_1^2}{k_1 c^2} K d_{eff} E_3 E_2^* \exp(i\Delta k z) \\ \frac{\partial E_2}{\partial z} &= -\alpha_2 E_2 + \frac{i\omega_2^2}{k_2 c^2} K d_{eff} E_3 E_1^* \exp(i\Delta k z) \\ \frac{\partial E_3}{\partial z} &= -\alpha_3 E_3 + \frac{i\omega_3^2}{k_3 c^2} K d_{eff} E_1 E_2 \exp(-i\Delta k z). \end{aligned} \quad (5.11)$$

The frequency relation of the interacting waves follows $\omega_3 = \omega_1 + \omega_2$, and the phase-mismatch between them is $\Delta k = k_3 - k_2 - k_1$. The effective nonlinear coefficient d_{eff} can be taken from equation 5.4. The value K can contain the overlap integral of the fields, the factors that differ between type-0 and type-II phase matching, etc. This will be discussed in section 5.2.3. The interaction of the involved fields is maximized for $\Delta k = 0$. If this is achieved, the process is called phase matched.

5.2 Phase Matching

Besides energy conservation, the second law which has to be fulfilled is momentum conservation. In optics, this is related to phase matching of the interacting waves. In all three-wave nonlinear mixing processes, the phase-mismatch has to be zero, i.e. $\Delta k = 0$ (compare to 5.1.3), for useful conversion efficiencies. In the following we use second harmonic generation as an example for a phase matching process. During second harmonic generation, the fundamental wave travels with a phase velocity of $\frac{c}{n(\omega)}$ through the nonlinear medium, while the generated second harmonic wave propagates with a velocity of $\frac{c}{n(2\omega)}$.

Due to the dispersion of the material $n(\omega) \neq n(2\omega)$, the driving field at the frequency ω and the generated field at 2ω are out of phase with each other. The energy which was already transferred from the driving field to the driven field will be transferred back to the initial field, corresponding to a reduction of the efficiency. This is shown in figure 5.2c), orange line, as non-phase matched. There is a certain propagation length in which the energy in the driven field increases; after this length the energy flows in the opposite direction back into the driving field. This distance is called the coherence length of interaction L_c :

$$L_c = \left| \frac{\pi}{\Delta k} \right|. \quad (5.12)$$

However, if phase matching is achieved at each point over the full interaction length, light generated at each point interferes in a constructive way and increases the output power of the generated light. The field of the second harmonic increases linearly with the distance, thus the intensity grows quadratically. In the next sections, we describe two important techniques to achieve phase matching, starting with birefringent phase matching (BPM) (green line in figure 5.2a)) in section 5.2.1, followed by quasi-phase matching (QPM) (red line in figure 5.2b)) in section 5.2.2. [54]

5.2.1 Birefringent Phase Matching

Birefringent phase matching (BPM) is a technique to achieve phase matching exploiting the birefringence of a nonlinear crystal. Normal dispersion leads to higher refractive index for the second-harmonic light and phase matching would not be possible. The interacting waves have different frequencies, so to achieve phase matching, it is necessary to adjust the corresponding phase velocities. This is only possible if the fields are polarised differently, $\beta_{\perp}(\omega) = \beta_{\parallel}(2\omega)$, where \perp represents an orthogonally polarised field and \parallel fields with the same polarisation. The BPM process can be divided into two different categories. Type-I processes involve driving fields (ω) with the same polarisation, and the second harmonic field 2ω is orthogonally polarised compared to the driving one. Type-II processes have orthogonally polarised driving fields.

Birefringent phase matching can be subdivided in noncritical and critical phase matching. In the situation of beam propagation at $\theta = 90^\circ$ to the axis of the dielectric tensor, noncritical phase matching is achieved. Noncritical phase matching is obtained with temperature tuning. The other situation is the case of $\theta \neq 90^\circ$ which is called critical phase matching.

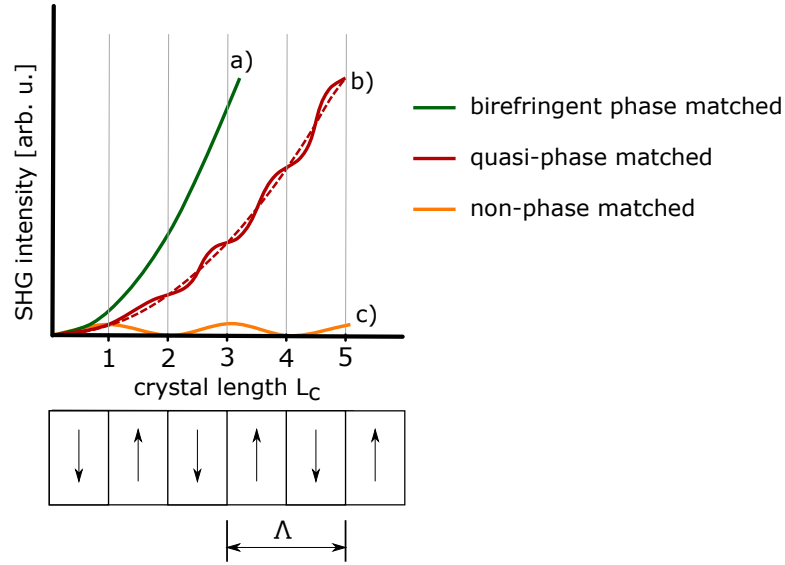


Figure 5.2 – Schematic sketch of different phase matched processes. a) The green line represents birefringent phase matching, b) the red line describes quasi-phase matching, while c) the orange line is a non-phase matched process.

The birefringent phase matching has many limitations, such as Poynting-vector walk-off, access only to the low nonlinear coefficients, and inconvenient phase matching temperatures and angles [54]. The main drawback is the limitation to lower magnitude nonlinear optical coefficients. Typically d_{33} is the largest coefficient, but it cannot be addressed by birefringent phase matching because all involved fields in d_{33} have the same polarisation. Also, the full wavelength range of the material cannot be addressed. One solution to overcome these limitations is the use of a quasi-phase matching.

5.2.2 Quasi-Phase Matching

Quasi-phase matching provides an elegant way to compensate the resulting phase shift between the nonlinear optical polarisation induced by the fundamental or driving wave and the corresponding second harmonic wave (SH wave). This technique was first suggested by Armstrong *et al.* in 1962 [55] and experimentally realised by Somekh und Yariv [56]. During second harmonic generation, the second harmonic field increases with the distance until at a certain point, the energy flows back into the driving field (orange line in figure 5.2). This length is called coherence length. Due to the different propagation velocities, there is no fixed phase relationship between the driving polarisation and the generated wave and a continuous shift of the relative phase occurs. The phase shift leads to destructive and constructive interference along the propagation path, giving a periodic increase and decrease of the second harmonic power $P_{2\omega}$ along the interaction length. If the nonlinear coefficient is modulated with a period twice the coherence length, the phase mismatch can be compensated.

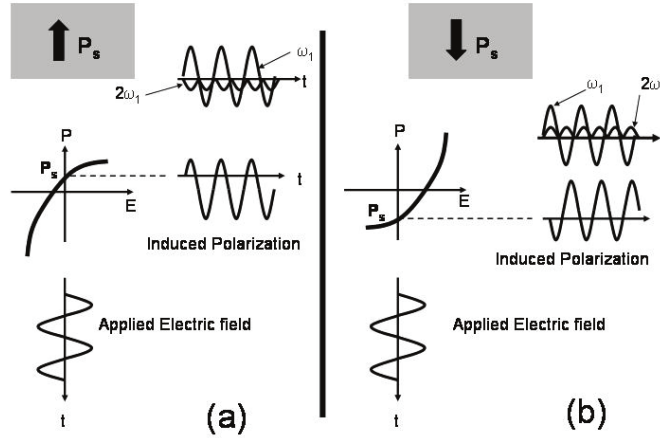


Figure 5.3 – Impact of the spontaneous polarisation on SHG. An inversion of P_s from (a) to (b) leads to a 180° phase shift in the generated second harmonic field. Figure from [57]

This compensation can be done by changing the sign of the nonlinear coefficient (compare to figure 5.3). In contrast to the BPM, QPM requires an artificial structuring of the nonlinear material. The periodic structuring leads to a step-like increase of the SH power (red line in figure 5.2). The increase of the SH power is lower than its birefringent counterpart. Despite this drawback, there are many advantages of using QPM, since a whole new world of interactions can be explored by addressing ideally all possible nonlinear coefficients and a much wider wavelength region than for BPM.

An artificially engineered sign modulation by flipping the sign of the nonlinear tensor d allows the usage of QPM. $d(z)$ is a rectangular function with the period Λ and the magnitude $\pm d$, which represents the modulation of the sign of the nonlinear coefficient (figure 5.4):

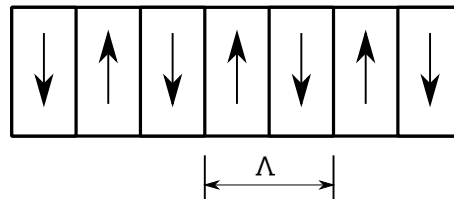


Figure 5.4 – Sketch of a periodical structure to achieve a quasi-phase matching. The arrows indicate the sign of the spontaneous polarisation, and Λ is the period of the inversion.

$$d(z) = d_{eff} \cdot \text{sign} \left[\cos \left(\frac{2\pi z}{\Lambda} \right) \right] \quad (5.13)$$

The periodic spatial change of the nonlinear coefficient can be expressed as a Fourier series:

$$d(z) = d_{eff} \cdot \sum_{m=-\infty}^{\infty} G_m \cdot \exp^{ik_m z}. \quad (5.14)$$

Here, k_m describes the order of the grating vector in relation to the m -th Fourier component of $d(z)$,

$$k_m = \frac{2\pi m}{\Lambda}. \quad (5.15)$$

For a rectangular structure with a duty-cycle

$$D = \frac{l_p}{\Lambda}, \quad (5.16)$$

where l_p is the length of the grating where d is positive, the coefficient G_m takes the values

$$G_m = \frac{2}{\pi m} \sin(\pi m D). \quad (5.17)$$

At the optimum D, i.e. 50% duty-cycle, the sine function becomes 1, and $d_{eff} = \frac{2}{\pi m} d$. Taking into account the m -th Fourier component of the domain grating, the amplitude development

$$\frac{dA_{2\omega}}{dz} = \Theta \cdot \exp^{-i\Delta k_{QPM} z} \quad (5.18)$$

with

$$\Delta k_{QPM} = \Delta k - k_m. \quad (5.19)$$

Solving the integral along the direction of propagation (z) yields

$$\int_0^L \exp^{-i\Delta k_{QPM} z} dz = \frac{2 \cdot \exp\left(\frac{-i\Delta k_{QPM} \cdot L}{2}\right)}{\Delta k_{QPM}} \cdot \sin\left(\frac{\Delta k_{QPM}}{2} \cdot L\right). \quad (5.20)$$

This means for the amplitude of the second harmonic at the end of the nonlinear medium $z=L$ is

$$A_{2\omega}(L) = \Theta \cdot L \cdot \exp\left(\frac{-i\Delta k_{QPM} \cdot L}{2}\right) \cdot \text{sinc}\left(\frac{\Delta k_{QPM}}{2} \cdot L\right). \quad (5.21)$$

If $\Delta k_{QPM} = 0$, the nonlinear polarisation and the second harmonic wave are rephased every coherence length.

For $\Delta k_{QPM} = 0$, $\text{sinc}\left(\frac{\Delta k_{QPM}}{2} \cdot L\right)$ becomes 1 and $\exp\left(\frac{-i\Delta k_{QPM} \cdot L}{2}\right) = 1$, from eq. 5.21.

The amplitude is then

$$A_{2\omega}(L) = \Theta \cdot L. \quad (5.22)$$

To achieve $\Delta k_{QPM} = 0$, the following equation has to be fulfilled:

$$\Delta k_{QPM} = k_{2\omega} - 2k_{\omega} - \frac{2\pi}{\Lambda} = 0. \quad (5.23)$$

For a certain Λ , phase matching ($\Delta k_{QPM} = 0$) can be achieved, which is called quasi-phase matching.

The propagation constant k_ω and $k_{2\omega}$ can be expressed as

$$\begin{aligned} k_{2\omega} &= \frac{2\pi n(2\omega)}{\lambda_{2\omega}} \\ k_\omega &= \frac{2\pi n(\omega)}{\lambda_\omega}. \end{aligned} \quad (5.24)$$

Inserting these in equation 5.23 yields

$$\frac{2\pi}{\lambda_{2\omega}} \cdot n(2\omega) - 2 \frac{2\pi}{\lambda_\omega} \cdot n(\omega) - \frac{2\pi}{\Lambda} = 0 \quad (5.25)$$

and

$$\frac{1}{\lambda_{2\omega}} \cdot n(2\omega) - 2 \frac{1}{\lambda_\omega} \cdot n(\omega) - \frac{1}{\Lambda} = 0. \quad (5.26)$$

With $\lambda_\omega = 2\lambda_{2\omega}$ it follows that

$$\frac{2}{\lambda_\omega} \cdot n(2\omega) - \frac{2}{\lambda_\omega} \cdot n(\omega) - \frac{1}{\Lambda} = 0 \quad (5.27)$$

$$\frac{2}{\lambda_\omega} (n_{eff}(2\omega) - n_{eff}(\omega)) = \frac{1}{\Lambda}. \quad (5.28)$$

Thus one obtains for the coherence length

$$\Rightarrow \Lambda = \frac{\lambda_\omega}{2(n(2\omega) - n(\omega))}. \quad (5.29)$$

The poling period Λ is chosen such that after the coherence length L_c a phase inversion takes place. The relation between the poling period Λ and the coherence length L_c is $\Lambda = 2 \cdot L_c$.

5.2.3 Second Harmonic Generation

In the case of second harmonic generation, two photons with the same frequency ω_{fund} combine and result in a photon having twice the frequency

$$\omega_{SH} = 2\omega_{fund}. \quad (5.30)$$

Starting at the three coupled wave equations in 5.11 for SHG, the following relations can be used:

$$\omega_1 = \omega_2 = \omega \text{ and } \omega_3 = 2\omega. \quad (5.31)$$

Assuming a lossless material and using the given relations, the coupled wave equations reduce to two equations

$$\begin{aligned} \frac{\partial E_{2\omega}}{\partial z} &= \frac{i\omega}{n_{2\omega}c} d_{eff} E_\omega E_\omega \exp(i\Delta kz) \text{ where } K_{SHG} = \frac{1}{2} \\ \frac{\partial E_\omega}{\partial z} &= \frac{i\omega}{n_\omega c} d_{eff} E_{2\omega} E_\omega^* \exp(i\Delta kz) \text{ where } K_{SHG} = 1, \end{aligned} \quad (5.32)$$

with $\Delta k = k_{2\omega} - 2k_\omega$. Assuming a plane wave pump beam, the intensity of each wave can be expressed as

$$I_j = \frac{1}{2} \epsilon_0 c n_j \|E_j\|^2. \quad (5.33)$$

Integrating the first equation of 5.32, over the crystal length L , and assuming the pump is not depleted, gives

$$I_{2\omega} = \frac{2\omega^2 d_{eff}^2 L^2 I_\omega^2}{n_{2\omega} n_\omega^2 \epsilon_0 c^3} \text{sinc} \left(\frac{\Delta k L}{2} \right). \quad (5.34)$$

This intensity is maximized for the phase matched condition $\Delta k = 0$. If the process is not phase matched $\Delta k \neq 0$, the pump polarisation at 2ω evolves in and out of phase with generated wave $E_{2\omega}$ and the conversion oscillates with $\sin(\Delta k \frac{z}{2})$.

All these nonlinear processes can be realised in $\chi^{(2)}$ nonlinear material. One of the prominent ones is KTP. To realise such processes, the material has to be periodically poled to achieve quasi-phase matching. For a deeper understanding of the material and to overcome several technological challenges, we discuss the material properties in the following sections.

5.3 Potassium Titanyl Phosphate

Potassium titanyl phosphate (KTiOPO₄; KTP) is an attractive and commonly used material in nonlinear integrated optics and quantum optics [36, 58]. In 1890, Ouvrard synthesised the first KTP crystals [59] out of a flux of molten potassium pyrophosphate and orthophosphate. However, the optical nonlinearity of the material has been discovered only in 1976. Zumsteg *et al.* [60] measured the nonlinear optical properties in a birefringent second harmonic generation (SHG) experiment, by frequency doubling of Nd-YAG laser.

KTP belongs to the family of isomorphous compounds with generic composition described by MTiOXO₄, where M can be potassium (K), rubidium (Rb), thallium (Tl), ammonium (NH₄) or caesium (Cs) and X can be either phosphorus (P) or arsenic (As). All crystals of this family have an orthorhombic structure and, at room temperature, belong to the non-centrosymmetric point group *mm2* (see 5.3.1). KTP and its isomorphs are characterised by outstanding optical properties: the large transparency range, the high nonlinear and large electro-optic coefficients, as well as the weak photo refraction and the high optical damage resistance. Make these crystals, and KTP in particular, excellent materials for nonlinear optics. Especially for applications in the visible wavelength range with high optical intensities involved, it is the material of choice. However, the fabrication of periodically poled integrated structures is still a challenge. To overcome these challenges we have to understand the material properties. For this reason, we explain in the following sections the material properties, we need for the fabrication of integrated frequency conversion applications.

5.3.1 Crystallographic Structure

Masse and Grenier [61] investigated the structure of KTP, rubidium titanyl phosphate (RbTiOPO₄; RTP) and thallium titanyl phosphate (TlTiOPO₄; TTP) in 1971. The lattice constants of KTP are $a = 12.819 \text{ \AA}$, $b = 6.399 \text{ \AA}$ and $c = 10.584 \text{ \AA}$ [61]. The results from Trodjman *et al.* [62] from 1974, who characterised the crystallographic structure of KTP, were refined by other groups [63, 64] in the following years. At room temperature, KTP is orthorhombic and belongs to the point group *mm2* and the space group *Pna2₁* [61]. The dimension of the unit cell in flux-grown KTP is 871.16 \AA^3 [61]. To describe the unit cell of KTP and its isomorphs properly, 64 atoms are necessary (see figure 5.5). In the unit cell are four asymmetric units with 16 atoms each. These asymmetric units split up into two formula units, each with 8 atoms. Therefore eight formula units describe the unit cell of KTP.

There are two inequivalent potassium sites in KTP. The location of the potassium ion is in a place with high coordination number and bound to the oxygen atoms of the TiO₆ octahedron and PO₄ tetrahedron (see figure 5.6). Helical chains of TiO₆ tetrahedra parallel to the [011] and [0 $\bar{1}$ 1] directions are formed and connected at two corners. Separated by PO₄ tetrahedra, one-dimensional channels along the polar c-axis ([001] direction) locate the potassium atoms [62]. Along these channels an increased mobility of the K-ions gives rise to the anisotropy of many material properties, e.g. ionic conductivity or the large anisotropic domain growth, as we will see later on.

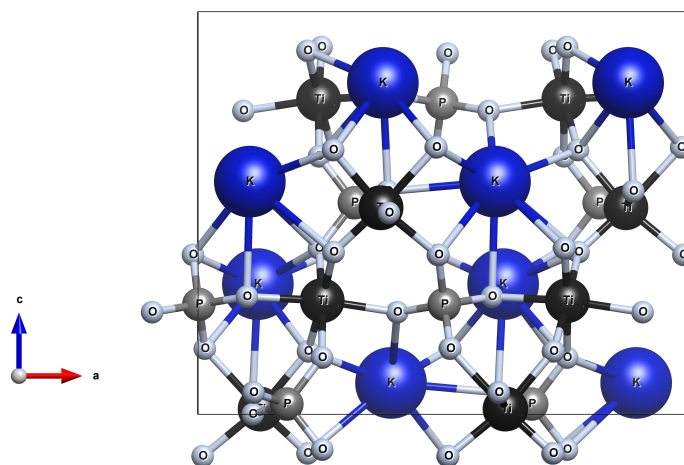


Figure 5.5 – Crystallographic structure of KTP, depicted in its [010] direction. Potassium, oxygen, titanium and phosphor atoms are represented by blue, light grey, dark grey and black spheres. Image generated with [65]

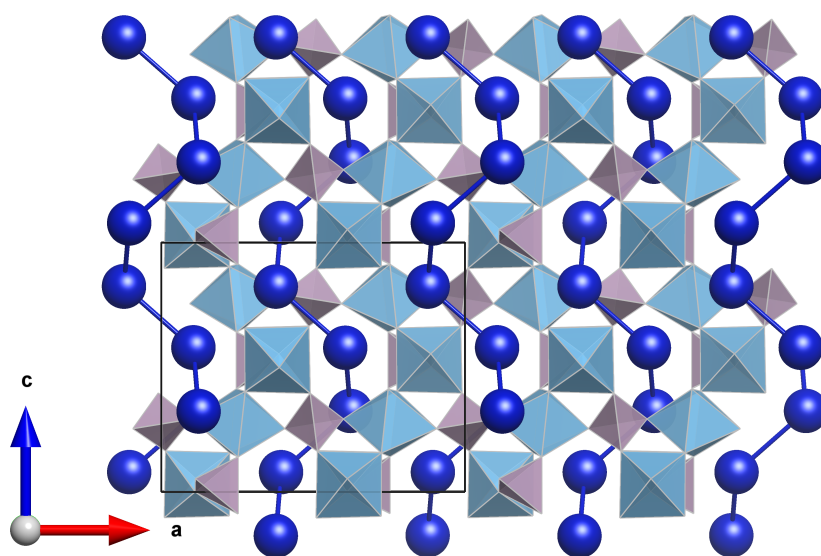


Figure 5.6 – Potassium ions bond to TiO₆ octahedron (light blue) and PO₄ tetrahedron (light red). Along the c-direction, one dimensional chains appear, indicated by the blue lines between the potassium ions (blue balls). Image generated with [65]

5.3.2 Non-stoichiometric KTP

The previously described structure is true for stoichiometric material, which cannot be grown in practise. Regardless of the growth method in all crystals of the KTP family MTiOXO_4 , the X-to-M ratio increases during the crystal growth. The residual solution enriches with M-ions. KTP grown from the KTP/K6–flux [66, 67],



shows a high concentrations of K-vacancies (500-800 ppm) [68] (compare to figure 5.7). These vacancies have to be charge-compensated by positively charged oxygen vacancies [69] and/or by trapped holes at bridging oxygen ions between two titanium ions [70]. The non-stoichiometric KTP can be described as



with x as the concentration of potassium vacancies.

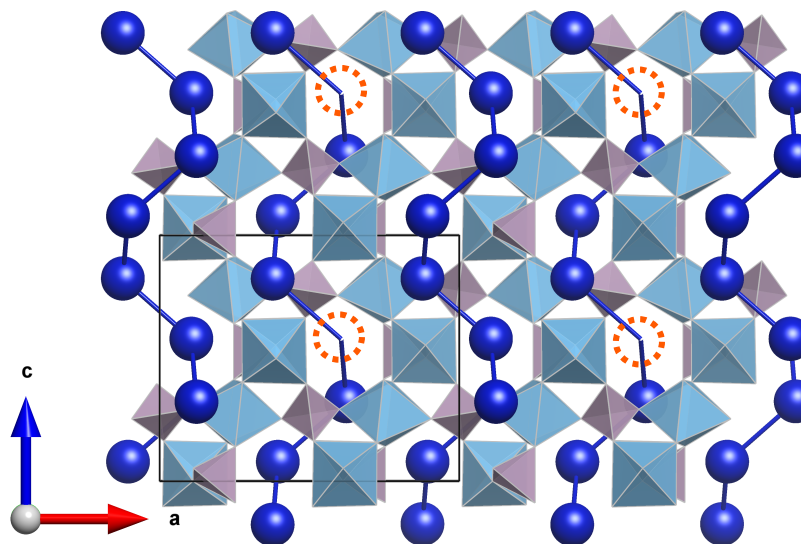


Figure 5.7 – Schematic of a non-stoichiometric KTP lattice. A reduced potassium concentration leads to the occurrence of K-vacancies, indicated by orange dotted rings. An increased amount of vacancies increases the ionic conductivity of the material. Image generated with [65]

5.3.3 Ionic Conductivity

KTP is a dielectric material with band gap of 3.2 eV [71]. The charge transport through interband excitation can be neglected for sufficiently small fields and temperatures. However, a charge compensation can be achieved by ionic conductivity. The ionic conductivity in KTP type crystals can be described by a hopping mechanism, as crystals with relatively high concentration of potassium vacancies show an increased conductivity. Thus, the growth method has a huge influence on the conductivity of the material. Flux grown crystals exhibit a larger number of vacancies than hydrothermally grown crystals. Details on growth methods can be found in [72]. In recent years, the flux grown technique evolved to the most common method for KTP crystal growth, due to the simpler and cheaper technical effort. Furthermore, the quality of the crystals is increased, which can be directly seen in the reduced conductivity compared to crystals grown a few years ago. This will be discussed in chapter 6.3.1.2.

Several attempts to reduce the ionic conductivity in KTP type crystals can be found in the literature [73–78]. Relevant methods will be described in the following. One idea for a temporary reduction is a lowering of the temperature, which leads to a reduction of the ion mobility. The low thermal energy reduces the charge carrier mobility. A temperature of 170 K reduces on the one hand the conductivity to vanishing values. On the other hand, it increases the coercive field strength by one order of magnitude to 21 kV/mm [78].

A permanent reduction is achieved by a potassium treatment. This method was developed by H. Suche, H. Rütz and O. Driesner in 2014 [75]. Here, the crystal is immersed in a pure potassium nitrate (KNO_3) bath. This method aims to equalise the potassium deficit which occurred during the crystal growth. A similar result can be achieved in a melt of other alkali metals of higher order numbers. In case of KTP, Rb and Cs are common materials to use. Already a very small amount of doping reduces the conductivity by two or more orders of magnitude. This doping can be either done in an ion exchange after the crystal growth, like the potassium treatment, or during the crystal growth, leading to a homogeneous concentration distribution of the dopant over the full crystal. Rubidium and caesium show a higher activation energy compared to potassium, which plays an important role in doped crystals, i.e. for waveguide fabrication and periodic poling, respectively. A simple explanation is the larger radius of the Rb-ions compared to K. The ions block the one-dimensional channels in the c-direction (section 5.3.1) and prohibit ion mobility and therefore an ionic current. Since the ionic conductivity is an important property of the crystals for several parts of this thesis, it is further investigated in more detail in chapter 6.3.1.

5.4 Domain Inversion

Periodic domain inversion is an important feature, as already explained in the process of quasi-phase matching in section 5.2.2. We investigate the phenomenon of $\chi^{(2)}$ inversion in nonlinear materials to achieve quasi-phase matching. The physical properties behind this phenomenon will be described in the following sections.

5.4.1 Curie Temperature

Ferroelectricity is a characteristic of materials, owning a spontaneous polarisation which can be reversed by applying an external electric field (see chapter 5.4.2) [79, 80]. It occurs only in crystals in which the crystalline symmetry allows a polar axis, e.g. in KTP or lithium niobate (LN). At the Curie temperature T_C in KTP ($T_C \sim 945 \text{ }^\circ\text{C}$) [81] the spontaneous polarisation disappears analogously to ferromagnetism. Above this temperature, the material shows a paraelectric behaviour. At the Curie temperature a phase transition takes place and the material becomes ferroelectric again [82]. The crystal in the paraelectric phase shows a higher crystal-symmetry within the $Pnna$ group [61], in comparison to the ferroelectric phase. A small distortion in the crystal structure below $945 \text{ }^\circ\text{C}$ leads to a lower lattice symmetry ($Pna2_1$ -group) within the ferroelectric phase. As shown in figure 5.8 the potassium ion can occupy two different sites within the lattice structure. The displacement occurs either by alternating short and long Ti-O bond or/and by the location of the potassium ions. The monovalent potassium ions are either 8-coordinated (denoted as K(1)) or 9-coordinated (denoted as K(2)) with respect to the oxygen. This change is responsible for a spontaneous polarisation.

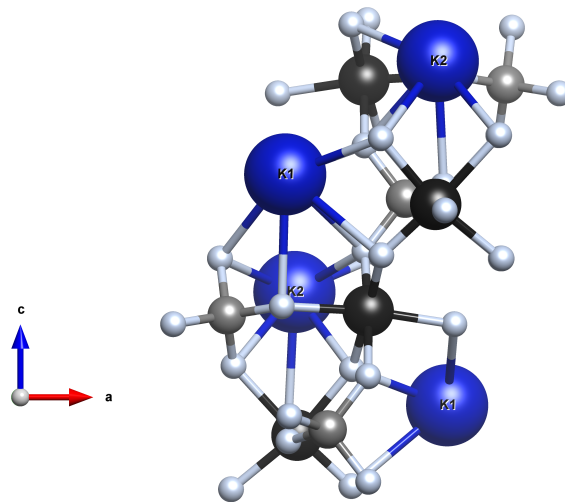


Figure 5.8 – Excerpt of the KTP lattice, indicating the different lattice sites, K1 and K2, the potassium atoms can occupy within the lattice. Both sites differ in bonding strength and length to adjacent atoms. Image generated with [65]

5.4.2 Spontaneous Polarisation and Optical Nonlinearity

As introduced in the previous section, KTP exhibit a spontaneous polarisation below the Curie temperature in the ferroelectric phase. This ferroelectricity is introduced by a shift \vec{d} of positive and negative charge centres Q within a unit cell of a charge-neutral solid. The dielectric polarisation is defined as the microscopic dipole moment $\vec{P} = \vec{d}Q$ with respect to the unit cell volume [83]. This dielectric polarisation is called spontaneous polarisation and appears mainly in one direction of a crystal. The spontaneous polarisation in ferroelectric materials is in thermodynamic equilibrium and therefore stable over time.

The distorted crystal structure in ferroelectric KTP leads to the spontaneous polarisation P_s (see 5.4.1). The origin of P_s is not fully understood yet. Two sources can be identified, which explain the nonlinear optical properties.

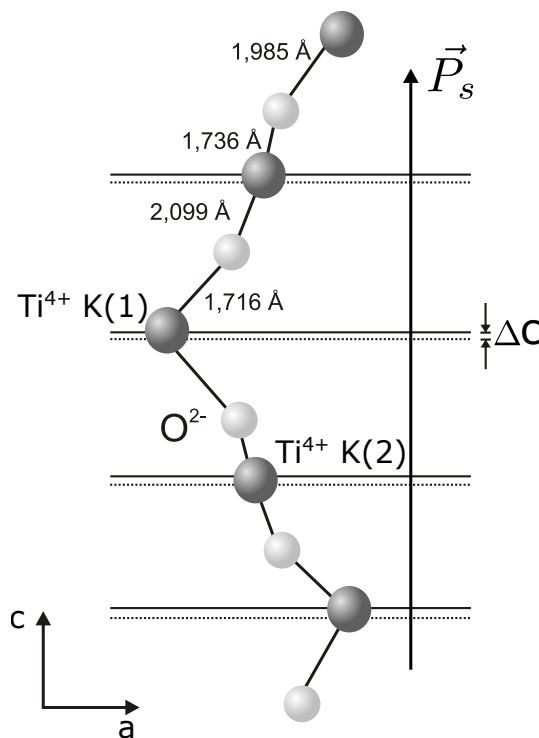


Figure 5.9 – Influence of a Ti displacement on the spontaneous polarisation. The displacement can be visualised by the change in the Ti bonding lengths.

One source was discussed first in 1976 by Zumsteg *et al.* [60]. They identified the presence of one-dimensional channels and different lengths of the Ti-O bonds as the source for the nonlinear optical properties. The Ti-ion in the TiO_6 octahedra can be at two different positions. A displacement from the centre positions of these independent positions in the Ti(1) octahedra and the Ti(2) octahedra (Δc in figure 5.9) results in different short and long Ti-O bonds which leads to a permanent dipole moment in the c -direction.

In 1997, Xue and Zhang argued that the PO_4 tetrahedral and the K-O groups are responsible for the optical nonlinearity [84].

Up to now it is not clear which has the main impact on the nonlinear properties. On the one hand, the exchange of the potassium ion against other ions has a huge impact on spontaneous polarisation reversal properties. On the other hand, Raman analysis implies a stronger effect on the Ti octahedra signals [85].

The origin of the spontaneous polarisation in KTP cannot be explained at this point and will not be a part of this thesis. Further investigations are necessary to understand the mechanism behind the spontaneous polarisation. Nevertheless, an inversion of the spontaneous polarisation is possible and will be discussed in the next section.

5.4.3 Polarisation Reversal and Ferroelectric Domains

The key feature that makes ferroelectric materials versatile systems is the possibility of reversing the polarity of the spontaneous polarisation. This can be achieved for example by an external electric field, which has to be higher than the coercive field strength. This dependence will be discussed in the next section. Application of an electric field makes one direction of the spontaneous polarisation to be preferred over the other. In terms of a double well this is like pushing one well up and the other down (compare to figure 5.10). At the coercive field strength, the polarisation reaches a saturation polarisation P_s and cannot be further increased (see P_s in figure 5.10), (details on the coercive field strength can be found in section 5.4.4). If the external field is switched off, a residual polarisation P_r remains in the crystal. An opposing field can invert this polarisation, again.

The hysteresis loop, which is shown in figure 5.10, and the related inversion occurs only in ferroelectric materials. In KTP, the residual polarisation P_r is approximately equal to the spontaneous polarisation P_s .

As discussed in section 5.4.2, the reversal of the spontaneous polarisation P_s is linked to a displacement of Ti-ions within the TiO_6 octahedra and a change of the bonding lengths: the short Ti-bonds become long and vice versa [86]. Also, the alkali ions, e.g. K, Rb, Cs, shift along the c -direction. During the polarisation reversal, the change of the surface charges has to be compensated by a displacement current. A complete reversal requires a charge transfer of

$$Q = 2 \cdot P_s \cdot A. \quad (5.37)$$

Here, A is the inversion area of the sample and P_s is the spontaneous polarisation with a value of $P_s = 20.1 \frac{\mu\text{C}}{\text{cm}^2}$ measured in KTP by Rosenman *et al.* in 1997 [87].

In ferroelectric crystals, regions with the same direction of the polarisation are called domains. If the spontaneous polarisation is inverted in a periodic way, a periodic domain grating can be created. The boundary areas between polarisation directions with an opposite sign are named domain walls.

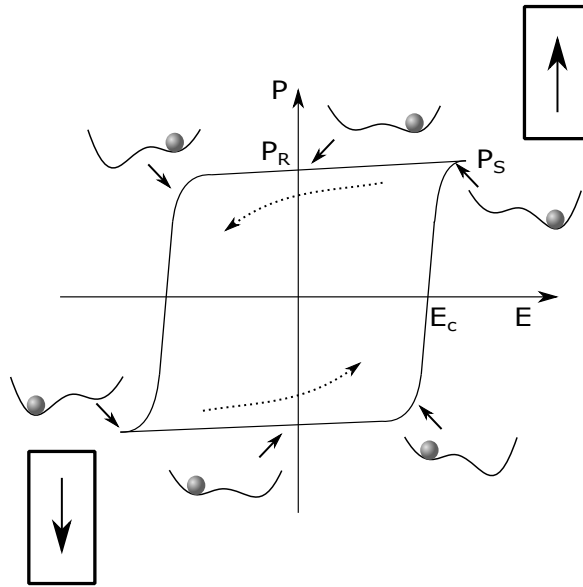


Figure 5.10 – Polarisation reversal hysteresis of a ferroelectric material. The direction of the spontaneous polarisation is indicated by the arrow in the box. The double well potential represents the different occupied lattice sites on each side of the spontaneous polarisation direction, indicated for various electric field strengths and directions.

The poling period is the length of an inverted plus a non-inverted region and indicated by Λ . The duty cycle is defined as the ratio between the inverted region and the period (see figure 5.4). For efficient quasi-phase matched nonlinear frequency conversion applications, the duty cycle should be 1 : 1 (compare to section 5.2.2). The domain growth in ferroelectric materials starts with a nucleation of nanodomains. These nuclei grow in the depth, merge, and form domains. The growth is predominantly parallel to the external field but also slightly perpendicular to the field. This anisotropy of the domain wall motion forms the basis for periodic domain inversion and is very strong in KTP. It depends strongly on the applied field strength. Figure 5.11 schematically shows the evolution of domain nucleation and anisotropic growth of domains inside of the crystal. The growth speed along the optical c-axis is $200 \frac{\mu\text{m}}{\text{ms}}$, measured at a field strength of $2.2 \frac{\text{kV}}{\text{mm}}$ [58] and the external field along the c-axis. At the same time, the domain broadening in the a and b-direction is orders of magnitude lower than in the c-direction. Comparing the domain velocity in the a and b-directions, the domain growth in the a-direction is much smaller. The lower domain broadening allows for the fabrication of small domains and therefore for short poling periods. Realisation of short poling periods is a key to realise QPM processes that bridge large momentum gaps, like the one encountered in frequency conversion between very distant wavelengths or counter-propagating parametric down conversion. To fully exploit KTP poling properties, it is therefore advisable to use the a-direction as propagation axis for the nonlinear interaction, since the domain growth in this direction can be controlled much more precisely.

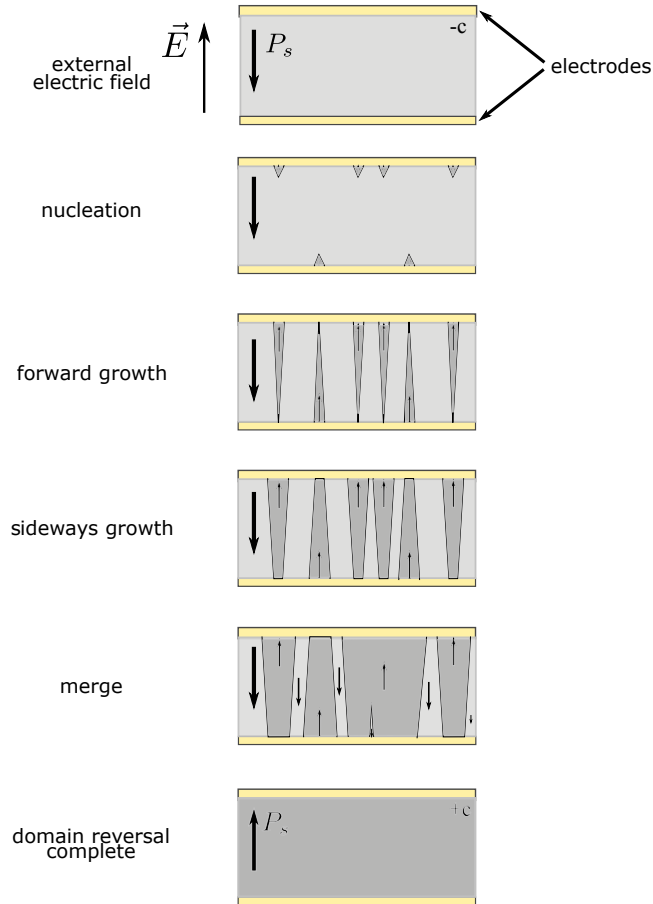


Figure 5.11 – Schematic of the temporal evolution of domain growth in KTP.

5.4.4 Coercive Field Strength

As mentioned in the previous section, the coercive field strength E_c is an important parameter for periodic poling and therefore characterised in detail in this thesis. It is defined as the field at which half of the spontaneous polarisation of a crystal is reversed (see E_c in figure 5.10). For very small or very large field strengths in comparison to the coercive field strength, the material behaves like an ordinary dielectric. However, the estimation of the coercive field is still a challenge, since the measurement depends on the temperature, the type of electrode used in contacting the crystal, on the measurement frequency, the pulse shape of the applied voltage and the measurement technique. For flux grown KTP, the coercive field strength is in the order of $1.7 - 2.1 \frac{\text{kV}}{\text{mm}}$ [58]. The value also strongly depends on vacancies, defects and dopants in the crystal. The influence of dopants will be discussed later but has to be considered during the experiments and will be analysed in section 6.3.1.3.

5.5 Rubidium Doping of KTP

A major problem in bulk nonlinear optics is the low efficiency that arises from the diffraction of Gaussian beams. Moreover, bulk devices and free space setups are sensitive to alignment and temperature stability and cannot easily be integrated in fibre networks. A way to overcome these problems is to realise nonlinear processes in waveguides. A waveguide is a structure designed to prevent light from diffracting, therefore increasing the modal confinement and the useful length of the devices. The confinement is achieved with an increase of the refractive index of the crystal along the propagation axis of the light. For a two dimensional confinement of the light in a guiding structure, it is necessary to ensure a refractive index increase in the transverse plane of the system, i.e. along the depth and the width of the waveguide.

Doping of KTiOXO_4 with larger alkali ions, e.g. rubidium (Rb) or caesium (Cs), is possible and allows for a modification of the dielectric properties and leads to an increase of the refractive indices and therefore allows the realisation of optical waveguides. We focus on the Rb-doping, which is a common way to fabricate waveguides in KTP. The doped crystal can be described by $\text{Rb}_x\text{K}_{1-x}\text{TiOPO}_4$ with $x=0 \rightarrow 1$ (in short RKTP). The full replacement of K- by Rb-ions forms rubidium titanyl phosphate (RbTiOPO_4 ; RTP) crystals. The two inequivalent K-sites (K(1) and K(2), described in 5.3.1) play an important role during the diffusion process. The volume of the K(1) site is 25% lower in comparison to the K(2) site [88]. This may explain why the Rb-ions preferentially occupy the larger K(2) sites [89] due to the lower lattice energy (see figure 5.12). The diffusion of Rb-ions into KTP takes place in a melt of rubidium nitrate (RbNO_3). The melt can be modelled as an infinite bath, which means the Rb concentration during the exchange does not change over time. The simplest description of the diffusion process is the one dimensional diffusion equation, which is described in [90]. We start from Fick's first law, describing the relationship between diffusion current density $j(x)$, in our case the in-diffusing rubidium ions, and the concentration of the already in-diffused rubidium ions $c(x)$

$$j(x) = -D \cdot \nabla c(x), \quad (5.38)$$

where D is the diffusion coefficient. According to the continuity equation, the change of the concentration over time is related to the divergence of the particle flowing in and out of a volume

$$\frac{\partial c}{\partial t} + \nabla \vec{j} = 0. \quad (5.39)$$

Solving these equations for a one-dimensional diffusion process with a concentration-independent diffusion coefficient D , the diffusion equation derives to

$$\frac{\partial c}{\partial t} = D \frac{\partial^2 c}{\partial x^2}. \quad (5.40)$$

We consider an infinite bath, which means there is no change in the concentration of the bath over time:

$$c(x = 0, t) = c_0. \quad (5.41)$$

For pure KTP, there is no Rb-content in the crystal at the beginning of the diffusion:

$$c(x, t = 0) = 0. \quad (5.42)$$

Solving the diffusion equation under these conditions, we obtain

$$c(x, t) = c_0 \operatorname{erfc} \left(\frac{x}{2\sqrt{Dt}} \right), \quad (5.43)$$

with t the exchange time, D the diffusion coefficient, c_0 the concentration at the surface and x the diffusion in the depth of the crystal, in our experiments in the c -direction of the crystal. A full description of the diffusion process is given in [91]. During our experiments, we have to measure the diffusion depth to compare different types of waveguides. Two different formulas for the calculation of the penetration depth of waveguides can be found in the literature. One definition is the depth of

$$\frac{c}{c_0} = \operatorname{erfc}(1). \quad (5.44)$$

This leads to a diffusion depth which is proportional to the square root of the exchange time and the diffusion coefficient:

$$d_{\operatorname{erfc}(1)} = 2\sqrt{D(T)t}. \quad (5.45)$$

Another, commonly used definition is the $\frac{1}{e}$ diffusion depth, which leads to a diffusion depth identical to equation 5.45 multiplied by the factor of $\frac{1}{\sqrt{2}}$:

$$d_{\frac{1}{e}} = \frac{1}{\sqrt{2}} d_{\operatorname{erfc}(1)}. \quad (5.46)$$

Details about the diffusion depth can be found in [92]. In the following, we are using equation 5.44 for the definition and calculation of the diffusion depth. The indiffusion of Rb-ions increases the refractive index in the doped region, which allows waveguiding and enables the realisation of integrated devices in KTP. The indiffusion changes the optical properties of the material only in a small manner which preserves the outstanding optical properties of KTP. For integrated optical applications, the optical properties are of a great interest and will be discussed in the next section.

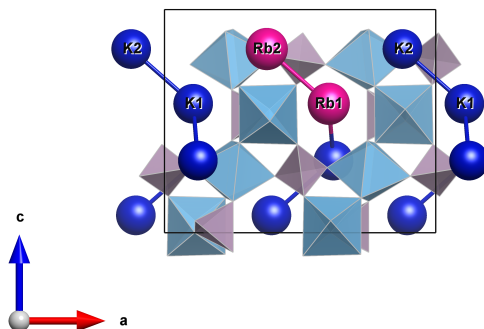


Figure 5.12 – Illustration of the rubidium-potassium exchange in KTP. The one dimensional chains define the direction of the exchange along the c -direction. Image generated with [65]

5.6 Optical Properties

For integrated optical applications, the optical properties of KTP are of great interest. KTP exhibits a large transparency range from 0.365 μm to almost 4 μm . The transmission of KTP and its isomorphs has been measured by Hanson *et al.* [93] for unpolarised light. At infrared wavelengths above 3 μm an enhanced absorption appears, related to OH-groups trapped in the crystal during the crystal growth.

The electro optic tensor of KTP has only 5 non-zero elements. Its values, measured at $\lambda=633$ nm are [38]:

$$r = \begin{bmatrix} 0 & 0 & r_{13} \\ 0 & 0 & r_{23} \\ 0 & 0 & r_{33} \\ 0 & r_{42} & 0 \\ r_{51} & 0 & 0 \\ 0 & 0 & 0 \end{bmatrix} = \begin{bmatrix} 0 & 0 & 9.5 \\ 0 & 0 & 15.17 \\ 0 & 0 & 36.6 \\ 0 & 9.3 & 0 \\ 5.3 & 0 & 0 \\ 0 & 0 & 0 \end{bmatrix} \left[\frac{\text{pm}}{\text{V}} \right].$$

KTP has the symmetry of the point group $mm2$. The second-order susceptibility tensor then becomes

$$d = \begin{bmatrix} 0 & 0 & 0 & 0 & d_{15} & 0 \\ 0 & 0 & 0 & d_{24} & 0 & 0 \\ d_{31} & d_{32} & d_{33} & 0 & 0 & 0 \end{bmatrix}. \quad (5.47)$$

The nonlinear susceptibility coefficients for different wavelengths are collected in table 5.1

Table 5.1 – Nonlinear susceptibility coefficients for KTP.

	d_{31}	d_{32}	d_{33}	d_{24}	d_{15}
532 nm [pm/V] [94]	1.4	2.65	10.7	2.65	1.4
1064 nm [pm/V] [95]	2.4	4.4	16.9	7.9	6.1

An important property when choosing a crystal for nonlinear optical applications is its resistance to optical induced damage, especially for applications in the visible and in the UV regime. A high energy laser beam creates optically excited free carriers in the crystal. If these carriers get trapped outside the optical beam, they create an internal field which distorts the beam via the electro-optic effect and leads to photo refractive damage. KTP has the advantage of several orders of magnitude lower photo refraction than LiNbO_3 . This enables the possibility to operate KTP at room temperatures, while LiNbO_3 has to be heated above 100°C. One reason for the low photo refraction is the relatively high ionic conductivity, which leads to a fast redistribution of the free carriers and to a shielding of the induced field by the carriers. However, radiation with high intensities in the blue to green region in the spectral domain induce absorbing colour centres in the crystal, creating Gray tracks, which are partially associated with Ti^{4+} formation [96].

5.6.1 Gray Tracking

Radiation with a high optical electromagnetic field, X-ray or an external electric field can create gray tracks in KTP material. In comparison to transparent crystals, gray tracks exhibit a high optical absorption. This can lead to a catastrophic damage in an experiment with high optical intensities up to destruction of the crystal [97]. In addition, this effect increases the anisotropy of linear optical properties which limits the applicability [96]. Because this is a limiting factor in an experiment, we will discuss in this section the gray track phenomenon and describe different mechanisms which can create gray tracks.

Several experiments have been conducted to investigate and understand the origin of gray tracking. However, an exact description is still an open question. In an experiment by V. A. Maslov *et al.* in 1997 [98], KTP crystals were illuminated by light with wavelengths of 1064 nm, 870 nm, 700 nm and 532 nm. They discovered a negligible absorption of the first harmonic, while the second order nonlinear absorption increases to $10^{-9} \frac{1}{\text{Wcm}}$. Furthermore, the absorption increases by 50% if both fields were present in the crystal. Therefore, they attributed the effect of discolouration to a two-photon process during the frequency doubling. However, in 1992 Loiacono *et al.* [99] observed gray tracking in samples which were illuminated by monochromatic light at 530 nm wavelength. This wavelength corresponds to absorptions wavelength in Ti^{3+} centres. Therefore, they predict a reduction process from Ti^{4+} to Ti^{3+} as the origin of the increased absorption in the material. Already in 1989 Roelofs could detect Ti^{3+} in gray tracking samples [70]. In the same study, it was also observed that gray tracks are also caused by the application of external electric fields.

Scripsick suggested that the reduction is due to a charge imbalance within the cell. Irradiation with high-intensity light or the application of an external electric field can lead to the formation of electron-hole pairs. If these recombine, no change in absorption is observed. However, if the electron-hole pairs are separated sufficiently during their formation, they can be stabilised by defects which are located in the crystal [100]. In particular, in KTP crystals, electrons can be trapped by titanium ions, which are sited close to the oxygen vacancy [100]. However, holes are stabilised by titanium-titanium bonded oxygen atoms in the presence of a potassium vacancy [101]. As already discussed in section 5.3.3, KTP inhibits a large number of potassium vacancies, where free, positively charged holes can be bonded. In addition, various processes can induce oxygen vacancies in the cell, as it can be observed for example in an H_2 atmosphere. At high temperatures and low oxygen concentration, also called "hypoxia", oxygen atoms diffuse from the interior of the crystal to the surface. Here, they combine to O_2 and transfer into the gas phase or react, if the thermal energy is sufficient, with the existing H_2 molecules to form water [102]. Gray tracking can be induced by an annealing in a low oxygen atmosphere. The process can be reversed by annealing in an oxygen rich atmosphere [103]. Thermal annealing in pure oxygen can recover gray tracked samples or even increase the transmittance of as-grown KTP by roughly 20%.

5.6.2 Material Dispersion

Dispersion describes the refractive index depending on optical frequency $n(\lambda)$. For an accurate prediction of desired QPM periods for a given process (wavelength and polarisation) it is required to know the dispersion of the material. The refractive index can be expressed in the form of Sellmeier equation as

$$n_i(\lambda) = A + \frac{B}{\lambda^2 - C} + \frac{D}{\lambda^2 - E}. \quad (5.48)$$

In our experiments, we use the Sellmeier equations taken from Kato *et al.* [104]. The values can be found in table 5.2.

Table 5.2 – Sellmeier coefficients for KTP crystals [104].

	A	B	C	D	E
n_a	3.23100	0.04140	0.03978	9.35522	31.45571
n_b	3.45018	0.04341	0.04597	16.98825	39.43799
n_c	4.59423	0.06206	0.04763	110.80672	86.12171

However, when a material with high refractive index is surrounded by one with lower refractive index, light can be guided in the first region without suffering diffraction losses. Since the propagation of the light beam is significantly different than in the free space propagation case, the dispersion properties are affected by these guiding conditions. In particular, the modified dispersion properties depend on the waveguide geometry and refractive index distribution. For the indices of our waveguides $n_i(\lambda)$ we used the Sellmeier equations for bulk KTP $n_{i(\text{bulk})}(\lambda)$ [104] and a modification to describe the refractive index increase of the rubidium exchange $\Delta n_{i(\text{waveguide})}(\lambda)$ [105] which has also a dispersive character:

$$n_i(\lambda) = n_{i(\text{bulk})}(\lambda) + \Delta n_{i(\text{waveguide})}(\lambda). \quad (5.49)$$

The waveguide dispersion is taken from Callahan *et al.* [105].

$$\Delta n_{i(\text{waveguide})}(\lambda) = A + B\lambda + C\lambda^2 + F e^{-(\lambda - \frac{350}{G})} \quad (5.50)$$

The values for the refractive index increase in waveguides including the dispersion can be found in table 5.3 with λ in [mm].

Table 5.3 – Sellmeier coefficients for Rb-exchanged waveguides in KTP [105].

	A	B	C	F	G
Δn_b	2.90816×10^2	-6.5850×10^6	2.13894×10^9	9.60547×10^3	39.20047
Δn_c	2.67947×10^2	-1.09737×10^5	2.29268×10^9	2.24565×10^2	44.62477

With these values, the refractive index and the waveguide dispersion can be described (see figure 5.13). This is an important description, which we need and use for the calculation of phase matched processes in the applications part at the end of this thesis. Furthermore, we use these relations to reconstruct and recalculate the obtained phase matching in the analysis

of second harmonic generation. Starting from the refractive indices, we calculate the group velocity v_g (see figure 5.14). KTP is the only $\chi^{(2)}$ nonlinear material, that allows for group velocity matching in the telecom wavelength regime. Here, the group velocity of the pump field is between signal and idler photons [36]. Furthermore, the tailoring of the waveguide properties allows for the simultaneous realisation of birefringent phase matching and asymmetric group velocity matching. In this case, the group velocities of the pump photon at 670 nm and the idler photon at 1276 nm are equal; the signal photon is then at 1411 nm and has a higher velocity than both [37].

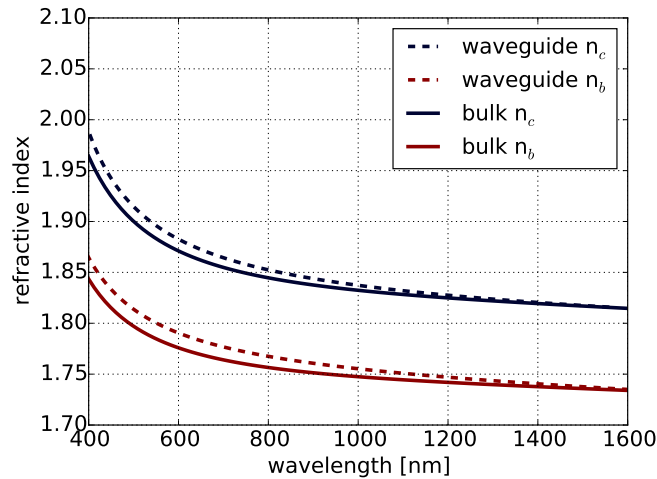


Figure 5.13 – Dispersion for bulk KTP and our KTP waveguide model. The two important refractive indices n_b and n_c are plotted.

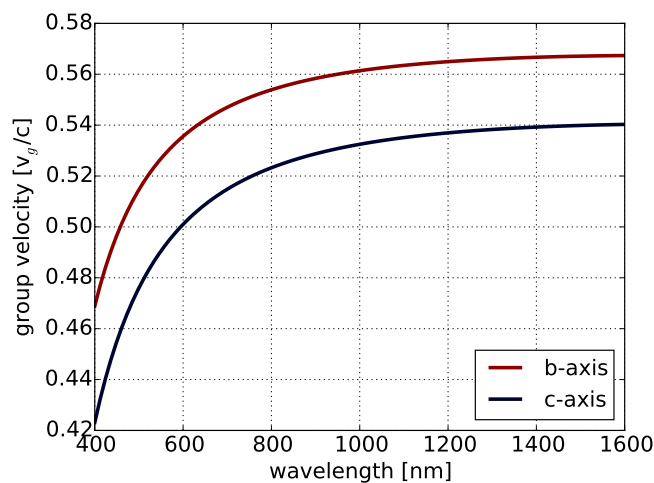


Figure 5.14 – Group velocity in KTP for the crystal b- and c-axis, respectively.

Summary

In this chapter, we introduced the relevant nonlinear optics including the nonlinear polarisation, the second order nonlinearity and the concept of coupled wave equations. We discussed phase matching for the example of birefringent phase matching and showed the idea of quasi-phase matching which opens the possibility for many new applications. Later on, we described the nonlinear material KTP with its crystallographic properties. To understand the periodic poling and the waveguide fabrication, we gave insight into the domain inversion properties and the doping mechanism of the material. Finally, we showed the optical properties, in which we are interested for the realisation of nonlinear integrated devices.

Contents

6.1 State of the Art: Periodically Poled Waveguides in KTP	39
6.2 In-house Processing	48
6.3 Poled Waveguide Results	61

In the previous chapter, we have introduced the material properties of KTP and its isomorphs. In this chapter, we will use the understanding of the material to develop the techniques for periodic poling and waveguide fabrication in KTP and get an insight into the fabrication process and the results. First, we give an overview

about the state of the art of waveguide fabrication and periodic poling in KTP. Afterwards, we show our periodic poling setup and our waveguide fabrication technique, which we developed. Before the fabrication, we start with a preliminary investigation of KTP to get a deeper understanding of the poling dynamics. Periodically poled waveguide fabrication consists of two steps, waveguide fabrication and periodic poling. These two steps are theoretically independent, i.e. it is possible to fabricate the waveguide and subsequently pole them or, vice versa, first pole the bulk crystal and then fabricate the waveguides. We show the results for both fabrication sequences and conclude this chapter with a brief discussion on the sequence of the fabrication process.

6.1 State of the Art: Periodically Poled Waveguides in KTP

The realisation of efficient integrated frequency converters, especially for UV applications, requires a material, which fulfills several requirements. The ideal frequency converter would possess a wide transparency range from the IR to the UV, a $\chi^{(2)}$ nonlinearity, a high damage threshold, low photorefraction in the UV and the possibility to produce waveguides.

If we compare different material systems like silicon, KTP, lithium niobate LN, β -barium borate BBO, bismuth triborate BiBo and all isomorph of the material families, only KTP exhibits all requirements. Silicon is only transparent in the IR [106], such that this material is not suitable for this kind of converter. Moreover, crystals with a centro-symmetric structure can access only $\chi^{(3)}$ nonlinearities, that reduces the conversion efficiency by several orders of magnitude, in comparison to $\chi^{(2)}$ materials [47]. For the realisation of UV light devices a high damage threshold and low photorefraction in the visible and UV regime is essential. Due to high photorefraction in LN, the material is not suitable for applications in the UV [107]. Common materials for UV

applications are KTP, BBO and BiBo. BBO and BiBo don't allow periodic poling for QPM, which limits the adjustability and applicability of such devices. Since it is also possible to produce waveguides in KTP and periodically pole the material, KTP satisfies all requirements for an efficient frequency converter.

In the next sections, we describe different techniques and show the state of the art of poling techniques and possible waveguide fabrication processes.

6.1.1 Poling Techniques

In the following, we will discuss different techniques to fabricate periodically poled structures in KTP. Several techniques have been reported for the fabrication of periodic domain structures so far. At this point, we will focus on the most important and applicable ones. These are; modulation of the spontaneous polarisation P_s during crystal growth [108], chemical domain inversion [109], electron beam writing [110] and electric field poling.

One conceptually simple technique is the direct growth of periodically poled crystals. During the growth process, the crystal grows with the same direction of the spontaneous polarisation as the seed crystal. By using a periodically poled seed crystal, the grown crystal will be as well periodically poled. The drawback of this method is the limitation to rather large periods and errors, like domain merging, due to dislocation site defects [108].

Another technique, which can only be used if the poling is combined with waveguide structures, is chemical poling [109]. In a rubidium nitrate melt waveguides can be made in KTP (compare to section 6.1.2). If barium nitrate is added to the melt, the barium leads to a domain inversion on the $-c$ face of the crystal. This inversion is limited to a small area close to the surface and also limited to large periods. Furthermore, the waveguide and poling properties cannot be optimised separately [111].

The method most commonly used is electric field poling. An electric field, above the coercive field strength, is applied to the sample and inverts the spontaneous polarisation [39]. By a structuring with an insulating material, e.g. SiO_2 or photo resist, periodic domain inversion can be achieved. This method has the advantage of fabricating thousands of uniform domains on a short time scale, in comparison to other methods. The challenge of this method is to find a switch-off criterion to stop the poling process, since this method is not self-terminating. For an efficient quasi-phase matched process, a 50:50 duty cycle between inverted and non-inverted domains is required. Techniques which can be used to monitor the poling process will be discussed in the next section 6.1.1.1.

6.1.1.1 Electric Field Poling Monitoring

One challenge of electric field poling is the switch-off criterion to achieve a well defined duty cycle. Several methods exist to monitor the poling process, e.g. switching current, accumulated charge, optical monitoring, and second harmonic generation monitoring. In the following, we describe different techniques that are commonly used and discuss their applicability to KTP as well as their benefits and disadvantages.

One simple technique is the optimisation of the poling process to a repeatable procedure. For samples with equal sizes and periods, the same number of pulses at the same field strength

should lead to comparable results. However, due to the inhomogeneity in ionic conductivity, coercive field strength, and potassium concentration of KTP wafers, this is not suitable. Each wafer needs different voltages and therefore different switching times.

A well known technique, used in lithium niobate poling, is the measurement of the accumulated charge. This method is based on integration of the displacement current to determine the spontaneous polarisation inversion progress. The accumulated charge Q for an inversion through the hole crystal is defined as two times the Area A multiplied by the spontaneous polarisation P_S of the material ($Q = 2 \cdot P_S \cdot A$). However, due to the intrinsic ionic conductivity in KTP the physical system behaves very differently to lithium niobate. When trying to measure the accumulated charge the measured signal will consist of a component due to the ionic conductivity and the true accumulated charge. It is not possible to distinguish between these two components because the electric field induces a localised heating that changes the resistivity of the material from pulse to pulse. This means that the component of the measured signal due to the ionic conductivity is not constant and therefore cannot be subtracted from the total signal. Thus, this technique is not suitable for KTP.

The method of second harmonic generation monitoring allows the direct measurement of the nonlinear response of the quasi-phase matched process. To apply this method, the material dispersion has to be known very well. Furthermore, for different poling periods, different light sources with different wavelengths are required, which limits the range of application. The reverse process, i.e. measuring the reduction of the birefringent phase matching, is also difficult. This is due to the unpoled areas at the border of the crystals, e.g. below an o-ring sealing, which contribute to the birefringent process and the minimum of the birefringent SHG won't be at zero.

An alternative method is optical monitoring. This method relies on the electro-optic effect and provides a signal that contains information about the inverted and non-inverted parts of the crystal. This method is independent of the poling period and can be used in both bulk and waveguide samples. A detailed description of this method is given in section [6.1.1.2](#).

6.1.1.2 Electro-optical Monitoring Technique

The electro-optical monitoring technique is a technique that directly probes the domain inversion of the material at a desired location and is suitable in virtually any material. Karlsson *et al.* developed this technique based on the transverse electro-optic effect [112], which we also expanded and used for monitoring directly in the waveguide. As we have already seen, KTP possesses a non-zero electro-optic tensor. Therefore, an electric field along the c-axis will lead to a modification of the refractive index along the b- and c- axes. This means that an electromagnetic wave passing through the crystal will experience a phase retardation that depends on the sign of the spontaneous polarisation and the amplitude of the applied electric field. For this reason, the application of an external poling field results in a differential phase retardation between electro magnetic fields polarised along the b- and c- axis. The differential phase retardation Γ can be described by equation 6.1:

$$\Gamma = \frac{2\pi}{\lambda} E \cdot L \left(\frac{n_b^3}{2} r_{23} - \frac{n_c^3}{2} r_{33} \right). \quad (6.1)$$

The phase retardation depends on the wavelength λ (in our experiments $\lambda = 633$ nm), the applied electric field in c-direction E , the length of the electrical contact L , the refractive indices n_b and n_c ($n_b = 1.771$ and $n_c = 1.865$) [113] and the electro-optic coefficients r_{23} and r_{33} (compare to section 5.6). At the wavelength of 633 nm they have values of $r_{23} = 15.17 \frac{\text{pm}}{\text{V}}$ and $r_{33} = 36.6 \frac{\text{pm}}{\text{V}}$ for KTP, respectively [38].

In combination with a linear polariser behind the sample, which acts as an analyser, the differential phase shift results in an intensity modulation. A linear variation of the electric field is transferred to a linear differential phase retardation. The intensity variation I shows a sinusoidal behaviour (compare to figure 6.1), and can be described as:

$$I \propto 1 - \cos^2(\Gamma(E)). \quad (6.2)$$

Figure 6.1 shows the intensity variation for different crystal lengths.

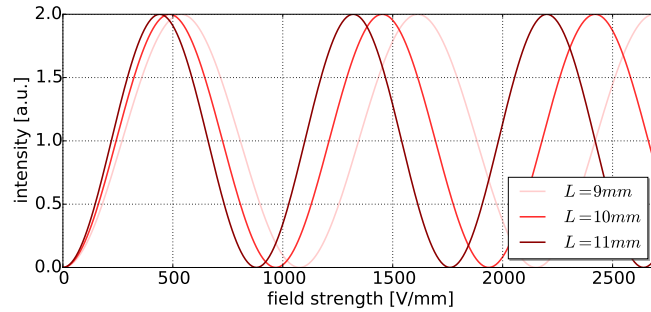


Figure 6.1 – Calculated intensity variation by differential phase retardation for various crystal lengths.

The electro-optical monitoring technique has the advantage of being simple and practical to use. This method is suitable for all poling periods where a duty cycle of 50:50 is required. Since this method probes the total phase difference acquired as the electric field passes through the crystal, it is not possible to gain information about different sections of the crystal [114]. However, a full cover electrode does not allow for a compensation of poling errors arising during the domain reversal process.

To analyse the poling progress, it is requisite to have the optical monitoring system built into the poling setup. As a linear polarised laser, we are using a Helium-Neon (He-Ne) laser at 632 nm wavelength. The laser beam is linearly polarised under 45° with respect to the b-axis of the crystal and launched along the a-axis through the sample (see figure 6.2). This configuration gives equal electro-magnetic field distributions in b and c-direction.

An electric field strength in the order of the coercive field strength leads to a phase retardation of more than 2π (e.g. for bulk crystals compare to figure 6.1), which leads to several complete oscillations. A linear polariser (lin. pol.) translates the phase retardation to an intensity modulation. The intensity signal is measured on a silicon photo diode (PD). The dependence of the optical signal on poling behaviour will be discussed next.

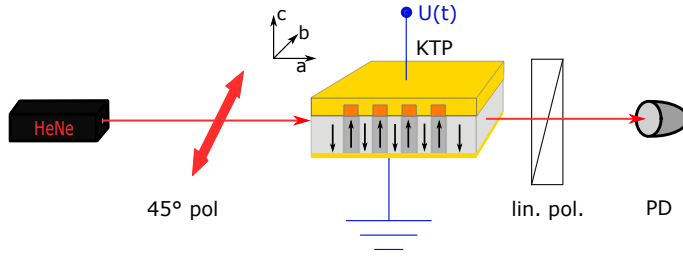


Figure 6.2 – Optical monitoring setup developed by Karlsson *et al.* [112].

Optical Monitoring Signal during Poling

An external electric field applied in the opposite direction of the spontaneous polarisation, above the coercive field strength, leads to a switching of the spontaneous polarisation. In the inverted region, the sign of the electro-optic tensor elements changes. In this case, equation 6.1 splits up into two parts.

$$\Gamma = \frac{2\pi}{\lambda} E \left(\underbrace{\left(\frac{n_b^3}{2} r_{23} - \frac{n_c^3}{2} r_{33} \right) \cdot (L - x)}_{\text{initial state}} + \underbrace{\left(-\frac{n_b^3}{2} r_{23} + \frac{n_c^3}{2} r_{33} \right) \cdot (x)}_{\text{inverted state}} \right) \quad (6.3)$$

Here, L is the length of the original orientation of P_s and x is the length of the inverted region with the opposite sign of the electro-optic coefficients (see figure 6.3). A separation of the sign in the inverted state leads to the following equation:

$$\Gamma = \frac{2\pi}{\lambda} E \left(\frac{n_b^3}{2} r_{23} - \frac{n_c^3}{2} r_{33} \right) \cdot \underbrace{(L - 2x)}_{L_{\text{eff}}}. \quad (6.4)$$

The result is a smaller accumulated phase retardation of the crystal, which is equivalent to a smaller effective length $L_{\text{eff}} = L - 2x$, with progressive polarity reversal. Figure 6.3 shows the effect of the reduced effective length on the optical signal. The oscillations vanish if the effective length is zero. Also, the effective length can be negative. This is the case if more than half of the spontaneous polarisation of the crystal is inverted. The more the spontaneous polarisation is inverted, the more the oscillations tend towards the initial number of oscillations. In the case of a complete reversal of the spontaneous polarisation, the effective length L_{eff} will be equal to $-L$.

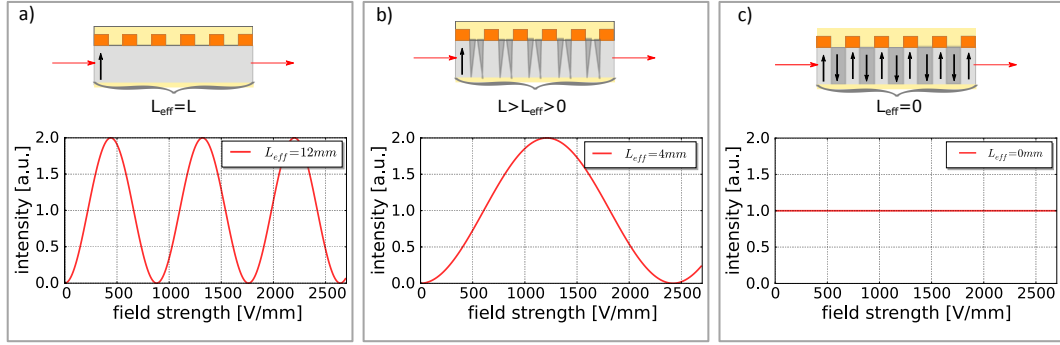


Figure 6.3 – Optical signal during the poling process. In figure a) no domain inversion within the crystal is present. Thus the effective length is equal to the crystal length. In figure b) the poling process has begun and the effective length is reduced to values between L and 0 . In figure c) the effective length is 0 , indicating the optimal time to stop the poling process.

The goal of the electro-optical monitoring technique is to find a switch-off-criterion, which can be used to stop the poling process at precisely the right moment. During the poling process, we apply several high voltage pulses to the sample with the shape like in figure 6.10. In the rising and the falling edge of the pulse we observe a number of oscillations. The shorter the pulse length, the larger is the number of pulses we need for the domain inversion. The larger number of pulses makes this method more accurate, having more data points. If there are no more oscillations in the optical signal, the effective length is zero and half of the crystal is poled (see figure 6.3c). In this case,

$$\Gamma = \frac{2\pi}{\lambda} E_z \left(\frac{n_y^3}{2} r_{23} - \frac{n_z^3}{2} r_{33} \right) \cdot \underbrace{\left(L - 2 \cdot \frac{L}{2} \right)}_{L_{eff}=0} \quad (6.5)$$

half of the poled region x is inverted and the differential phase retardation becomes zero. At this point, the phase change in the unpoled region and in the poled region cancels out, resulting in a total phase retardation of zero.

Whilst optical monitoring is a very versatile method that is well suited to KTP, one must also consider the limitations of this method. This technique does not spatially resolve the domain duty cycle since it is an averaging method. Inhomogeneous ionic conductivity, inhomogeneous shielding of the applied field by ionic space charges or variations in sample thickness may lead to inhomogeneous poling results that may not be sensed by optical monitoring (see figure 6.8). When choosing the poling parameters, we have to find a trade-off between pulse length and number of pulses. If the chosen pulse length is too long, it is difficult to determine the best switch-off time and can lead to an over-poling. Using several short pulses makes it more easy to precisely meet the switch-off criterion. However, a small number of long pulses leads to a more homogeneous poling result [58, 115].

6.1.2 Waveguide Fabrication Techniques

The fabrication of low loss waveguide structures in KTP has been under investigation for many years. Several attempts have been made to make waveguides in KTP. In the following section, we discuss the most important ones e.g. He⁺-ion implanting, laser writing, ion exchange and advanced techniques of these methods.

The implantation of He⁺-ions in KTP increases the refractive index, which can be used to fabricate waveguides. This technique was used by Zhang *et al.* in 1992 [116], who demonstrated SHG in planar waveguides. This is an interesting but cumbersome technique, due to the high optical losses [117].

Doumuki *et al.* made waveguides in a layer of Ta₂O₅ on top of KTP [118]. The layer of Ta₂O₅ on top of the sample shows no nonlinearity but guides the optical light field. Only the evanescent field inside the KTP crystal contributes towards frequency conversion, which drastically lowers the efficiency [118].

A relatively new but promising technique is waveguide fabrication in thin film KTP. A thin film of KTP is made on a substrate, like SiO₂, and afterwards diced or etched to form waveguide structures. These kind of waveguides have a potentially high confinement but still show very high losses [119].

A flexible and versatile fabrication technique is laser writing. A laser beam is focused into the KTP material while the sample moves under the beam to create channel waveguide by modifying the material properties [120]. It is based on a refractive index change occurring due to the elasto-optic effect and by stress induced birefringence and/or lattice modification [121]. Waveguides can be made in two different ways, in the modified region (type-I waveguides) or adjacent to it (type-II waveguides) [122]. The preferable type is the type-II waveguide, due to a reduction of the nonlinearity in the modified region. Laser written waveguides have potentially low losses and lead to a good confinement between two closely placed tracks [123].

The most common technique is a surface-near rubidium Rb (or other alkali ions, like caesium (Cs) or thallium (Tl)) ion-exchange which was first introduced by Bierlein *et al.* in 1987 [124]. The exchange of alkali ions has an impact on the dielectric properties as well as the ionic conductivity and the coercive field strength (see section 6.3.1). The concentration profile follows a complementary error function [124]. The high quality and the low losses make ion-exchanged waveguides an ideal candidate for guided optics [121]. It is possible to use more advanced techniques, both of them based on the rubidium exchange. Through an ion bombardment, for example by carbon ions, a modified layer in the crystal circumvents the exchange process. This can be used to manipulate the exchange profile to reach a more rectangular shape [125].

Another technique, which can be used to gain a larger refractive index increase between the waveguide and the surrounding material is a subsequent dicing of the rubidium exchanged material. With this technique, ridge waveguides can be realised [3]. However, the fabrication, especially the end facet preparation of such ridges, is a challenging task due to the brittle material [126]. Also the side wall roughness increases the waveguide losses. The advantages of these structures are a higher mode overlap and therefore an increased efficiency.

6.1.3 Characterisation Techniques

A fundamental understanding of the fabrication process requires a variety of analysis techniques. Some of these techniques can characterise the domain structure. These include, for example, the already described optical monitoring (see section 6.1.1.2), polarised light in crossed polariser, atomic force microscopy (AFM) or pulsed force microscopy (PFM). The most commonly used technique is a selective etching of the surface. Other methods are well suited for characterising the exchange properties of alkali ion doped KTP. Suitable methods are secondary ion mass spectroscopy (SIMS) and secondary neutral mass spectroscopy (SNMS) or energy dispersive X-ray techniques (EDX). The most powerful tools, which can be used for both the domain structure and the exchange properties, is confocal micro Raman microscopy. In the following, we will explain the fundamental ideas and compare the pros and cons of each technique. One simple and well known technique to check for a periodically poled structure in ferroelectric materials is phase-shift polarimetry [127]. This technique utilises two linear polarisers, one before and one after the sample, to analyse the stress induced birefringence in ferroelectric domain walls. The advantage of this technique is the fast and non-destructive measurement. The disadvantages are the low resolution of 5 μm and the low contrast in KTP due to relatively small domain walls, lower stress induced internal fields, and a weaker resulting phase change. This method is therefore not suitable for KTP characterisation.

Selective etching is a suitable technique to visualise the domain structures in ferroelectric materials. For many ferroelectric materials an etchant can be found which attacks the two crystallographic faces (+c and -c) with different speed. This transfers the domains structure in a surface profile to different physical heights. For KTP different solutions allow selective etching of the crystal facets. Two possible etchants are an aqueous mixture of KOH and KNO_3 [73] or an ammonium solution. Both attack the -c face more vigorously. The advantage of the method is the high resolution ($<1 \mu\text{m}$) and the short time to analyse the whole sample. The drawback of this technique, especially for integrated devices, is the increased surface roughness which also increases the losses of waveguide structures.

In secondary ion mass spectrometry a focused primary ion beam is used to analyse the composition of solid surfaces and thin films by sputtering the surface of the specimen. The generated secondary ions are collected and analysed with respect to the mass/charge ratios in a mass spectrometer. It is possible to determine the elemental, isotopic, or molecular composition of the surface to a depth of 1 nm to 2 nm. Due to the large variation in ionisation probabilities, this technique gives qualitative results. SIMS is the most sensitive surface analysis technique. Secondary neutral mass spectrometry analyses the generated neutral atoms. A big disadvantage of these methods is the destructive character. This limits the applicability as a standard analysis method in KTP [128, 129].

Energy-dispersive X-ray spectroscopy is an analytical technique for the elemental analysis or chemical characterisation of samples. It relies on an interaction of X-ray excitation and material. To generate characteristic X-rays from a specimen, a high-energy beam of charged electrons has to be focused into the sample (see figure 6.4). Within the sample, the incident electrons excite electrons in the inner shells and the X-rays generated by the recombination of these electrons are analysed. The intensity and energy of the emitted X-rays from a specimen are measured on an energy-dispersive spectrometer. As the energies of the X-rays are characteristic of the dif-

ference in energy between the two shells of the atomic structure of the emitting element, EDX allows the characterisation of the elemental composition of the specimen [130].

Raman spectroscopy is based on the inelastic scattering of monochromatic light when the frequency of photons changes upon interaction with a sample. A sketch of a confocal Raman setup is shown in figure 6.4. The photons of the laser light are absorbed by the sample and subsequently re-emitted. The frequency of the re-emitted photons shift up or down in comparison to the exciting monochromatic frequency. This effect is called the Raman effect. The Raman shift provides information about vibrational and rotational energies of molecular bonds. Raman spectroscopy is a convenient probe of the vibrational energy levels within a material which easily provides crystallographic fingerprints. The advantages of this technique is the easy sample preparation and the non-destructive method. Raman spectra usually contain sharp bands that are characteristic of the specific bonds in the sample. The intensity of the bands in a Raman spectrum is proportional to the concentration of the corresponding molecules and thus can be used for quantitative analysis. A drawback is the long measurement time, which makes it inapplicable for full sample characterisation [2, 131].

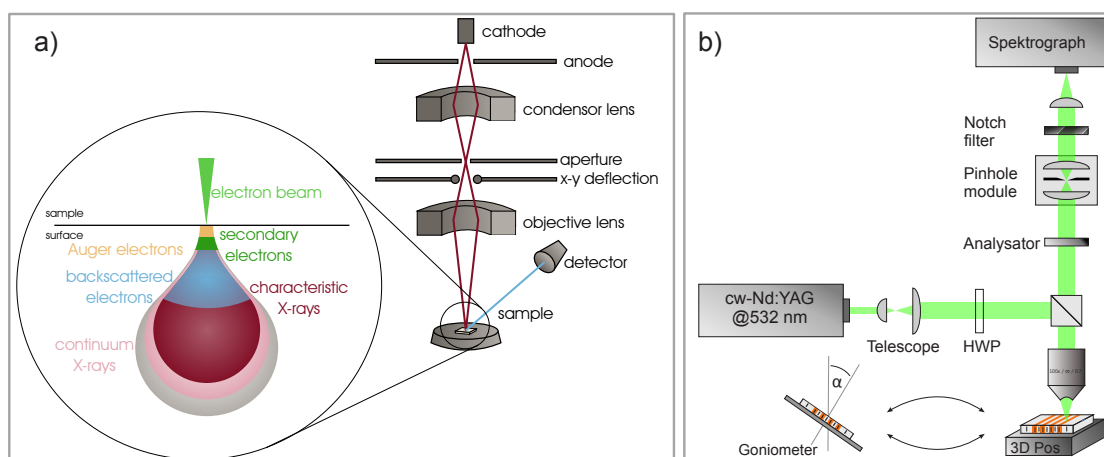


Figure 6.4 – Figure a) shows an illustration of a scanning electron microscope. The inset indicates the interaction volume of the electron beam with the sample and possible interaction processes [92]. In b) a sketch of the confocal Raman setup is shown [1].

6.2 In-house Processing

In the previous sections we introduced the state-of-the-art technologies and discussed the benefits and disadvantages of each one. Next, we select the optimal technologies for poling, waveguide fabrication and characterisation and describe our in-house setups and procedures for realising these technologies. Some of the technology is adapted from the existing lithium niobate setups and procedures, but many these elements required complete or partial rebuilding for the processing of KTP.

6.2.1 Chosen Technologies

We have introduced different techniques for poling, waveguide fabrication and their characterisation in KTP. Here, we summarise the most promising technology for each of these techniques. In our experiments we choose the poling technique by electric field poling. For our applications, this offers the most promising results with respect to fabrication effort, speed and accuracy. We can fabricate periods of roughly $8\mu\text{m}$ over the full sample length in a less amount of time without stitching errors, compared to electron beam writing.

For the waveguide fabrication, the Rb-exchange is the way of choice. We can fabricate uniform waveguides with relatively low transmission losses. In contrast to other options, the Rb-exchange should not decrease the nonlinear properties; which is crucial for nonlinear optical applications.

The analysis of the periodically poled samples is carried out by means of selective etching, which facilitates the characterisation of the whole sample in one step. The exchange properties are characterised by EDX. Periodically poled waveguide structures pose a particular challenge in terms of analysis. Here, the versatile Raman spectroscopy is used.

6.2.2 Periodic Poling

In this section we explain our processes and techniques to periodically invert the spontaneous polarisation of KTP. It was previously stated that the chosen method would be electric field periodic poling. However, there are many ways to achieve this process. There are many options for what type of electrode to use and what insulating mask to use. Now, we investigate a few of these options and report on the results and detail the experimental setups used to achieve these processes.

6.2.2.1 Insulating Layer Structuring

Regardless of the electrode material, that will later be used, an insulating layer is required to define the areas where domain inversion is desired. An insulating material prevents surface charge compensation and creates a small variation in the electric field strength, which prevents the domain inversion. The insulator material can be for example a photo resist or a dielectric material e.g. SiO_2 . In this case we are using a photo resist as an insulator. The resist is a positive resist (AZ 4533), which we spin at 5000 rounds per minute (rpm). This creates a resist thickness of $3\mu\text{m}$, which is sufficient to insulate the sample and allow a periodic poling.

Due to the small dimensions of the samples, the effect of bulge formations along the sample edges causes a relatively large gap between the photo mask and the inner area of the sample. An edge grinding, a standard technique in LN technology, is not suitable because of the small sample size. Our solution to overcome this problem is a double step lithography. In a first step, we illuminate and develop (which is equal to a removing) the bulge. We cover the inner region with an aluminium mask (compare figure 6.5).

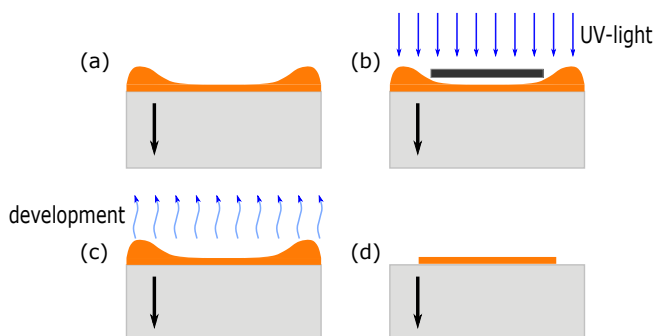


Figure 6.5 – Schematic sketch of process steps applied in order to remove the resist bulge on KTP.

In a second lithography step, we transfer the desired structures from the photo mask into the photo resist (see figure 6.6(a)-(c)).

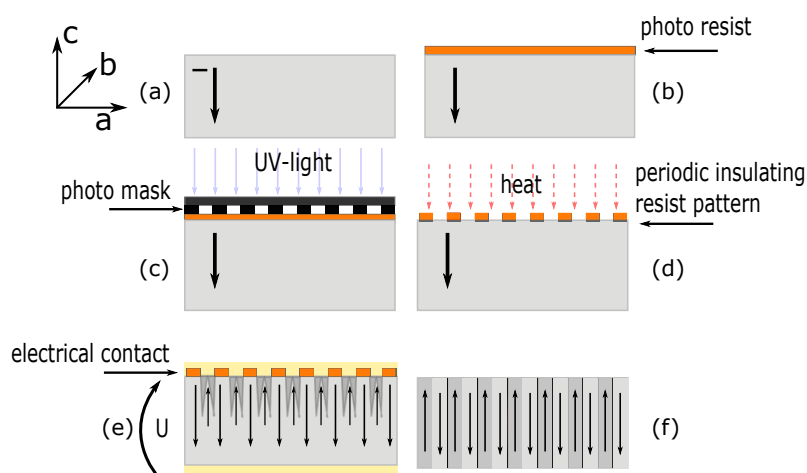


Figure 6.6 – Schematic of technological steps in the production of periodic domain inversion in KTP.

A metal ion free developer (MIZ 726) removes the illuminate photo resist. A baking step (see figure 6.6(d)) above the flowing temperature of 130 °C makes the photo resist more resistant against the electrolyte and changes the shape of the structures to a more roundish one. We sputter on the back side of the crystal a thin layer (80 nm) of gold palladium (Au/Pd) to create

the electrode (see figure 6.6(e)). The opposite side is either coated with a metallic layer, or, in case of waveguide poling, directly contacted by an electrolyte. For periodic poling, we applied several high voltage pulses (see figure 6.6(e)-(f)).

A further benefit to this technique is that it provides a spatially invariant electric field across the entire sample, that allows for the optical monitoring technique during poling. The optical monitoring technique requires an electric field distribution over the whole sample, which makes finger electrodes inapplicable. To fulfil this requirement, we are using a full cover electrode, which allows for nearly similar electric field components in the poled and unpoled regions in the crystal. This is needed determining the switch-off criterion (see section 6.1.1.2).

6.2.2.2 Metallic Electrode Poling Holder

The easiest and simplest way to apply the voltage to the sample is through direct contacting of both sides of the sample by a metal layer and a soft-pad (see figure 6.7). This soft-pad consists of foam rubber and silver plated copper particles. These particles induce an electrical conductivity in the rubber with a specific resistance of $0.005 \frac{1}{\Omega \text{ cm}}$ [132]. This technique was used previously. However, this is not the way of choice for periodic structures because of a low conductivity in the photo resist gaps and a voltage drop along the metal layer. Therefore the poling results are inhomogeneous (compare figure 6.8a)). Furthermore, the electrical insulation was a challenging task, the size of the soft-pad had to be limited to the inner part of the sample to prevent arcing.

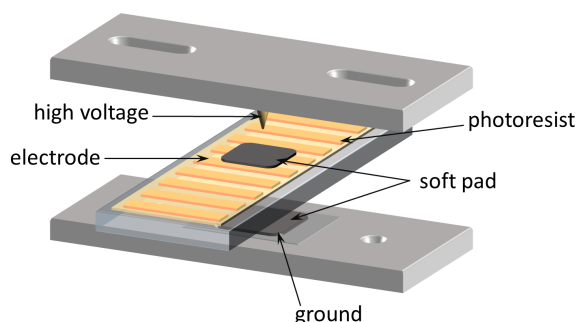


Figure 6.7 – Previously used sample holder for poling. Here, metallised KTP samples are contacted via gold wire and conductive soft-pads.

This technique is well suited for poling experiments without any photo resist, e.g. conductivity measurements or analysis of the coercive field strength. We used this technique for the analysis in section 6.3.1.

The metal electrode and a soft-pad (section 6.2.2.2) show an overpoling below the soft-pad, which means the domains are too broad (see red bar in figure 6.8a)). On the other hand, the outer regions are underpoled. This happens, because of the integrative method of the optical monitoring. For the whole sample, half of the crystal is inverted the other half not, even in an inhomogeneous manner.

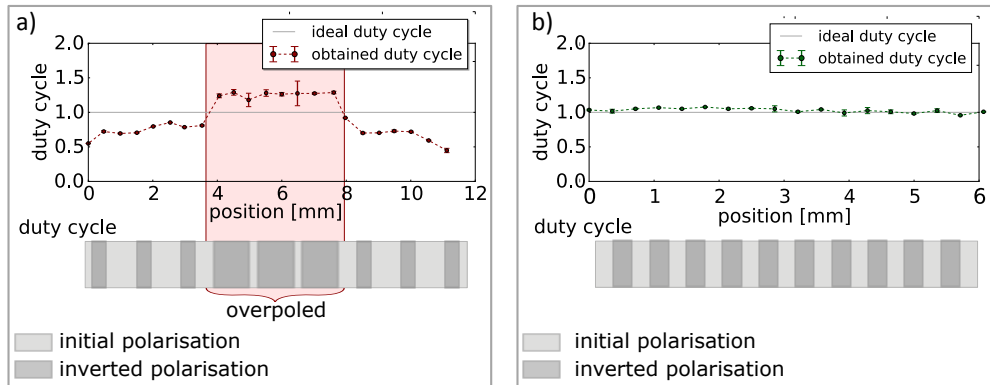


Figure 6.8 – Variation of the duty cycle over the sample. Figure a) shows the duty cycle obtained with the former poling holder using metal electrodes and a soft-pad. In the centre the sample is overpoled, while the outer parts are underpoled. Figure b), the use of the liquid electrode sample holder results in more homogeneous outcome.

6.2.2.3 Liquid Electrode Poling Holder

Instead of using a metal electrode, it is possible to use a liquid electrode. For this method, a new poling holder had to be constructed (compare to figure 6.9). The new poling holder has two parts, one to contact the bottom of the sample and the other to contact the top. The bottom part realises the contact via a metallised soft-pad while the top is contacted via an electrolyte sealed with an o-ring. The electrolyte is necessary for good electrical contact in the small slits of the poling pattern. The holder is designed such that the required laser fields in the optical monitoring are not blocked. The sample holder is affixed to a 3-axis tower, which allows an alignment of the sample to the laser beam. To fasten the sample in place, we screw the upper part of the sample holder on the lower part. The two halves of the holder are electrically connected in order to close the electric circuit. The soft-pad distributes the forces and reduces the risk of breaking or damaging the sample. This is necessary because of the o-ring sealing of the electrolyte in the upper part, which contacts the sample and the upper copper electrode.

The electrolyte consists of deionised water, isopropyl alcohol (IPA) and a salt to increase the electrical conductivity. IPA decreases the surface tension, that allows better flow of the electrolytic solution in the narrow structures of the poling pattern. For the poling experiments of KTP, we use KCl which decays into a K^+ cation and a Cl^- anion. The choice of a potassium-based electrolyte is to ensure no material modification at the surface of KTP. We measured in a mixture of 89% H_2O + 10% isopropyl alcohol (IPA) + 1% potassium chloride (KCl) a conductivity of $\sigma_{\text{electrolyte}} = 3 \frac{\text{mS}}{\text{cm}}$. For this composition, we determined a resist solubility of $55 \frac{\text{nm}}{\text{min}}$ and a surface tension which is a factor of 1.8 lower than that of water.

The electrolyte has an ionic conductivity, which is an important property for waveguide poling. Since we are using the differential phase retardation of an optical field, an electronic conductivity would absorb the light and makes an optical monitoring directly inside a waveguide impossible.

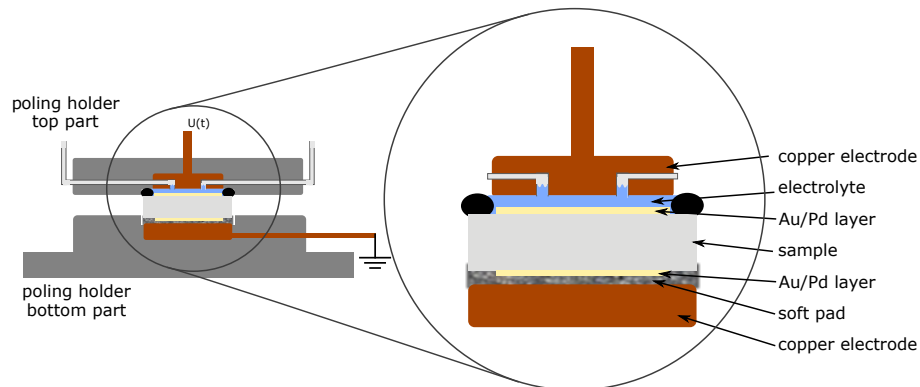


Figure 6.9 – Sketch of the new developed liquid electrode poling holder.

The domain inversion observed using the liquid electrode was much more homogeneous than using the metal electrode. Figure 6.8b) shows the duty cycle over the entire sample length varies by less than 8%. One challenge we have observed is the degradation of the photo resist when in contact with the liquid electrode. After ten minutes of contact the photo resist was seen to flake off which leads to a poor poling homogeneity. It is very difficult, albeit possible to achieve periodic poling on this time scale. Therefore, an alternative mask, consisting of SiO_2 , was investigated in the hope that would give more time for the processing.

SiO_2 Mask

We also investigated SiO_2 as an alternative insulating layer during the poling step. In contrast to the photo resist layer SiO_2 is not expected to degrade in the presence of the electrolyte. SiO_2 layer was deposited and patterned by a subsequent lift-off technique. The SiO_2 mask has the advantage that the mask can remain on the sample after poling and act like a protection layer, e.g. for end facet polishing. Since the ionic conductivity is driven by an electric field, an insulation layer does not affect the conductivity in the material, therefore the SiO_2 will not lower the ionic current.

A disadvantage to the SiO_2 mask is the problematic analysis of the periodically poled structure, because it is not possible to selectively etch the surface. For this reason, we have to use Raman spectroscopy, which takes a lot of time and only gives information about very small areas. Therefore, an SiO_2 mask is not well suited for preliminary studies and prototyping of poled KTP devices, but offers interesting potential for future sample fabrication.

6.2.2.4 Experimental Setup for Periodic Poling

For the periodic inversion of the spontaneous polarisation in KTP, a new poling setup was required. Due to the ionic conductivity in KTP, the “self-limiting configuration”, that is typically used in lithium niobate setups [15] is no longer suitable. Instead, we use a direct connection scheme, where the high voltage is directly connected to the sample. In contrast to the self-

limiting configuration, one can significantly exceed the coercive fields strength of the connected sample. This direct connection scheme has also exhibited tremendous performance for LN, where poling periods down to $1.7 \mu\text{m}$ have been demonstrated [133].

The key part of the poling setup is the high voltage amplifier *Trek 20/20C*. This amplifier can generate high voltage pulses of $\pm 20 \text{ kV}$ with a maximum current of 20 mA . The amplifier operates in two different modes. In the clipping mode, the high voltage is switched off, if the output current is higher than a set threshold. For our experiments, we use the limit mode. In the limit mode, the amplifier acts as an current source and reduces the output voltage to fulfil the current limitation.

The *Trek* amplifies an input signal by a factor of 20. This input signal is generated in our self made poling program and behaves like the pulse shown in figure 6.10. The rising and falling edge of the electric pulse follow a linear slope from zero to a set voltage within 1 ms . The data acquisition software records simultaneously the voltage and the current provided by the amplifier as well as the optical signal, used for the optical monitoring technique (compare to section 6.1.1.2). The poling takes place mainly during the plateau region, if the voltage is higher than the required coercive field.

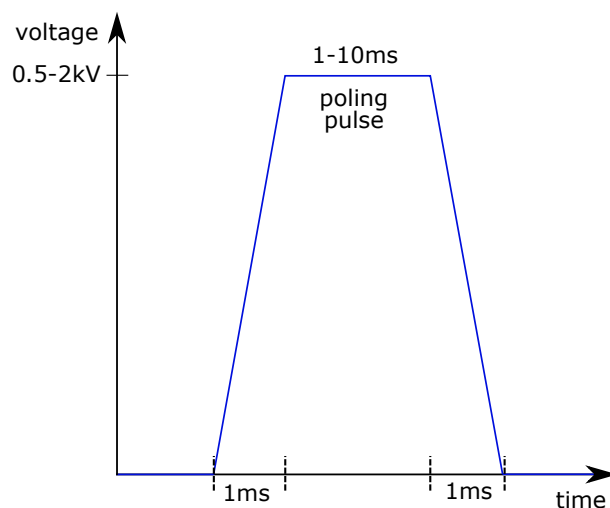


Figure 6.10 – Sketch of the high voltage pulse used for bulk and waveguide poling. In the rising and falling edge of the pulse the optical monitoring is done.

6.2.3 Waveguide Fabrication

In this section we focus on our techniques and processes to fabricate Rb-exchanged waveguides in KTP. Vertical confinement is achieved due to the increased refractive index from the Rb-exchange. To obtain horizontal confinement, it is possible either to create a ridge by dicing the crystal, or to create channel waveguides with a selective Rb-exchange through the slits of a mask deposited on the surface of the crystal.

In the following section, the waveguide fabrication setup will be described. The techniques are

in theory independent for the crystallographic faces and can also be used for any direction of waveguide, however the parameters, i.e. temperature, time and melt composition, have to be adjusted to the specific face.

6.2.3.1 Potassium Treatment

We already discussed the impact of potassium vacancies on several properties of the KTP crystal, e.g. the ionic conductivity or the challenging poling concerning homogeneity and monitoring. O. Driesner implemented a potassium treatment procedure, which increases the homogeneity and lowers the overall ionic conductivity [75]. During this procedure, the samples are immersed in a pure KNO_3 bath at a temperature of 375°C for 24 h. We use this technique to homogenise the wafer before the first fabrication step, like poling or waveguide fabrication. For our experiments, we use the optimised sample holder and treatment step as described in section 6.2.3.2.

6.2.3.2 Exchange Setup

In this section, we describe the exchange setup for the Rb-exchange. The original setup for a rubidium ion exchange in KTP was built by H. Suche and H. Rütz (compare [75]) and optimised by C. Eigner, M. Santandrea and R. Ricken. The setup itself consists of a heating plate, on which we place an *Alsint* (Al_2O_3) crucible (see figure 6.11). *Alsint* is a passive and stable material, which does not interact with the strongly oxidising nitrate melt. In the crucible, we melt a mixture of RbNO_3 , KNO_3 and $\text{Ba}(\text{NO}_3)_2$. The ratio depends on the specific application. In our experiments we use a mixture of 97% RbNO_3 , 2% KNO_3 and 1% $\text{Ba}(\text{NO}_3)_2$, which can be used to fabricate single-mode waveguides at 1550 nm (at an exchange time of 60 min at 330°C) or at 800 nm (at an exchange time of 5 min at 330°C).

The setup also includes a rack, consisting of two threaded rods and a crossbeam, holding the sample holder. We use a grip to lower the cross beam and immerse the sample holder into the melt in a precise and controlled manner. A detailed description of this crucial step is discussed in section 6.2.3.3. To automate the lowering process, it is possible to add a computer controlled stepper motor instead of the grip. For a homogeneous exchange, we rotate the holder and improve therefore the exchange of the melt close on the surface of the KTP sample. The sample holder consists of two pieces. We place the sample on the base plate and fix it by tightening the top part of the sample holder (see inset in figure 6.11). Through drilling holes, the melt reaches the sample. On the lower part of the base plate, melt swirls mix the melt during rotation and thus homogenise the temperature distribution in the melt itself. It should be noted, that the lid allows an exchange of the melt on top of the sample. We monitor the temperature with a steel covered thermocouple. To prevent an oxidation of the steel, we place the thermocouple in an *Alsint* case. The melt shows a temperature variation of less than 2 K, which is in the error margin of the thermocouple. The temperature decreases from the melt surface to the top of the crucible by 150 K (compare to temperature-bar in figure 6.11). During the exchange, the crucible is covered by a lid to keep the temperature conditions during the exchange process constant.

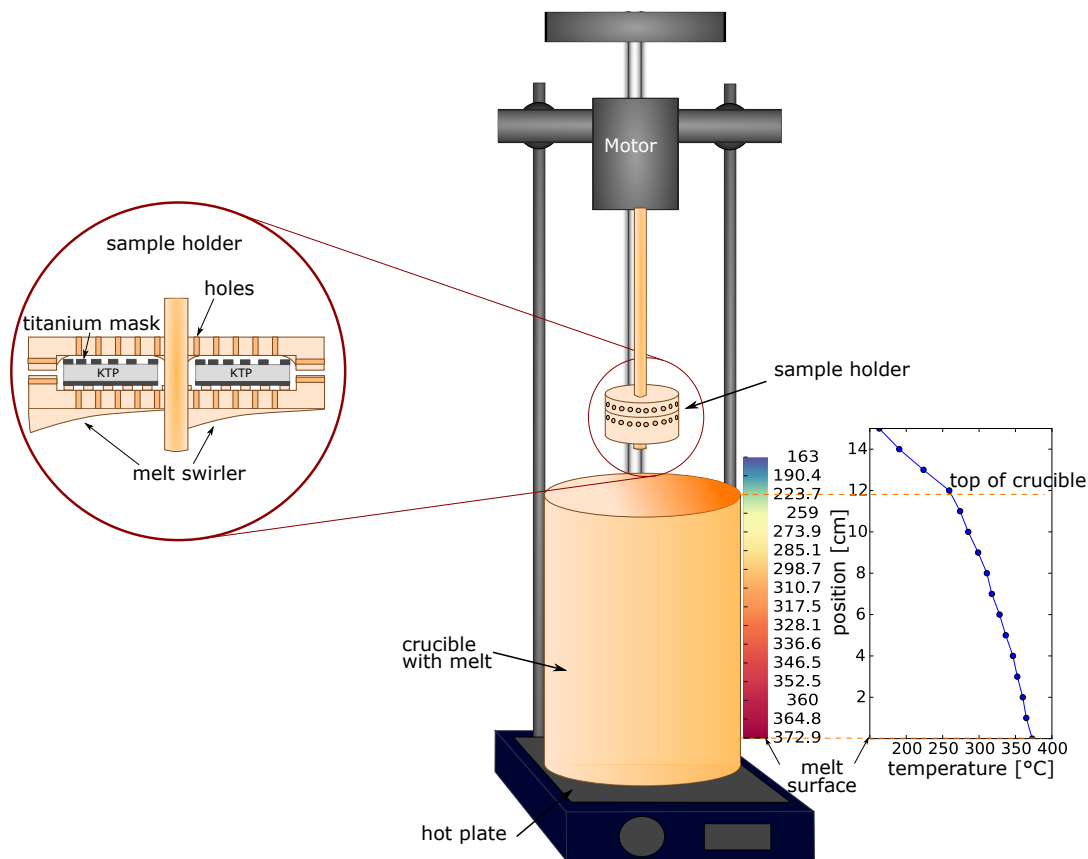


Figure 6.11 – Schematic sketch of the exchange setup for Rb-ion exchange and the potassium treatment.

6.2.3.3 Exchange Procedure

The fabrication of waveguide structures requires a specific sequence of events. We established a standard procedure to do the exchange with a maximum yield. The critical parameter, which leads to a breaking of the sample is the temperature gradient. To minimize the gradient, we lower the sample holder stepwise and wait at each position for a specific amount of time to equalise the sample holder and the ambient temperature. The procedure is done as explained in table 6.4. At first, we heat up the sample above the crucible for 20 minutes and during this time open the lid of the crucible slowly to keep the temperature gradient as small as possible. Afterwards, we lower the sample holder below the edge of the crucible, in the middle of the crucible and directly above the melt and wait at each position for 10 minutes to equalise the temperatures. Before inserting the holder and the sample into the melt, we slightly touch the melt surface with the holder to equalise both temperatures. After this procedure, we immerse the holder and the samples into the melt. During the exchange, we rotate the sample holder to swirl the melt, which leads to a homogeneous temperature distribution. Furthermore, the swirling keeps the melt composition constant at the sample to melt interface during the exchange. We

Table 6.4 – Sequence of process steps for Rb-exchange and K-treatment.

	position	temperature [°C]	time [min]
1	above the crucible	160	20
2	below crucible edge	225	10
3	middle of crucible	310	10
4	above melt	365	10
5	touching melt	370	5

remove the sample after successful exchange (typically 1h 330 °C) by reversing the steps 1-3 in table 6.4. This procedure is optimised for producing single-mode waveguides at 1550 nm (SM1550).

For the fabrication of single-mode waveguides at 800 nm (SM800), one could in theory either reduce the melt temperature or the exchange time. Given that the melt is already close to the solidification point, the only possibility is to reduce the exchange time. To achieve single-mode waveguides at 800 nm, the exchange time has to be reduced to 5 min. The fabrication of SM800 waveguides is more critical than for SM1550. The short exchange time required for the processing means that any timing error for the interruption of the exchange results in a different waveguide depth. Moreover, during the removal of the sample from the crucible the temperature is high enough to induce some thermal annealing, thus modifying the waveguide profile. To overcome this problem, we remove the samples only doing steps 1 and 2 (compare table 6.4). However, this approach reduces the yield due to the larger temperature gradient and therefore a higher breaking rate of the samples.

6.2.4 Channel Waveguides

Using a selective Rb-exchange through the slits of a mask deposited on the surface of the crystal, one can define channel waveguides. The structure of the resulting waveguides will depend critically on the structure of the mask used during the exchange process. It is therefore important to optimise the mask design and fabrication. Once the channel waveguides are defined, the end facets are polished to ensure efficient light coupling.

6.2.4.1 Exchange Mask Definition

The simplified fabrication steps for the channel waveguides exchange mask are shown in figure 6.12. The material of choice for the mask is titanium, due to the high stability against the strong oxidising effect of the nitrates. Other materials, like aluminium have been tested but resulted in holes in the metallic layer. First, we deposit a 80 nm layer of titanium on the exchange face. Above the titanium layer, we pattern the mask layout with a photolithographic procedure, in a similar fashion as for the fabrication of periodic structures. After illumination and development, this pattern will be transferred to the titanium via an etching step. These slits have different

widths between 1.5 μm to 4.5 μm . The full mask layout is shown in figure 6.13. The back side of the sample is also protected by a titanium layer. This is necessary because the larger ionic radii of Rb changes the size of the unit cell, which leads to a macroscopic expansion and therefore to a bending of the sample. This bending causes a low yield due to larger breaking probability during the polishing process.

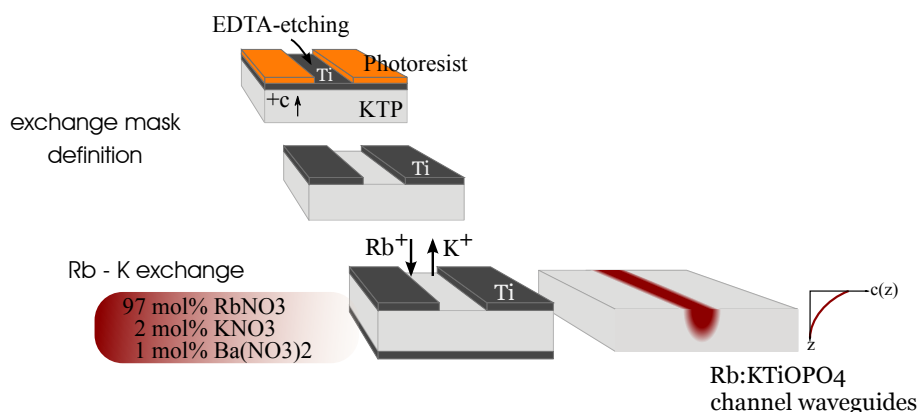


Figure 6.12 – Process steps to fabricate a hard mask, structuring the areas for rubidium exchange.

The titanium mask has to be removed after the exchange process. One solution for a permanent mask is the fabrication of SiO_2 exchange masks. For this mask a lift of process is preferable, because solvents which attack SiO_2 also attacks KTP and therefore lead to an increased surface roughness. This kind of exchange mask protects the crystals surface and reduces scratches. However, an SiO_2 mask is not well suited for preliminary studies and prototyping of KTP waveguides because of the protection layer. But it offers interesting potential for future sample fabrication.

6.2.4.2 Waveguide Endfacet Polishing

After producing the waveguides, the next step is to polish the end facets. Polishing is required before the poling step because the optical monitoring requires good coupling to the waveguides/bulk, and this can be achieved only if the end facet is a smooth surface.

The polishing before the bulk poling procedure is not that critical, since the edge of the sample is not important. For the waveguide poling and the finish polishing, as the last step before the coating and/or the optical experiments we have to take care of the end facet edges. The waveguide itself has a exchange depth of 5 μm to 10 μm . This depth is the region of interest during the waveguide polishing. Here, we have to press a second sample top side down on the waveguide sample to reduce the edge rounding.

We had to improve the polishing technique, which is well developed for LN in our group, to achieve good end facets without damaging the samples surface. In the standard process, the two samples pressed together. Since the waveguides are slightly higher than the bulk material,

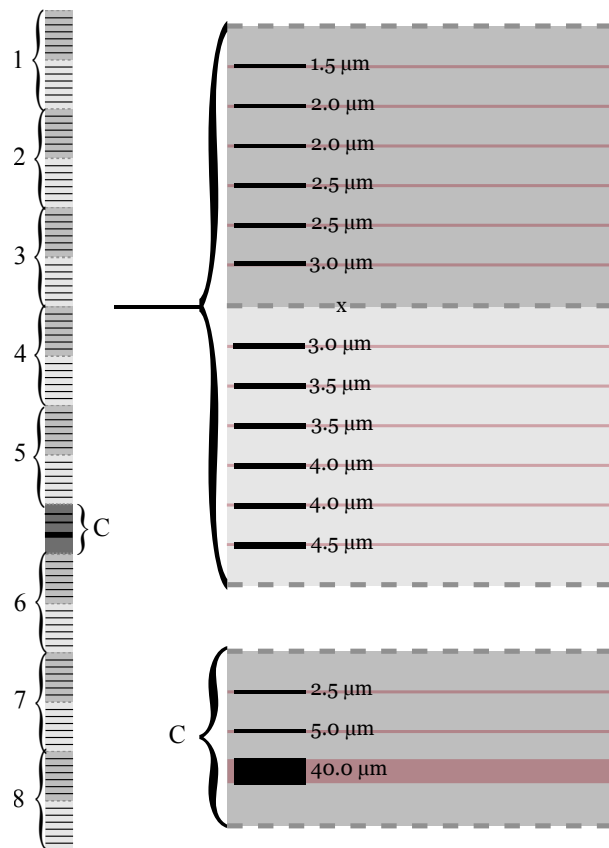


Figure 6.13 – Overview of the mask layout. The mask consists of 8 groups, each with 12 waveguides, of varying width from 1.5 μm to 4.5 μm .

because of the rubidium exchange, the highest pressure and the first contact is on the waveguide itself. If these samples are pressed together, the force is such high, that we get a bonding effect. By removing the upper sample, we destroy the waveguide (see figure 6.141b) and 2c)). This damage leads to increasing waveguide losses of 5 dB/cm. A buffer layer of SiO_2 reduces the pressure and reduces also the damaging. The hardness of pure SiO_2 transfers the stress to the waveguide. To release the pressure, a thin layer of photo resist is spin coated between the two samples. With this technique, the surface of the samples looks much smoother, which can be seen in the losses of the waveguide. Losses of 0.2 dB/cm at 1550 nm and 1.2 dB/cm at 800 nm could be measured (compare to section 8.3.3.2).

The polishing is done in a combined physical and chemical polishing process with alkaline colloidal silica (*Logitec SFI* [134]). The sample is mounted in a polishing holder, which is placed in an additional holder. The two holders can rotate independently, which leads to a homogeneous polishing without any directional dependency. Both holder are fixed on a polishing plate. This plate rotates and an aqueous solution of the *SFI* polishing solution drips with roughly 1 drop per second on the polishing plate and forms a thin layer. The polishing time for one end facet is between 2 h and 6 h. Because of the short length of the samples, it is difficult to adjust

the sample end facet perpendicular to the waveguide. Using a back reflection technique, we measured a typical angle error between the end facet and the waveguides of less than 1° . This polishing technique is the best to polish exchanged waveguide samples. For diced waveguides (see next chapter) it is not suitable to use a polishing and we had to find a different way to prepare the waveguide end facets.

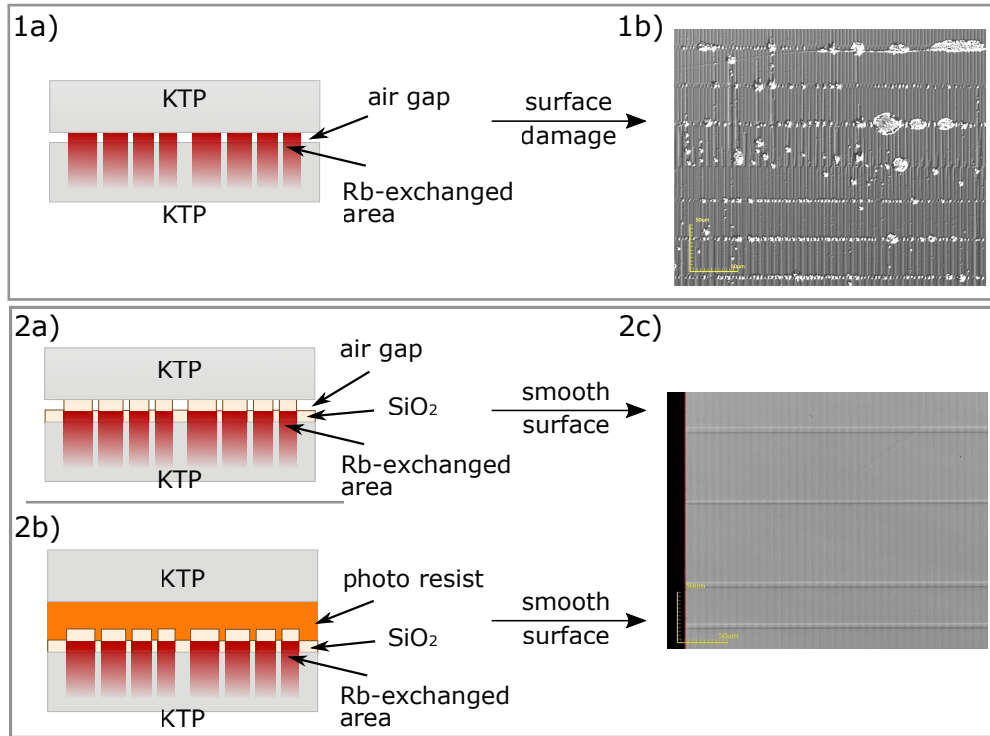


Figure 6.14 – Figure 1a) Sketch of the previous polishing technique with direct contact between waveguides and the second sample. Figure 1b) shows a microscope image of the waveguide structures with damages, intersecting the waveguides. Figures 2a) and 2b) show the optimised polishing process with additional SiO₂ and SiO₂ + photo resist, respectively. In figure 2c) a microscope image of the waveguides after polishing is depicted, showing no defects on the surface.

6.2.5 Ridge Waveguides

An alternative technique to channel waveguides through exchange patterning is ridge waveguide achieved by a dicing process. This was undertaken with Prof. Kip's group at the Helmut Schmidt University Hamburg. After a planar rubidium exchange, the confinement in the lateral direction is achieved by a subsequent ridge dicing (see figure 6.15).

Ridge dicing is challenging because the area in which the rubidium exchange has occurred is very brittle and also bends. For a successful dicing, a planar base plate is required. For this, we have to polish or rather dice the back side of the crystal. After the back side preparation, we made ridges along the a-direction of the crystal with a diamond blade (Disco Corp. G1A853 SD6000 R21B01). This dicing has been performed in Hamburg by Martin Volk and Christian Haunhorst.

The resulting brittle material after the exchange is susceptible to chipping during the dicing step and makes polishing impossible. Because of this the end facets are prepared with the dicing saw which gives much poorer end facet quality.

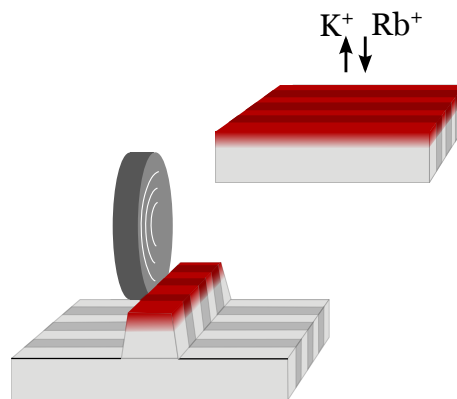


Figure 6.15 – After the planar rubidium exchange, the ridges are prepared in a subsequent diamond blade dicing process.

6.3 Poled Waveguide Results

This section comprises the results of KTP characterisation and device fabrication. We start with a material analysis in which we investigated the basic material properties, e.g. material absorption, ionic conductivity, poling behaviour and gray tracking mechanism. Then, we discuss two different fabrication sequences, either fabricating waveguides in periodically poled material or periodically pole waveguide structures. We show and compare the outcomes for both sequences and discuss the most promising technique.

6.3.1 Doped and Undoped Bulk KTP Properties

Before the fabrication of periodically poled waveguide structures, we have to analyse and understand the material properties of KTP. We characterised several properties, like the optical absorption of the material, the ionic conductivity, the coercive field strength and the gray tracking behaviour. We investigate these properties in a number of different samples in the hope of gaining some understanding of the effect that Rb-doping has on the material properties. We investigate KTP, potassium titanyl arsenate (KTA), RTP and RKTP, a commercial KTP crystal which contains 1.5% Rb doping in the bulk material.

6.3.1.1 KTP Absorption Characteristics

The absorption of the material, especially the absorption edge is an important parameter for conversion experiments in the UV regime. We characterised the absorption in KTP, RKTP and RTP by transmission measurements in a UV-VIS-IR spectrometer (*Agilent Carry 5000*). Since KTP is a biaxial birefringent material, we had to measure the transmission with polarised light. The transmission varied among different material types and among KTP samples in the visible and the UV regime. We show transmission spectra from 500 nm to the bandgap absorption edge. Typical KTP transmission spectra on the UV absorption edge for different polarisation directions are shown in figure 6.16. The cut-off wavelength is different for the distinct polarisations, with the shortest wavelength for the refractive index n_c and the longest for n_a .

In addition to the pure KTP samples, further samples with different Rb compounds were available. We compared two samples with different Rb content with pure KTP crystals. A comparative study of n_a between KTP and one sample with 1.5% Rb content (RKTP) and another sample containing 100% Rb (RTP) compounds was made. The visible-to-UV transmission spectrum for each sample is shown in figure 6.17.

The absorption edge in the UV regime is generally attributed to absorption in Ti-O subgroups [135]. No clear trend is observable in samples with different concentrations of dopant. The RTP crystals shows the lowest transmission and the lowest absorption edge compared to the other materials. Hanson *et al.* observed the same behaviour in RTP crystals and attributed this effect to a lower crystal quality due to other constituents in the flux during the crystal growth process. Such constituents, e.g. molybdate and tungstate compounds, allow a reduction of the growth temperature and lowers the viscosity and volatility of the flux and facilitate a faster growth rate [136]. However, the impurity level of the crystals improves, which therefore explains the decrease of the transmission [137]. RKTP crystals show the highest transmission and the longest

absorption edge. Such crystals are commonly used in bulk applications due to the low gray tracking occurrence. Because of that, the growth process is optimised and crystals with low imperfections and impurities can be grown.

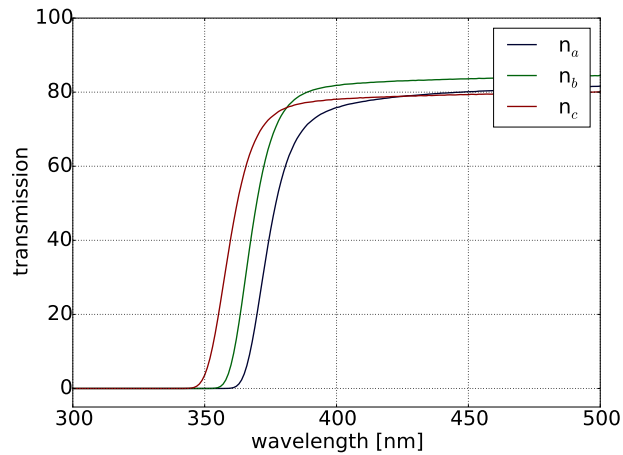


Figure 6.16 – Polarisation dependent absorption edge in KTP.

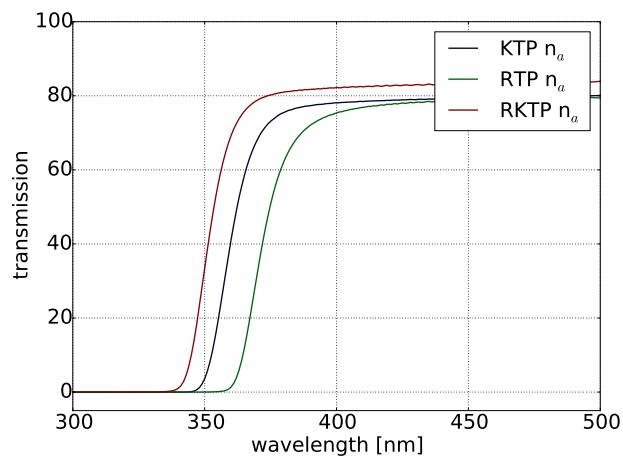


Figure 6.17 – Absorption edge for KTP, RKTP and RTP substrates.

6.3.1.2 Ionic Conductivity Characteristics

The characterisation of the ionic conductivity is a key parameter to understand the poling behaviour of the material. Furthermore, the maximum area which can be periodically poled is limited by the maximum current of the amplifier and the ionic conductivity of the sample. Therefore, a lower conductivity allows for larger samples sizes to be periodically poled. We had

the possibility to characterise different kinds of materials. e.g. KTP, KTA, RTP and RKTP. From former investigations [138], we know the ionic conductivity does not show an ohmic behaviour. The conductivity increases in a nonlinear way with an increasing electric field strength. For that reason, it is important to measurement and compare different values and materials at the same field strength. Comparing different materials, KTA exhibits the highest ionic conductivity of $\sigma_{\text{KTA}} = 658 \frac{\mu\text{S}}{\text{cm}}$ (see orange line in figure 6.18). One reason could be a higher concentration of potassium vacancies. Pure KTP shows, compared to KTA, a reduced but to Rb-doped material a relatively high ionic conductivity of $\sigma_{\text{KTP}} = 44 \frac{\mu\text{S}}{\text{cm}}$ (see blue line in figure 6.18). A small amount of Rb doping (roughly 1.5%) lowers the ionic conductivity to $\sigma_{\text{RKTP}} = 2 \frac{\mu\text{S}}{\text{cm}}$ (see red line in figure 6.18).

A simple explanation is the larger ion radius of Rb-ions with respect to K-ions. The ions have to move through a bottleneck of tetrahedral and octahedral a long a one dimensional chain (compare section 5.3.3). Therefore, the activation energy of Rb, which is necessary to move along the one dimensional chains is higher than for K-ions. If a chain is already blocked by one Rb-ion, it is also blocked for K-ions which cannot move along the c-axis anymore, the overall ionic conductivity is reduced. Increasing the Rb concentration to the maximum value (this means a complete exchange of K against Rb; going from KTP to RTP) the conductivity lowers only a small amount, because the already blocked chains are no longer relevant for the ion movement. The different behaviour of the conductivities has to be considered during the periodic poling. We will discuss this later in section 6.3.3.2.

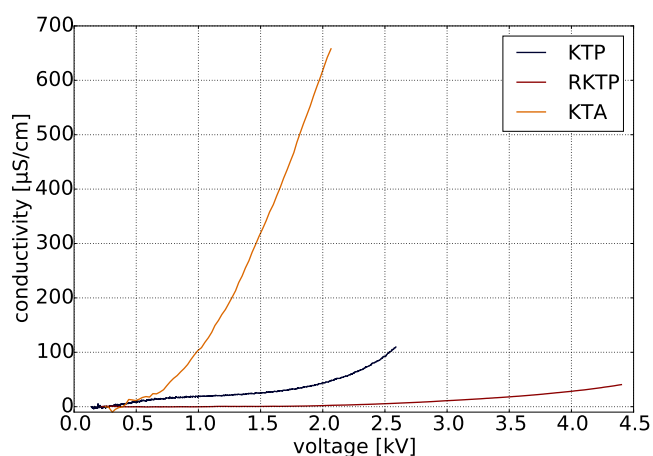


Figure 6.18 – Measured ionic conductivities for KTA, KTP and RKTP.

One possibility to reduce the overall ionic conductivity in KTP is a potassium treatment in pure KNO_3 (compare to 6.2.3.1). To compare KTP wafer from 2011 (*roditi*) with the newer one from 2014 (*bright crystals technology* (bct)), we measured the ionic conductivity for as-grown, annealed and potassium treated wafer. For a comparison to other experiments [75], we measured the conductivity at 500 V. In KTP material, we bought in 2011, it is possible to reduce the ionic conductivity by one order of magnitude [75]. A thermal annealing, which could homogenise

the ionic conductivity distribution of the wafer, does not result in a lower conductivity (compare to figure 6.19). In newer material, we bought in 2014, the ionic conductivity is already lower than the material ordered in 2011 at *roditi* after the potassium treatment. We didn't see an effect on the homogeneity or the absolute number of the conductivity after an annealing or a potassium treatment (compare figure 6.19). Therefore this method is not suitable to reduce the ionic conductivity any more.

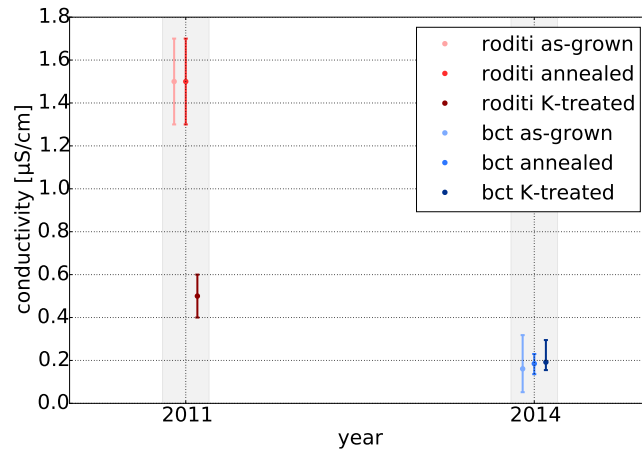


Figure 6.19 – Comparison of ionic conductivities in different KTP substrates for as-grown, annealed and potassium treated wafer.

The low conductivity of Rb-doped material predicts the possibility of poling larger sample sizes. But the conductivity itself is only one parameter which has to be considered for the periodic poling. Another key parameter is the coercive field strength. We will discuss this in the next section.

6.3.1.3 Coercive Field Strength Characteristics

The periodic poling of rubidium exchange waveguides is a challenging task. Before we start poling of mixed materials, we characterised the poling behaviour of the KTA, KTP, RKTP and RTP materials itself. The KTA material exhibits such a high conductivity, that even very small areas of 2 mm^2 reach the current limit of the amplifier before the coercive field strength is reached. For that reason, it was not possible to pole KTA samples in our setup.

The substrate we are using for our sample fabrication is pure KTP, so we inverted the spontaneous polarisation in the material on a larger area. We used the setup explained in section 6.2.2.2 and 6.2.2.3. The electric field has to be higher than the coercive field strength. For KTP we increased the voltage to 3 kV, which corresponds to an electric field strength of $3 \frac{\text{kV}}{\text{mm}}$ (compare figure 6.20 blue line). This field strength is sufficient to visualise the displacement current over the ionic current. We determined the coercive field strength at the point of the highest displacement current (compare to blue bar in figure 6.20) to $E_{C\text{-KTP}} = 2.2 \frac{\text{kV}}{\text{mm}}$.

In case, we would like to periodically pole the Rb-exchanged waveguides, we need the coercive

field strength of the doped material as well. To measure the coercive field strength, we are using the same procedure as for KTP. For this, we used doped bulk material. We measured values of $E_{C-RKTP} = 4.2 \frac{\text{kV}}{\text{mm}}$ for RKTP. For pure RTP, we had only tiny pieces available, such that it was not possible to measure the coercive field strength in our experiments. Instead, we are using values from literature of $E_{C-RTP} = 6.0 \frac{\text{kV}}{\text{mm}}$ taken from [58].

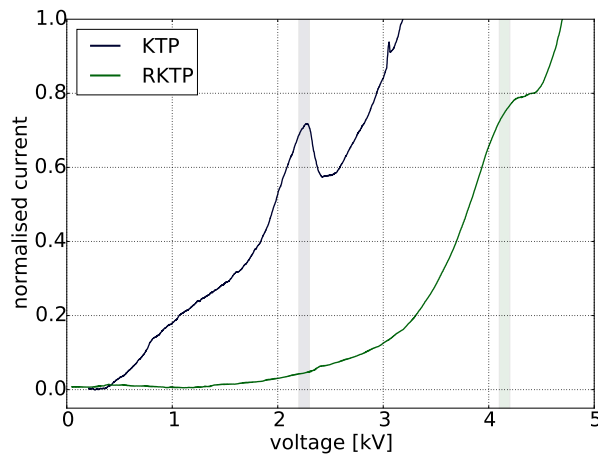


Figure 6.20 – Visualisation of the displacement current during the poling process for KTP and RKTP material.

We have to compare the ionic conductivity at the coercive field strength, which varies between the different materials. The conductivity at the KTP coercive field strength is $\sigma_{KTP-E_C} = 58 \frac{\mu\text{S}}{\text{cm}}$, for RKTP it is $\sigma_{RKTP-E_C} = 36 \frac{\mu\text{S}}{\text{cm}}$. It has to be noted, the measurement of the coercive field strength is a challenging task. The electric field has to be higher than the coercive field strength to visualize the domain inversion. If the field strength is set to too large values, arcs appear and cover up the inversion current or lead to a total damage of the sample. Furthermore, at high field strengths, gray tracks arise, which will be discussed in section 6.3.1.4. If the field strength is too low, the discrimination between ionic current and displacement current is difficult. It is not possible to increase the field strength stepwise, because of a change in the coercive field between as-grown samples and already poled ones.

For all materials, we observe a reduction in the coercive field strength. In KTP, the coercive field strength for as-grown samples is $E_{C-KTP \text{ as-grown}} = 2.1 \frac{\text{kV}}{\text{mm}}$ (compare figure 6.21a) puls 1), while for already poled ones is $E_{C-KTP \text{ poled}} = 1.7 \frac{\text{kV}}{\text{mm}}$ (compare figure 6.21a) puls 2). Such a reduction of the coercive field, depending on the number of repetitions of poling has been mentioned by Jiang *et al.* [78] and Canalias *et al.*[74]. Also in other materials, a reduction can be seen such as in KNbO_3 [139] and LiNbO_3 [140].

During electric field poling, the vacancies and K-ions may redistribute which can lead to a potassium ion concentration gradient. We are using a potassium chloride solution as an electrolyte. In combination with the high electric field, ions can be injected from the liquid solution as well as dilute potassium ions in the crystal. Created space charges can be trapped in the crystal and

modify the internal field and the steady state of K-ion distribution inside the crystal. A subsequent poling can readjust these modifications [74].

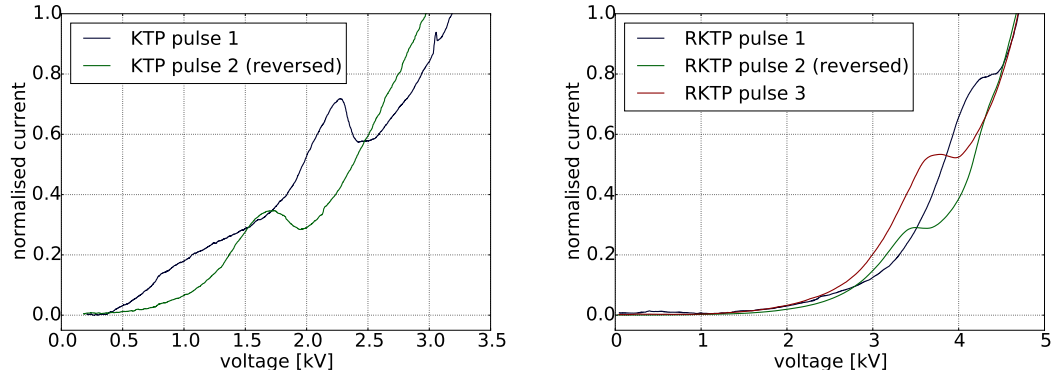


Figure 6.21 – Coercive field strength of KTP and RKTP bulk crystals for different number of pulses.

In RKTP, the coercive field strength for further pulses is reduced from $E_{C-RKTP \text{ as-grown}} = 4.2 \frac{\text{kV}}{\text{mm}}$ to $E_{C-RKTP \text{ poled}} = 3.6 \frac{\text{kV}}{\text{mm}}$ (compare figure 6.21b)). For the second pulse, we see two peaks, one big peak for the reduced coercive field strength. This could be the area which was already inverted in the first pulse. But there is also a second, even smaller peak, at the original coercive field strength. We interpret this peak as an area which had the wrong sign of the spontaneous polarisation. During crystal growth, it is difficult to grow KTP single crystals with a spontaneous polarisation in the same direction. Small areas show the wrong sign. These are the areas we invert in the second pulse for the first time and therefore, it shows the origin coercive field strength.

6.3.1.4 Gray Tracking Characteristics

During investigation of the coercive field strength, we observed an electric field induced gray tracking in the KTP crystals. The origin of gray tracks has been discussed in section 5.6.1. An electric field above $3 \frac{\text{kV}}{\text{mm}}$ introduces gray tracks starting from one side and growing deep into the crystal to the opposite electrode. The gray tracks look like needles that grow into the crystal (compare figure 6.22a).

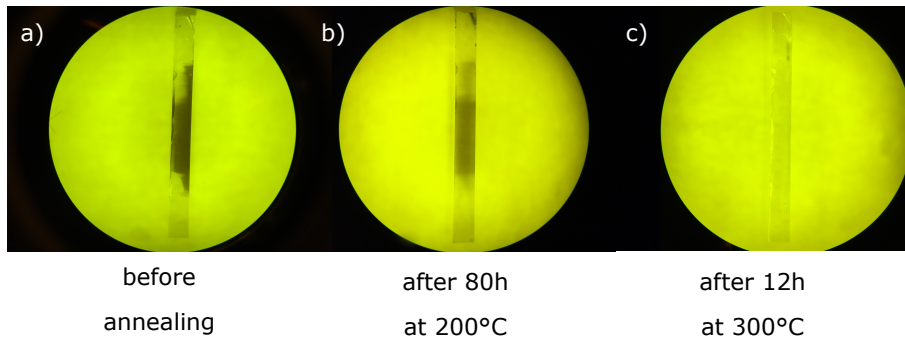


Figure 6.22 – Microscope images of gray tracked KTP samples for different annealing steps.

In this sample, we measured the ionic conductivity similar to the method described in chapter 6.3.1.2. In Figure 6.23a) the local ionic conductivity is shown. In gray track areas, the ionic conductivity is clearly reduced. The schematic sketch on the right hand side indicates the gray tracked area on the KTP sample. The horizontal black lines show the points on which we measured the conductivity. Figure 6.23b) shows an as-grown sample without gray tracking on which the conductivity is constant over the whole sample.

We interpret the reduced ionic conductivity either by a change of activation energy induced by a change of the crystallographic bonding length change (compare to the description in section 5.6.1). Alternatively, the created oxygen ions, which move along the crystal c-axis to the surface block the one dimensional channels and act like Rb-doping which reduces the ionic conductivity as well (compare to section 6.3.1.2).

After an annealing, the ionic conductivity increases again to the initial values (see figure 6.24). The appearance of gray tracks has to be prevented during the sample fabrication. In the next section, we discuss two different sequences to fabricate periodically poled waveguides in KTP.

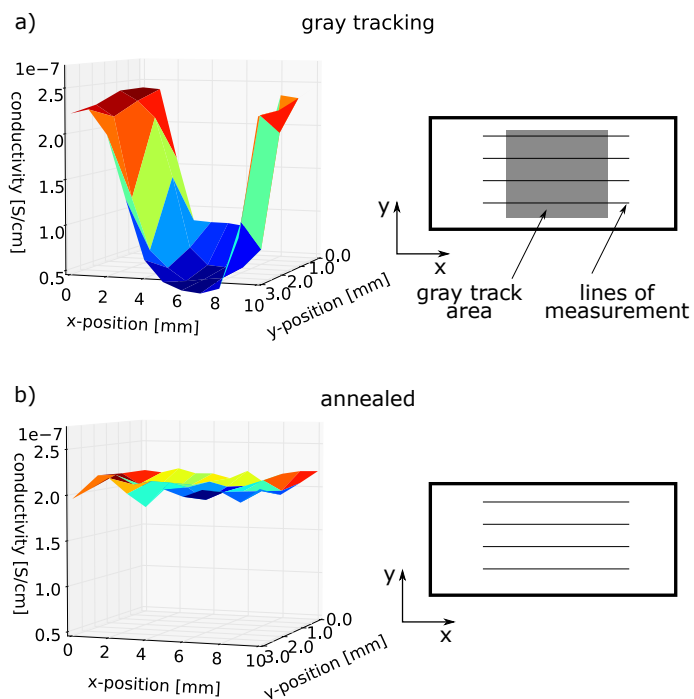


Figure 6.23 – Comparison of the ionic conductivity between gray tracked and as-grown/annealed samples.

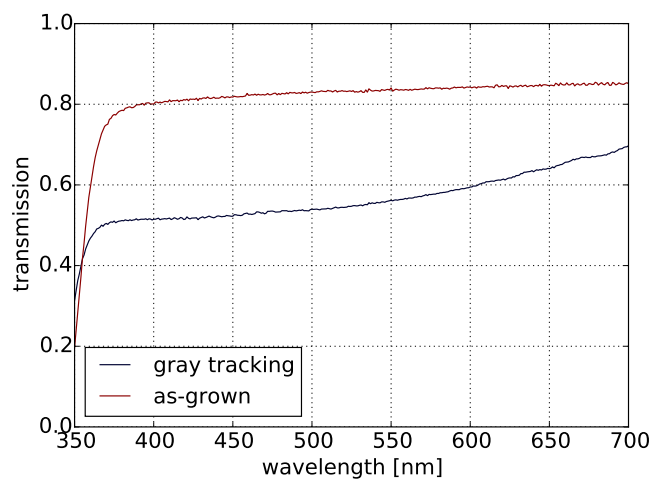


Figure 6.24 – Comparison of the optical transmission between gray tracked and as-grown samples.

6.3.2 Sequence of Sample Fabrication

Until this point, we independently discussed how to fabricate waveguides and how to make the periodic poling. In the next section, we explain the fabrication of periodically poled waveguides in KTP. The material gives us the possibility either to fabricate the waveguides in periodically poled bulk crystals or to pole the rubidium exchanged waveguides (see figure 6.25). In the following sections we show the results of the two sequences and discuss the advantages and challenges of each method.

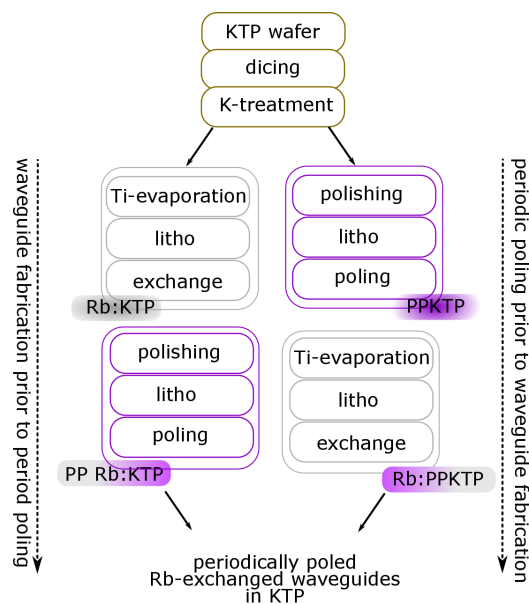


Figure 6.25 – Overview of the two examined fabrication sequences of periodically poled waveguides in KTP.

6.3.3 Poling after Waveguide Fabrication

At first, we will discuss the processes involving the fabrication of exchanged waveguides and a subsequent poling of such structures. This processing is very similar to the standard, well-established fabrication method of Ti in-diffused LN waveguides. In this case, the rubidium exchange is done in homogeneous KTP material. In a subsequent step, we invert the spontaneous polarisation in the exchanged material. The challenge is the poling of the inhomogeneous material, which is now a composition of pure KTP and Rb-doped KTP with different properties as discussed in section 6.3.1. In the following section, we explain the fabrication of such waveguide poling and discuss the results.

6.3.3.1 Fabrication

We start with commercially available KTP wafer (Bright Crystals Technology, Inc.) with a typical dimension of $24 \times 20 \times 1 \text{ mm}^3$ (in a-b-c direction). Due to the high costs of the material, we are not using a full wafer technology, instead we cut the wafer into smaller pieces¹ of $10 \times 6 \text{ mm}^2$. We choose for the fabrication the +c-face of the material. During our experiments, we found out that the poling in waveguides on -c-face is very difficult or even not possible.

Every time the sample surface needs to be cleaned, e.g. before photoresist deposition, after Rb-exchange etc., we clean the sample with a cleaning procedure composed of 4 steps. Each step consists in immersing the sample in different chemical (solutions) for 10 min at $40 \text{ }^\circ\text{C}$ in an ultrasonic bath. The cleaning agents are, in order, acetone (to softening residual photo resist), isopropanol (to dissolve the photo resist), water (to clean the surface) and ammonia solution (12.5% ammonia and 87.5% water, to remove organic residuals).

After the cleaning procedure, we do the potassium treatment to homogenise and reduce, if possible, the ionic conductivity. This is done in all wafers, independently of the initial ionic conductivity and homogeneity (details can be found in section 6.2.3.1). We do an additional cleaning procedure to remove the remaining KNO_3 from the surface.

In the next step, we produce the Ti exchange mask as explained in section 6.2.4.1. The backside is protected with a Ti cover layer to protect this side and prevent a planar Rb-exchange. We do the rubidium exchange as explained in section 6.2.3.3 to achieve Rb-exchanged channel waveguides (see figure 6.26).

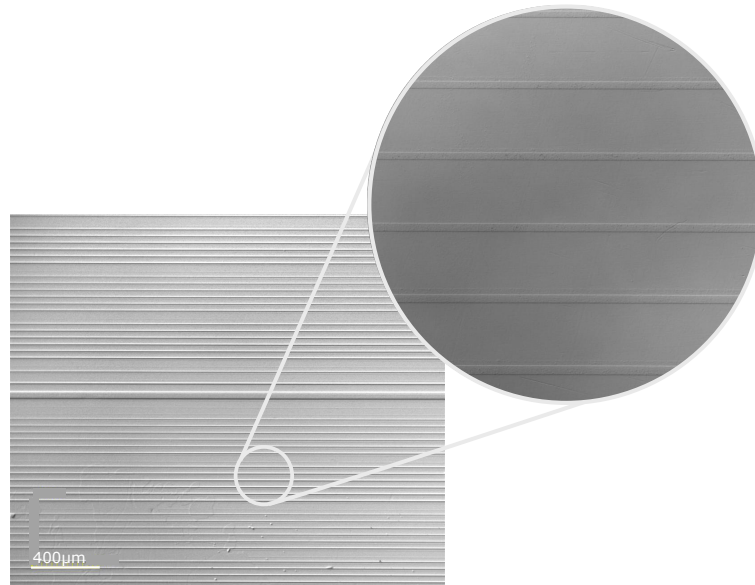


Figure 6.26 – Confocal laser scanning microscope image of a rubidium exchanged surface of KTP.

¹The length in a-direction can vary, depending on the sample and the absolute wafer size

Due to the different poling properties in pure KTP and rubidium doped KTP, we have to do the optical monitoring (see section 6.1.1.2) directly in the waveguide. To enable this, the sample end facet has to be polished (compare to section 6.2.4.2) after an additional cleaning process. The light is coupled with an 8 mm lens into the waveguide. The fabrication of the electrode structure is similar as explained in section 6.2.2.4. Since we are using the optical monitoring in the waveguide, we do not deposit a metal layer (like Au/Pd) because of the absorption of the laser light inside the waveguide. We use only electrolyte for the electrical contact and the photo resist as the insulator. We apply several high voltage pulses, between 300 V and 3 kV, depending on the waveguide and the linked poling properties of the different waveguides. We discuss the results in the following section.

6.3.3.2 Results

First of all, we observe a huge absorption of the transmitted light by the photo resist. This makes it difficult to analyse the poling progress. Nevertheless, it is possible to characterise the poling in the waveguide by usage of the optical monitoring technique. It is necessary to compensate for the initial offset of the phase retardation by adding an additional quarter-wave plate before the linear polariser (see figure 6.28). We optimise the quarter-wave plate and the linear polariser to achieve the maximum contrast in the transmitted light. It is difficult to analyse and compare the optical monitoring at the poling pulse because of different voltages and therefore different rising slopes of the voltage, the rising slope is set to 1 ms, independently of the amplitude. We improved the monitoring technique by adding two additional pulses, one before and one after the poling pulse (compare to figure 6.27). Both have a length of 20 ms and an amplitude of 0.5 kV.

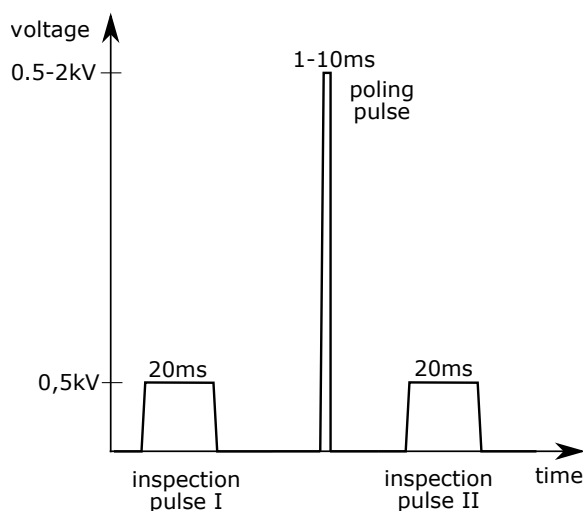


Figure 6.27 – High voltage pulses used for waveguide poling and optical monitoring in the waveguides.

We observe two effects in the optical signal. First, the oscillations do not stop after the plateau is reached (compare to figure 6.29a)). This can be a thermal effect, which influences the ionic conductivity and the electric field strength distributions in the doped and undoped areas. The second observation is the increased number of oscillations in the waveguide, which is in contrast to the expected phase retardation for that specific field strength.

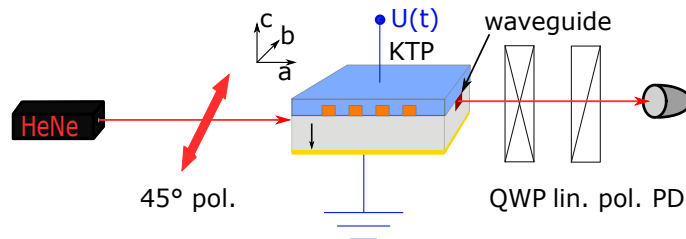


Figure 6.28 – Optical monitoring setup for in-situ determination of the poling process in the waveguide.

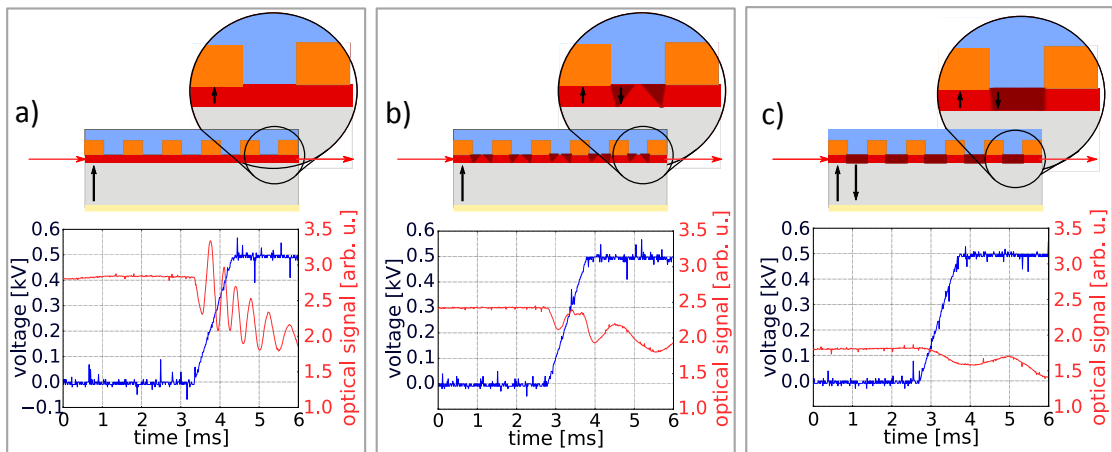


Figure 6.29 – Optical monitoring in waveguides. Figure a) shows the beginning of the poling process where no domain inversion is observable (see inset). In figure b) the waveguide is partially poled (see inset), the number of oscillations is decreased. In figure c) the waveguide is poled close to 50%, the oscillations are mostly vanished. At this point, the poling process has to be stopped.

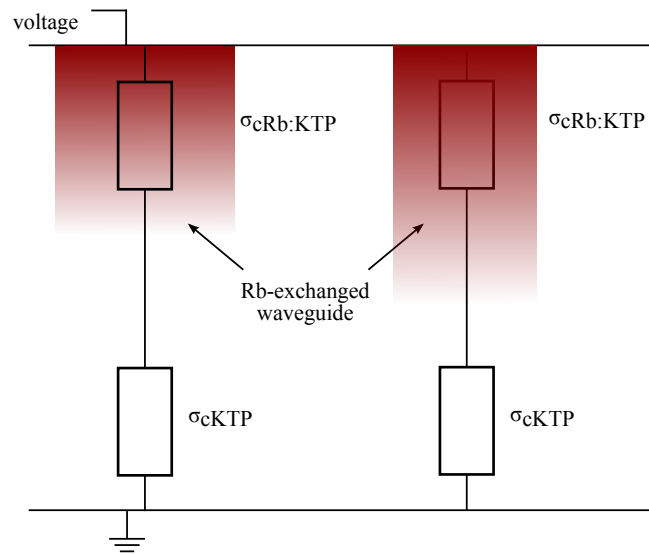


Figure 6.30 – Electrical circuit for Rb-doped waveguides in undoped material. Wider waveguides show a shallower exchange and therefore a decreased resistance.

We explain this by the ionic conductivities, the field strength varies between doped and undoped areas (compare to figure 6.30). Since the ionic conductivity is orders of magnitude lower in Rb-doped KTP (compare section 6.3.1.2), the electric field is much higher in the doped area. This effect must be larger than the increased coercive field strength (compare 6.3.1.3), because only in the waveguide the spontaneous polarisation is inverted. Figure 6.31 shows a selectively etched surface of a periodically poles waveguide.

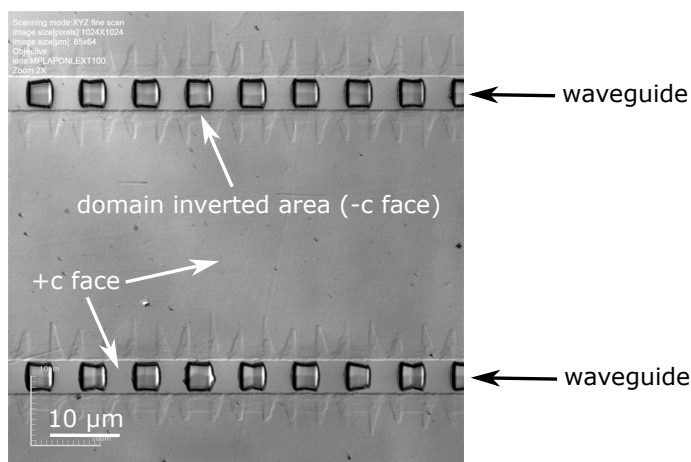


Figure 6.31 – Selectively etched surface of a periodically poled waveguide. The domains are only in the waveguide reversed.

Beside the waveguide the coercive field, which is necessary to invert the spontaneous polarisation, is not reached. If we have a closer look on a larger area (see figure 6.32) on this sample, we see a large variation of the poling behaviour for different waveguides. The sample was prepared according to the mask shown in figure 6.13. From top to down, we see one group of waveguides with different waveguide widths. The upper one has a width of $1.5\ \mu\text{m}$, the lowest has a width of $4.5\ \mu\text{m}$. A clear trend is evident: smaller waveguides are underpoled or not poled at all, while wider waveguides are overpoled or completely reversed poled.

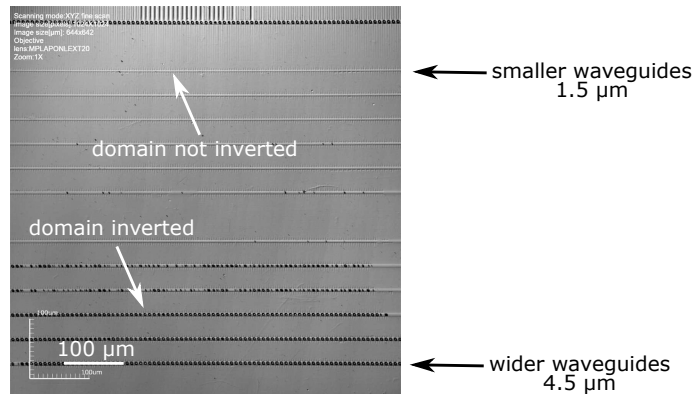


Figure 6.32 – Selectively etched surface of periodically poled waveguides in KTP. One group of increasing waveguide widths from $1.5\ \mu\text{m}$ to $4.5\ \mu\text{m}$ is depicted. A clear trend of smaller waveguides are underpoled, while wider waveguides are overpoled is evident.

Theoretically, a variation of the waveguide width should not affect waveguides so dramatically, since the overall resistivity in the depth does not vary. This suggests the presence of an unknown mechanism that modifies the poling behaviour depending on the waveguide width. Therefore, we will study the waveguides with EDX.

6.3.3.3 EDX Depth Analysis Depending on Waveguide Widths

To understand the different poling behaviours in different waveguides with different widths, we characterised the exchange depth with an EDX system. Details can be found in [92]. An increased conductivity of the surface prevents a charging effect in the electron beam microscope, therefore we coated the polished end facet of a sample with a 10 nm layer of silver. Silver has the advantage, that the X-ray peaks are not overlapped with containing elements in the sample. Furthermore, we can see the waveguides in the electron beam microscope. From the top of the waveguide into the depth we measured the rubidium concentration in a line scan.

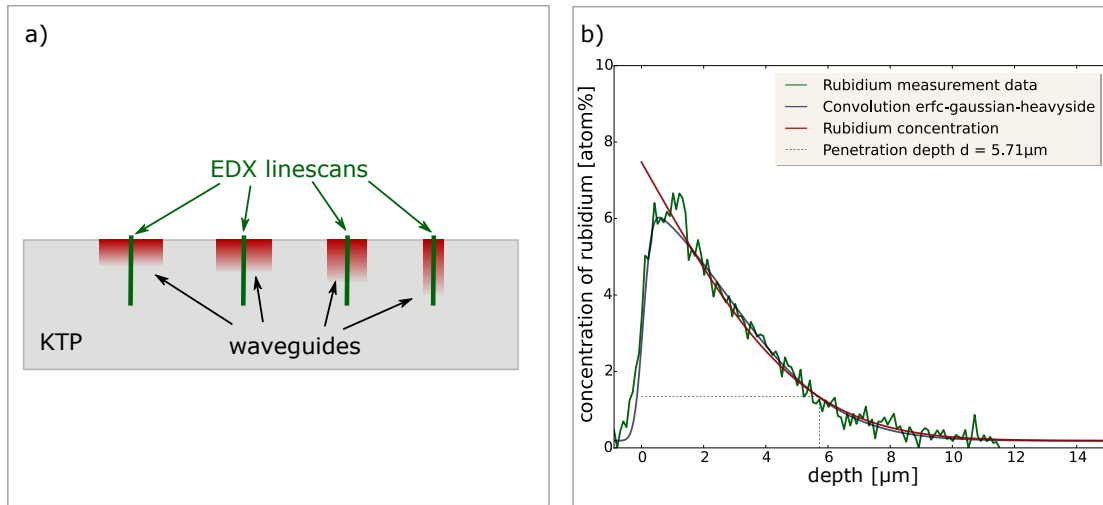


Figure 6.33 – a) Schematic drawing of line scans in KTP waveguides. b) Raw data and calculated exchange profile.

We reconstructed the concentration profile by a convolution of the complementary error function of the exchange profile, with the Gaussian function of the exciting beam and the Heaviside function, which represents the beginning of the sample (see figure 6.33). The exchange depth d is defined assuming the rubidium concentration profile $c_{\text{Rb}}(z) = c_{\text{Rb},0} \cdot [1 - \text{erf}(z/d)]$ [3], where $c_{\text{Rb},0}$ is the concentration at the surface. Surprisingly, the results of the measurement are not in agreement with the one dimensional exchange model. Instead of a constant waveguide depth, we found that narrower waveguides exhibit much deeper exchange profiles (compare to figure 6.34).

This can explain the different poling behaviours for different waveguide widths. For a set voltage across the sample, the voltage drop across the high-resistive Rb:KTP is lower for deeper waveguides (compare to figure 6.30). Therefore, different waveguides will see different poling field strengths, possibly even below the coercive field strength. Therefore, poling Rb:KTP waveguides yields very inhomogeneous results, since in the same sample it is possible to have both unpoled and very overpoled structures, depending on their width and poling voltages.

The domain inversion in the waveguides is reinforced by a larger voltage drop, such that beside the waveguide no poling is observed. Therefore, we expect the poling will stop below the Rb-exchanged region due to a reduced voltage drop. The calculation of the electric field is not trivial, because the voltage drop depends on the concentration and the ionic conductivity which changes also with the concentration. This means that for different samples, the poling behaviour is different due to the variation in the ionic conductivity. To characterise the poling behaviour in the depth of the material we used a confocal Raman microscope.

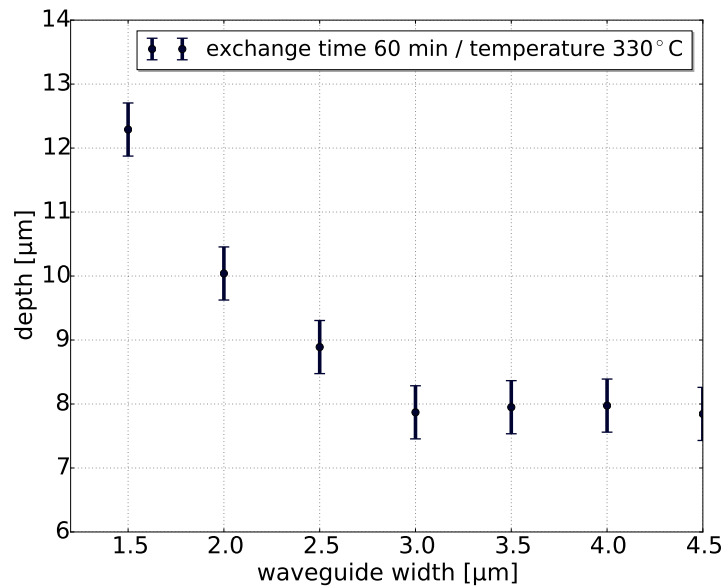


Figure 6.34 – Measured exchange depth for different waveguide widths. The EDX analysis reveals a exchange depth dependence on the waveguide width.

6.3.3.4 Raman Analysis of Domain Inversion in Waveguides

In cooperation with the group of Prof. Zrenner, we had the possibility to investigate the samples by confocal micro Raman spectroscopy. The measurements were performed by Michael Rüsing. The micro Raman spectroscopy allows a non-destructive analysis of the domain inversion in a three dimensional manner [1]. Figure 6.35a) shows the x-y plane of a periodically poled waveguide [85]. This image is comparable to a selectively etched surface image like figure 6.31. It is possible to see in figure 6.35a) the Rb-exchanged region in the horizontal direction in green due to a contrast between KTP and Rb-doped KTP. Also here, only the waveguide itself is poled, the inverted regions can be seen in red.

The analysis, which makes confocal Raman microscopy such a powerful tool, is the domain characterisation in the depth of the material. Figure 6.35b) shows the poling in the depth of the material in the x-z plane (compare to the black line in figure 6.35a)). The domain inversion stops in a depth of 15 μm . This is also observable in figure 6.35c), which shows a cross section of the waveguide. Beside and underneath the waveguide no domain inversion can be measured. The domain inversion is limited to the Rb-exchanged region, which is a huge drawback of this method.

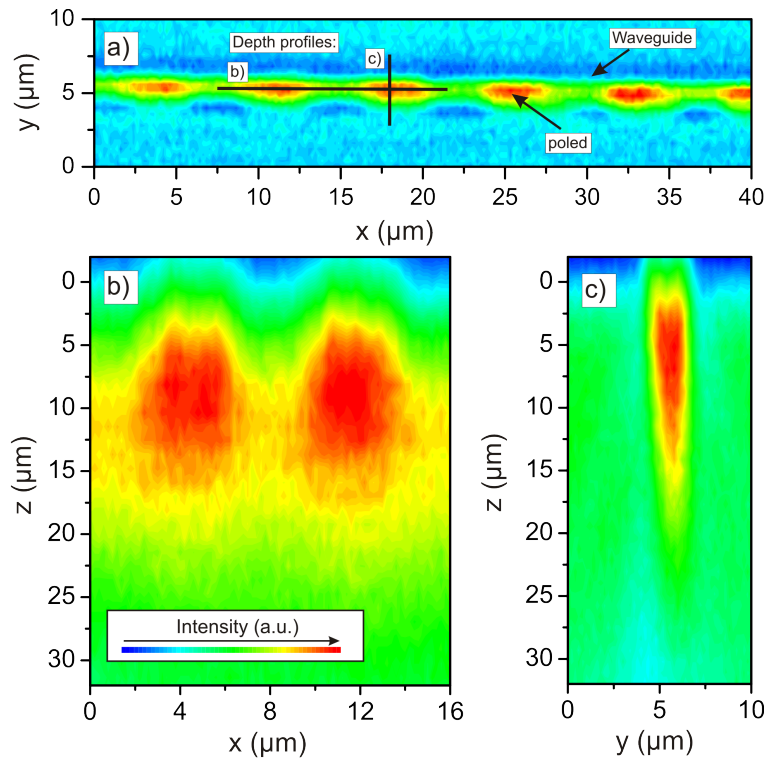


Figure 6.35 – Confocal Raman images of a periodically poled 1.5 μm wide Rb-exchanged waveguide, which was poled after waveguide fabrication. Figure a) shows the top view of a waveguide in the a-b-plane. Only in Rb-exchanged areas a domain inversion is observable. Figures b) and c) show domains in the depth direction of the crystal. In both directions, the domain inverted area is restricted to the Rb-exchanges region. [85]

The shallow domain inversion probably influences the domain stability. High optical power or high temperature can lead to a domain erasing/ back flipping of the domains. Domain stability problems can be a major limiting factor of this method and should be investigated in detail in the future. Because of the previously mentioned challenges and limitations, this method is not well suited for the fabrication of periodically poled waveguide structures in KTP.

6.3.4 Poling prior to Waveguide Fabrication

The other sequence is the fabrication of waveguides in periodically poled substrates to achieve periodically poled waveguides in KTP. One would expect that the poling could be improved because the poor domain growth seen in the previous processing should be avoided. We characterised this method with respect of waveguide homogeneity, poling results and domain behaviour after rubidium exchange.

6.3.4.1 Fabrication

We start by cutting the commercial wafer into smaller piece. In this case, we fabricate the poling and the waveguides on -c-face of the wafer, due to the higher nucleation rate. Like before in chapter 6.3.3, we diced, cleaned and did the K-treatment. Since we do the poling first, we polish the end facet of the samples to improve the contrast in the optical monitoring. In the next step, we make a periodic photo resist pattern comparable to section 6.2.2.1. For an increased electrical contact and to improve the resistivity against the electrolyte, we sputter a Au/Pd layer on both sides of the sample. This can lead to a more homogeneous poling result. In this case, no waveguides are present in the sample, the laser beam for the optical monitoring is transmitted deeper through the bulk crystal and is therefore not affected by the metal layer. To improve the duty cycle homogeneity at the surface, the beam is set closer on the -c-face (see figure 6.36).

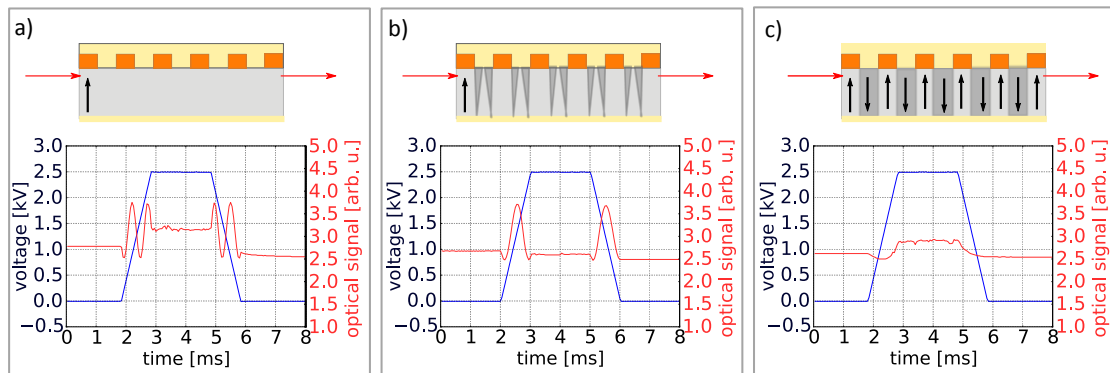


Figure 6.36 – Optical monitoring in bulk KTP. Figure a) shows the beginning of the poling process where no domain inversion is observable. In figure b) the sample is partially poled, the number of oscillations is decreased. In figure c) the sample is poled close to 50%, the oscillations are mostly vanished. At this point, the poling process has to be stopped.

For the domain inversion, we choose field strengths of $2.5 \frac{\text{kV}}{\text{mm}}$, which is significantly higher than the coercive field strength. This allows us to make use of the large anisotropy in the domain growth. The domains grow fast in the c-direction, but not in b-, and even more important, in the a-direction (see figure 6.37). With this, the potential of making short poling periods can be achieved.

After an additional cleaning procedure, in which we also remove the metal layer and the photo resist, we fabricate the exchange mask for waveguide fabrication. We start with the deposition of 100 nm titanium on the former -c-face. The mask and the exchange are done as described in section 6.2.3.2 and 6.2.3.3. The back side is protected by an additional titanium layer. We do the exchange in the periodically poled material. In the next section, we discuss the results of such periodically poled waveguides.

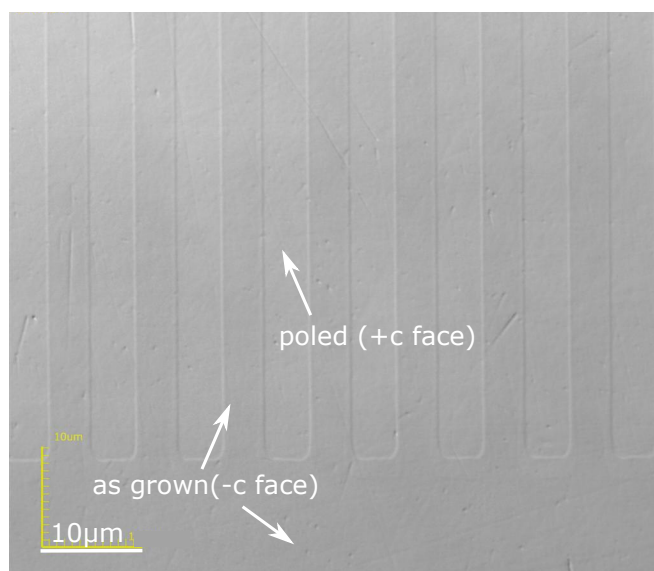


Figure 6.37 – Selectively etches surface of a periodically poled KTP sample.

6.3.4.2 Results

The homogeneity of the periodically poled KTP is much better than in the case of waveguide poling. Figure 6.38 shows a selectively etched rubidium exchanged waveguide in periodically poled KTP. A selective etching created a surface pattern of roughly 10 nm height difference, which is sufficient to achieve a clear contrast under the confocal laser scanning microscope. We measured the duty cycle over the whole sample length in steps of 500 μm (see figure 6.8). The sample shows a promising homogeneity which is better than in the case of poling waveguides. The selective etching gives a detailed overview about the poling on the whole surface of the sample in a small amount of time. But we are also interested in the poling and exchange behaviour in the depth of the material. Since we do the rubidium exchange in an inhomogeneous material, we analysed the influence of the alternating crystal face on the exchange process.

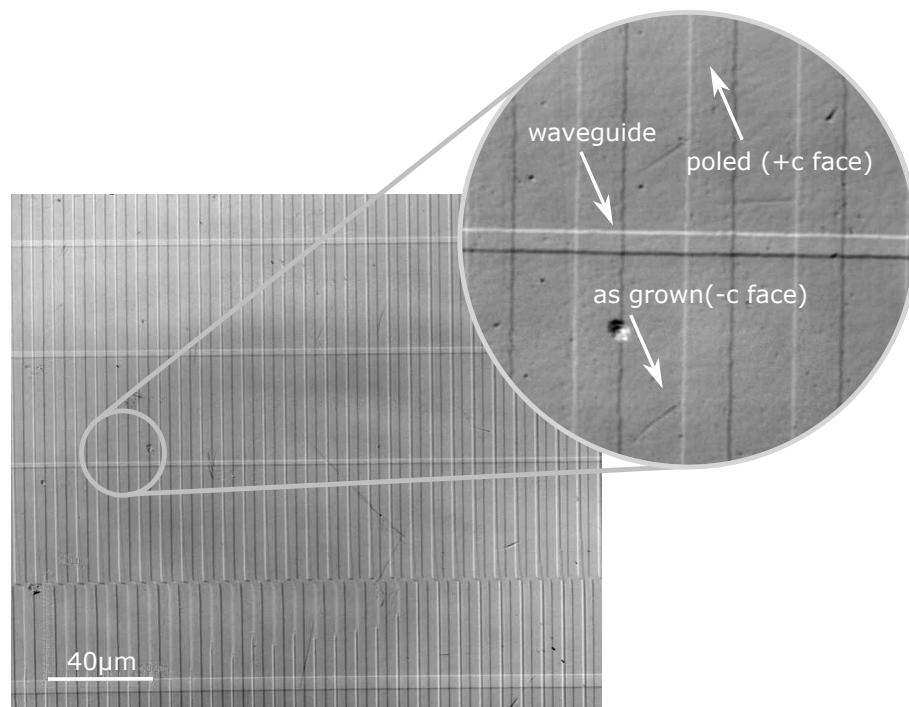


Figure 6.38 – Selectively etched surface of a Rb-exchanged waveguide fabricated in periodically poled KTP substrate.

6.3.4.3 EDX Depth Analysis Depending on Spontaneous Polarisation

We used the EDX analysis technique to check the influence of the alternating domain direction on the exchange process. For these measurements, we re-polished the end facet of a periodically poled sample (period 120 μm) that either the -c or the +c-face ended at the end facet. We measured different waveguide widths and compared both sides. The results can be seen in figure 6.39.

As already discussed in section 6.3.3.3, different waveguide widths show different depths. But independently of the waveguide width, the exchange depth is on the -c-face roughly 2 μm deeper than on +c. This leads to a corrugated waveguide in periodically poled material with alternating +c and -c-faces, and can result in an efficiency drop off nonlinear conversion processes [141]. One solution to overcome this problem is an optimised exchange process. By optimising the melt composition to 88% RbNO_3 , 11% KNO_3 and 1% $\text{Ba}(\text{NO}_3)_2$ and the exchange time and temperature to 43 min at 360 $^\circ\text{C}$ a smooth, corrugation free, single-mode waveguide for 1550 nm can be realised [142]. It has to be noted that an increased temperature leads to an increased domain switching. At 370 $^\circ\text{C}$ as well as at 330 $^\circ\text{C}$, we observed a domain erasure due to the thermal heating during the exchange process. We investigated this behaviour in Raman spectroscopy in more detail in the next section.

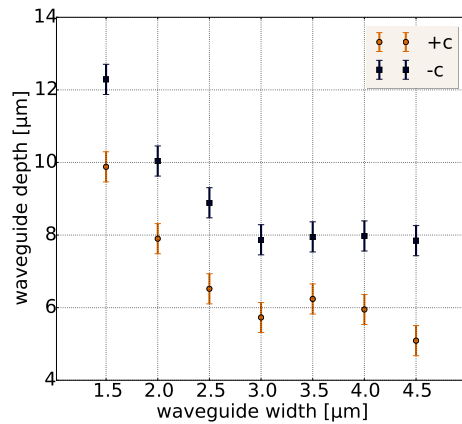


Figure 6.39 – Exchange depth dependence on the waveguide width for the two different crystal orientations +c and -c.

6.3.4.4 Discussion

For the depth analysis of the poling results, we are using the micro Raman microscopy and the SHG microscopy. The micro Raman microscopy gives an insight into the crystal from the top surface without any damage. Since the Raman mode 693 cm^{-1} is sensitive to the domain walls, we can investigate the domains in the depth of the material. Figure 6.40 shows the sketch of a periodically poled KTP sample before the Rb-exchange. In inset a) of figure 6.40, the Raman mode of the a-c-face is analysed. Close to the surface, the domains grow straight into the depth. The typical exchange depth of the waveguides is between $6\text{ }\mu\text{m}$ and $12\text{ }\mu\text{m}$, and therefore much shallower than the investigated depth.

Further, we characterised the poling behaviour into the full depth of the crystal either with Raman and SHG microscopy. These investigations were performed in cooperation with the group of Prof. Zrenner. As before, the Raman analysis was carried out by Michael Rusing, the SHG microscopy characterisation was performed by Peter Mackwitz. Both methods show that at a depth of roughly $500\text{ }\mu\text{m}$, which is half of the thickness of the crystal, a merging of the domain walls. The poling quality varies along the depth of the sample and we measure no poling inversion already in the middle of the sample. Anyway, since the waveguides are fabricated close to the top face, this doesn't affect the quality of poling in the waveguides. We explain this behaviour with the optical monitoring technique. Since we are more interested in the duty cycle and homogeneity at the surface, the laser beam is launched close to the surface through the crystal. The perfect poling result is reached there first.

The modification of the domain structure after the Rb-exchange process can be explained by unstable domains, which had grown only halfway through the sample. In the periodically poled material, we do the Rb-exchange process, the initial state of the domains is shown on the left side in figure 6.41a). After the exchange process, which consists of the heating and cooling steps, as explained in section 6.2.3.3 in table 6.4, and the Rb-exchange for roughly 60 min, the domain walls are distorted. We attribute this modification to a thermal back-switching of the

domains during the exchange process. This is supported by the observation of back-switching in annealed samples without Rb-exchange. Figure 6.41b) shows a selectively etched surface after the Rb-exchange. Figure 6.41c) is taken by SHG microscopy and shows similar results. In the area beside the waveguide, the inverted domains flip back and the duty cycle is not 50:50 any more. Inside the Rb-exchanged area, the duty cycle seems to be the same as before the exchange. We explain this by the more stable domain walls inside the Rb-exchanged areas. We do not observe the domain modification in all samples, we expect more stable domains if the poling is through the whole sample. This has to be investigated in detail in the future.

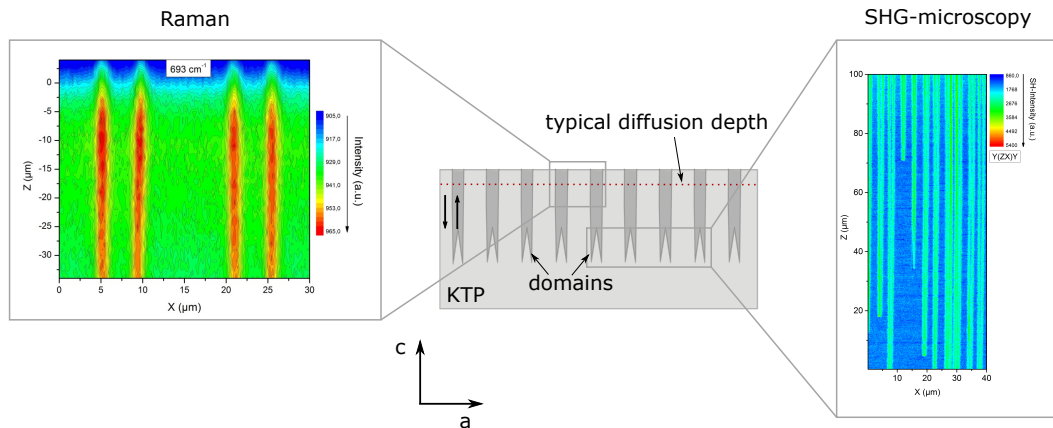


Figure 6.40 – Schematic sketch of a periodically poled KTP sample with a subsequent Rb-exchange. The inset on the left-hand side shows the Raman signal in the depth of the crystal (a-c plane) [85] close to the sample surface. The inset on the right-hand side shows the domains measured by SHG microscopy in the centre part of the sample. The domains inversions stops halfway in the crystal [143].

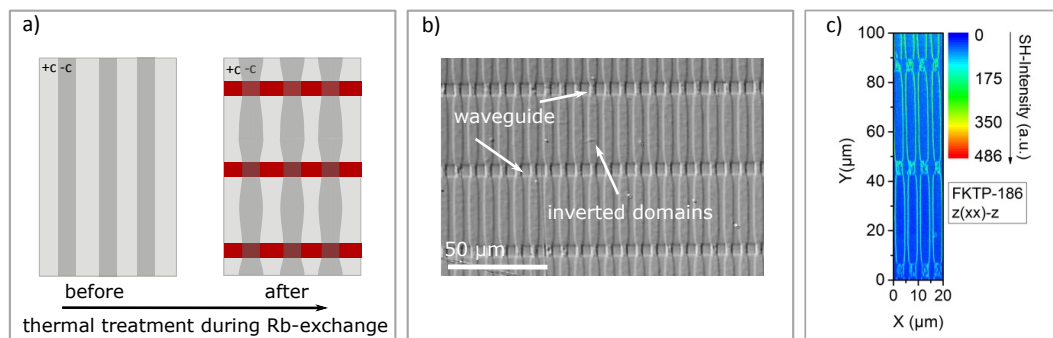


Figure 6.41 – Thermal back-switching during the Rb-exchange can be observed after a selective etching of the domains (sketch in figure a)) and laser scanning microscope image in figure b). The effect is also observable in non-etched samples by second-harmonic microscopy.

6.3.5 Comparison of the Fabrication Results

In conclusion, both sequences of periodically poled waveguide fabrication in KTP can be used. Independent of the fabrication sequence, the previously discussed gray tracks are not expected to appear, since a small doping of Rb inhibits the formation of gray tracks during waveguide poling. If the KTP crystal is poled first, gray tracks can appear, but should vanish during the Rb-exchange process at high temperatures above 300 °C.

The sequence of first doing the Rb-exchange in homogeneous substrate materials and doing the poling afterwards has the advantage of producing more homogeneous waveguide structures. The poling area can be limited only to the waveguide region, which is promising for different lithography techniques, like laser lithography which can be used to fabricate poling structures with an aperiodic poling or e-beam lithography for sub μm poling. Both techniques are sequential writing processes, in which the writing time increases with area which is to be illuminated. The drawback of this method is the poling process in the inhomogeneous substrate, as the coercive field strength varies between pure KTP and the doped material. Furthermore, the exchange depth depends on the waveguide width, limiting the variation range which can be poled simultaneously on the sample. Also the differences in the poling behaviours limiting the poling depth, the poling is not as deep as the waveguide.

The second sequence, which starts with the periodic poling in homogeneous material has the advantage of producing more homogeneous duty cycle. The poling is as deep as the waveguide. The different exchange depths depending on +c and -c-face can be overcome by an optimised melt and exchange process. The appearance of thermal domain erasing on a few samples has to be investigated in detail and is not observed in all samples.

All in all, the fabrication of waveguides in periodically poled material is the most promising technique to fabricate periodically poled waveguides in KTP. For that reason, we are using this kind of technique to realise devices for conversion applications.

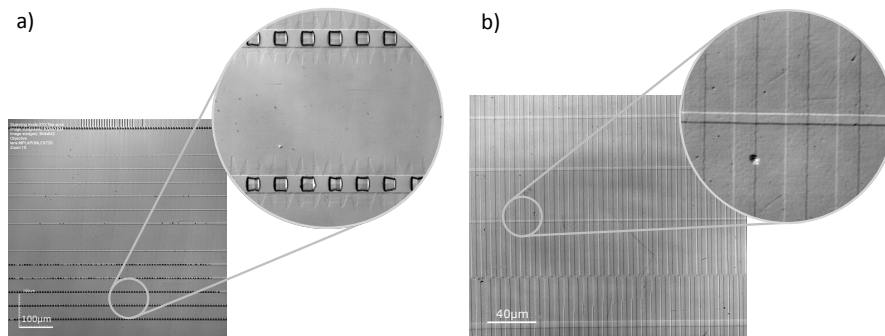


Figure 6.42 – Comparison of the two fabrication sequences to produce Rb:PPKTP devices. a) Results of the fabrication sequence of fabricating first waveguides and perform the poling in a subsequent step. b) Perform first the periodic poling and fabricating waveguides in the periodically poled material.

Summary

In this chapter, we gave an overview about the current technology to fabricate periodically poled waveguides in KTP and explained our solution to overcome challenges and realise such poled waveguide structures. First of all, we had a profound look on the material properties and the poling behaviour to get a better understanding of the exchange and poling dynamics. We investigated two different fabrication sequences and discussed the most promising way to achieve periodically poled waveguides in KTP. The sequence of fabricating waveguides in periodically poled materials is the most promising technique.

Contents

7.1 Optical Dielectric Coatings	85
7.2 Optical Coating Designs	87
7.3 Optical Coating Techniques	89
7.4 Our Coating Facility	92

This chapter focuses on dielectric coatings, which can be used to improve the performance of our sources. First of all, we give a short introduction into dielectric optical coatings, in which we describe the main ideas of coating techniques and show concepts for calculating and designing dielectric coatings. The following sections

describe our coating facility, in which we describe our fabrication technique, already realised coatings and ideas for new types of dielectric coatings and its applications.

7.1 Optical Dielectric Coatings

Optical dielectric coatings play a key role to improve and optimise the performance of our devices. The usage is not limited to KTP samples, we fabricate coatings as well for LN devices and on glass substrates for filters and lenses. Dielectric coatings consist of sub-micron layer-stacks of typically two different dielectric materials with different refractive indices. Usually, one material is used with a high refractive index (H) and another material with a low refractive index (L). An alternating stack of H and L layers with different thickness is deposited on a substrate. The underlying concept is the modification of the refractive properties of the coatings by exploiting the interference of reflections from multiple optical interfaces (see figure 7.1).

Possible applications are highly reflective coatings (HR) on mirrors for resonators e.g. in lasers or in etalons, partially transmissive mirrors for output couplers or for dichroic mirrors, which show a wavelength dependent characteristic. A simple high reflective coating design is a Bragg grating with equal optical layer thickness. Anti reflection coatings (AR), for various kinds of optical filters (e.g. for attenuation of certain wavelength regions) and beam splitters. These AR coatings can be realised by one single coating layer. More advanced applications require more sophisticated mirror designs. Dielectric mirrors normally use several layers, sometimes even more than 100.

The typical kind of dielectric coating consists of discrete layers with discrete alternating refractive indices (figure 7.2a)). However, a novel kind is the gradient-index coatings for rugate filters. Here, the refractive index varies continuously (figure 7.2b) and c)). This can be achieved, by gradually varying the chemical composition by mixing both materials during deposition.

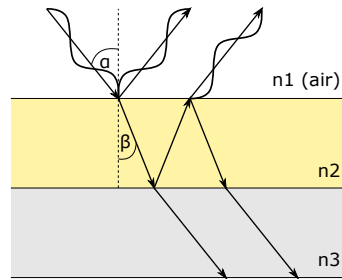


Figure 7.1 – Illustration of the interference effect of quarter-wave layers of a low index material.

The material properties of the dielectric films depends strongly on the used fabrication method and the fabrication parameters such as the substrate temperature, evaporation rate or partial pressures. Compared to ordinary bulk materials of nominally identical stoichiometric composition, thin-film layers often show a reduced density and therefore a reduced refractive index. The changes can be marginal but change the final design dramatically. This has to be taken into account during the design of dielectric coatings. The differences can be substantial, so that for the fabrication on a certain coating machine, it is absolutely essential to obtain the dispersive refractive index for that machine under the used conditions.

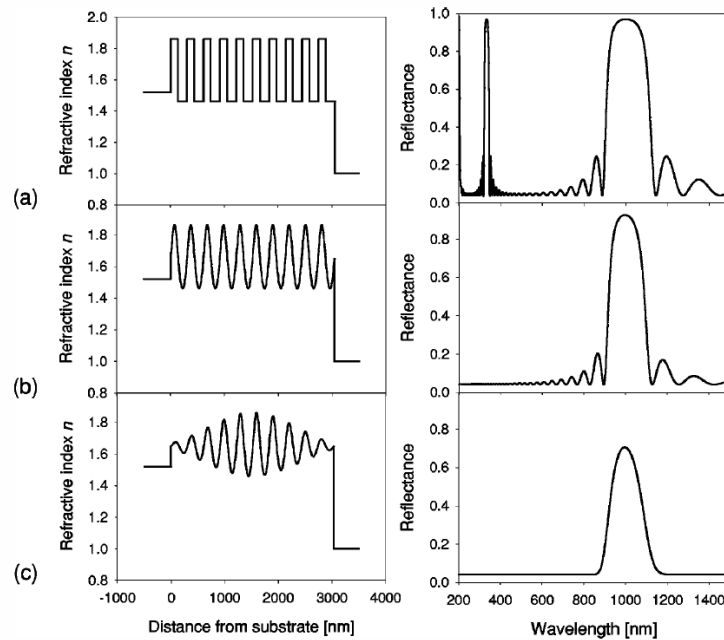


Figure 7.2 – Summary of filter properties: $n(z)$ profiles and $R(\lambda)$ of: a) a multi-layer, quarter-wave stack; b) a rugate filter; and c) a rugate filter with apodisation. Figure from [144]

7.2 Optical Coating Designs

Next, we explain the basics of calculating the optical properties of dielectric coatings. At each interface one part of an incident light wave will be reflected and a second part transmitted (see figure 7.1). The mechanism behind the reflection and transmission of optical light waves is based on optical interference effects. Two propagating beams along a coincident path with matching spatial location of the wave peaks and matching phases combine constructively and create a beam with a larger total amplitude. If the two beams are out of phase, e.g. a phase shift of π , they interfere destructively and the total amplitude decreases or vanishes. This effect is known as constructive and destructive interference, respectively. The performance of an optical coating depends on the number of layers, the thickness of the individual layers and the refractive index contrast between the high and low refractive material.

During an experiment, wavelength and angle of incidence are usually fixed values. The free parameter, which can be used to optimise the performance of an optical coating is the thickness of the different layers. Changes in the layer thickness have an effect on the path length of the light waves, which results in a phase change. The simplest coating one can imagine is a single layer anti reflection coating. Light propagating through a single layer, splits up in a reflected and a transmitted part at each interface (compare to figure 7.1). The phase-shift directly corresponds to a $\frac{\lambda}{2}$ shift of the sinusoidal wave, which can be accomplished by choosing the optical thickness of the layer to be $\frac{\lambda}{4}$. In this case, the phase-shift between the two reflected beams is π , and they cancel out.

Thus, not only the path length influences the optical characteristics, but also the reflection properties at each interface play an important role. The transmission (T) and reflection (R) is defined through Fresnel's equations [49]. For an interface $\frac{n_1}{n_2}$, we find for s-polarised light:

$$R_s = \left(\frac{N_1 \cos \alpha - N_2 \cos \beta}{N_1 \cos \alpha + N_2 \cos \beta} \right)^2 \quad (7.1)$$

$$T_s = \left(\frac{2N_1 \cos \alpha}{N_1 \cos \alpha + N_2 \cos \beta} \right)^2 \quad (7.2)$$

and for p-polarised light:

$$R_p = \left(\frac{N_2 \cos \alpha - N_1 \cos \beta}{N_2 \cos \alpha + N_1 \cos \beta} \right)^2 \quad (7.3)$$

$$T_p = \left(\frac{2N_2 \cos \alpha}{N_2 \cos \alpha + N_1 \cos \beta} \right)^2 \quad (7.4)$$

with N_1 and N_2 as index of refraction, which is in general a complex number and can be decomposed to $N_x = n_x + ik_x$. Here, n_x denotes the classical index of refraction and k_x the extinction coefficient, which is related to absorption of the material. α is the angle of incidence and β is the angle of refraction, which can be calculated by Snell's law. For normal incidence, $\alpha = 0$, and negligible absorption, the terms simplify to

$$R = \left(\frac{n_1 - n_2}{n_1 + n_2} \right)^2. \quad (7.5)$$

and

$$T = \frac{4n_1n_2}{(n_1 + n_2)^2} \quad (7.6)$$

All reflected and all transmitted light waves interfere either constructively or destructively, depending on the optical path difference (OPD). For the reflected parts, the OPD is equal to $2n_2d \cos \beta$, with d as the physical thickness of the layer. For a given wavelength, the interference is constructive if $OPD=m\lambda$ and destructive for $OPD=(m+\frac{1}{2})\lambda, m \in \mathbf{N}$.

The same formulas can be used to calculate all interfaces $\frac{n_i}{n_j}$. So, the total reflectance and transmittance can be calculated from the angle of incidence, refractive indices and physical layer thickness.

As already mentioned, the reflection becomes zero for specific wavelength λ for a $\frac{\lambda}{4}$ -thick layer at normal incidence. This is the easiest way to produce an anti reflection coating. If it is not possible to find a coating material with matching refractive index between coating material and substrate or a broad band coating is required, a multi layer coating can be used. Here, the described process occurs at every interface between the layers. This complicates mathematical calculations and often leaves numerical simulations as a last resort.

For a high reflective coating at wavelength λ , a simple analytical solution exists. The most effective way is a stack of alternating H and L refractive layers with a thickness of $\frac{\lambda}{4}$, also called a quarter-wave stack. For this kind of system, the reflectance increases with the number of layer pairs. Calculations show, that a sequence of about 10 pairs is sufficient to increase the reflectance up to approximately 100%, as presented in figure 7.3. This effect is limited by absorption and scattering losses in the coating.

Consequently, the transmission decreases to nearly 0%. The spectral width of the reflection band depends on the contrast of the refractive indices of the layer materials. A large refractive index ratio results in a broad reflection band. Thus, the quality of the layers and therefore the performance of the coating depends on the fabrication technique, which will be discussed in the next section.

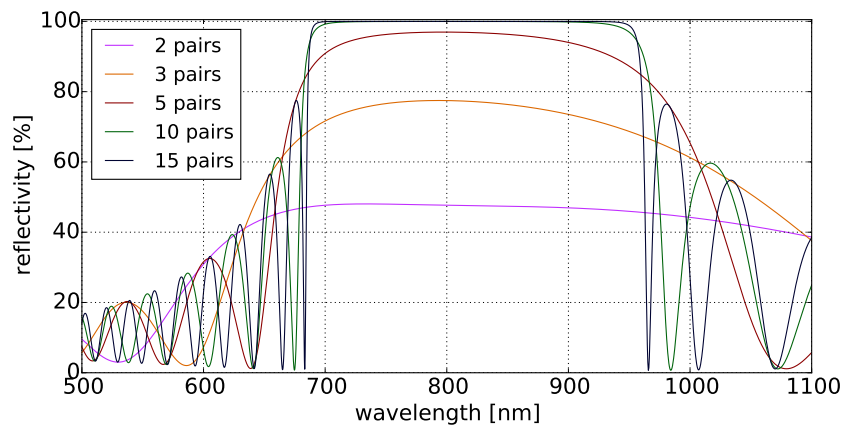


Figure 7.3 – Calculated reflectivity of quarter-wave stacks consisting of 2, 3, 5, 10 and 15 layer pairs of $\text{TiO}_2/\text{SiO}_2$.

7.3 Optical Coating Techniques

Various techniques can be used to fabricate dielectric layer coatings. Here, we are focusing on the four most important ones, namely electron beam deposition (EBD), ion-assisted deposition (IAD), ion beam sputtering (IBS) and advanced plasma reactive sputtering (APRS) [145, 146]. In order to choose an appropriate technique, the following aspects have to be taken into consideration.

- the suitability to handle a given coating material
- the precision of the layer thickness values, which can be improved by using an in-situ growth monitoring system
- the optical quality of the deposited layers, which is linked to absorption and scattering losses of the coatings
- the requirement for using high optical powers that could potentially damage the coating
- the uniformity of the layer thickness
- the consistent, reproducible and stable deposition of the materials without variations in the refractive indices
- the required substrate temperature
- the deposition rate, which defines the coating time

The in-situ growth monitoring is crucial for obtaining precisely controlled layer thickness. An optical in-situ monitoring allows for the determination of the optical transmission properties during the growth process. Thus, by applying appropriate system and process control, the layer thickness can be adapted to the current measured optical data, resulting in an enhancement of the coating performance. One challenge here is the fact that the temperature during deposition and the later operation might differ significantly, which could be compensated by knowledge of the progression of the temperature-dependent refractive index. However, these data are often not available.

Materials with a high refractive index contrast are the favourable choice for high reflective and large refractive bandwidth coatings. However, the chosen materials should also allow the fabrication of high optical quality films and provide a high stability concerning environmental conditions, i.e. variations of humidity might lead to a shift of the coating performance.

For the fabrication of dielectric mirrors, usually one of the following techniques is used [146] (compare to figure 7.4).

Electron Beam Deposition

Electron beam deposition is a simple technique, which is based on the evaporation of a material from a crucible by heating up the material with an electron beam. We are using electron deposition as one simple example, which represents several similar methods, like the evaporation by resistive heating of the crucible to evaporate the material. The electron beam can be generated by a hot filament, which is then focused and directed to the crucible by means of a magnetic field. To stop the evaporation, a mechanical shutter closes the path between the crucible and the substrate on a rather short time scale, which facilitates precise control over the deposited layer's thickness. The drawback of this method is the tendency to create porous layers, leading to a reduced density and subsequently to a reduced refractive index. This has a direct influence on the optical properties of the fabricated layer, such that e.g. water absorption in the pores leads to a shift of the target design with respect to all properties, i.e. transmission, phase, GDD etc.

Ion-assisted Deposition

Ion-assisted deposition (IAD) essentially works like the previously described e-beam evaporation. An additional ion beam source, typically using oxygen or argon ions, produces high energetic ions which hit the target substrate. This allows a reordering of the deposited material and leads to denser coating layers, even without heating the substrate, which can be of great importance for ferroelectric materials like LN and KTP. It is a well suited method for oxide coatings, e.g. SiO_2 and TiO_2 , which can produce similar quality coatings as those obtained with sputter deposition techniques.

Ion Beam Sputtering

Ion beam sputtering (IBS) uses an ion beam to sputter a metal or metal oxide. The dispersed material is then collected on a substrate. The advantages of the IBS technique are the well controlled flux and the energy of the ions, which can be controlled and optimised independently and very precisely. This leads to fairly uniform and reproducible, non-porous coatings with very high adhesion and a low surface roughness below 1 Å. However, the deposition rate is very low, and the technique requires expensive equipment and materials.

Advanced Plasma Reactive Sputtering

The advanced plasma reactive sputtering (APRS) is a more sophisticated alternative to IBS. The basic idea is the initial sputtering of thin metal films, which are subsequently oxidised in a separate oxygen plasma region. For this method, separate magnetron sources have to be used for the different coating materials. APRS represents the most practical technique, which combines a high precision and a high density of the coating layers, similar to IBS layer, with a high deposition speed, comparable to evaporation techniques. However, APRS requires very expensive equipment, which leads to a very low benefit cost ratio.

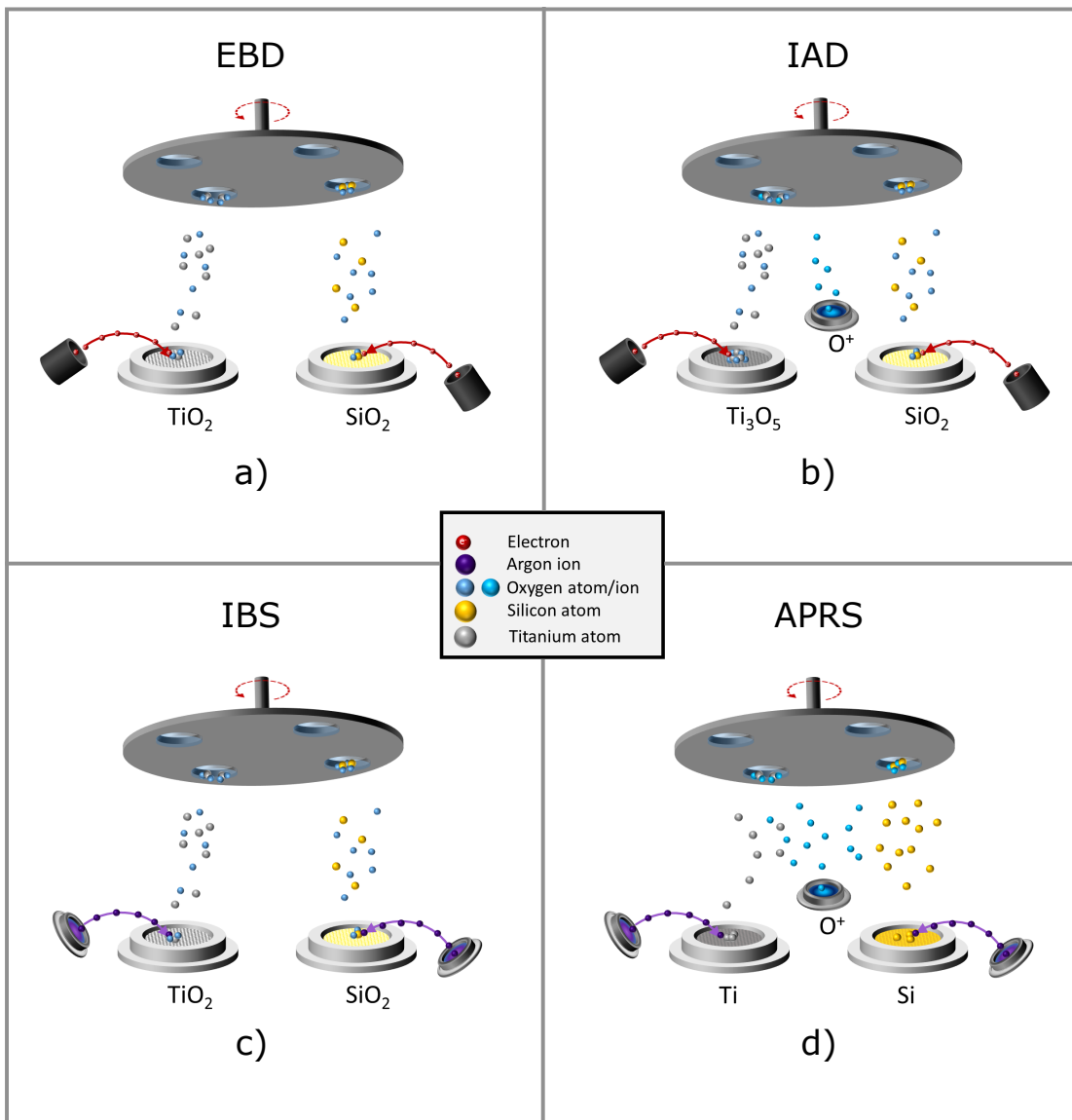


Figure 7.4 – Schematic sketches of various coating techniques. Material from the targets can be dispersed either via electron or ion beams. The process can be enhanced by adding an oxygen ion source. Out of that four techniques can be distinguished, namely a) electron beam deposition (EBD), b) ion-assisted deposition (IAD), c) ion beams sputtering (IBS), d) advanced plasma reactive sputtering (APRS).

7.4 Our Coating Facility

In our coating facility, we are using an ion-assisted deposition system. It represents the best trade-off between flexibility, cost and deposition rate. As explained in the previous section, the coating material is evaporated by an electron beam. In our machine, we use two electron beam evaporators, one for the high refractive material TiO_2 and the other one for the low refractive material SiO_2 , respectively. Both sources can be controlled separately to deposit both materials simultaneously. This allows the mixing of both materials to fabricate coatings with slowly varying refractive index. This technique facilitates the fabrication of so called rugate filter. The deposition process can be stopped and the coating material can be heated up without a deposition by closing a shutter. The deposition rate and the thickness of the already deposited material of each crucible is monitored by a quartz balance. The crucibles of both materials rotate to achieve a stable and homogeneous evaporation.

The low refractive material SiO_2 keeps solid during evaporation. This means that the stability of the evaporation over time is a considerable challenge. On the one hand a plate of SiO_2 can be used. In the beginning of the evaporation process, this is more stable but the geometrical characteristics change over time due to race tracks in the plate. On the other hand granular SiO_2 does not change over time but the deposition rate varies much stronger on a short time scale. However, the second option with granule materials gives the better results in our process. As already mentioned, we are using TiO_2 as high-refractive material, which decays during evaporation. Layer with a higher optical quality can be made by evaporating Ti_3O_5 and fully oxidising the material directly on the substrate. In contrast to SiO_2 , Ti_3O_5 forms a molten pool with a smooth surface which leads to a stable evaporation over time. To optimise the geometric evaporation characteristics, the electron beam position in the crucible can be adjusted.

To improve the quality of the coatings, we are using an oxygen plasma source producing positively charged oxygen ions. The ions are extracted by high voltage in a three grid system. This grid has a curvature to optimise the homogeneity of the oxygen bombardment at the substrate position. Since we are using dielectric materials, ions would lead to a charging effect of the substrate and deflect further ions. Especially for ferroelectric materials, e.g. LN and KTP, this charging effect can lead to damage of the material. For that reason, the oxygen ions have to be neutralised. The common way to achieve this, is thermal heating of a metallic filament. This is a crucial limiting factor, because of the very short life time of a hot filament in an pure oxygen atmosphere. If the filament is broken, the coating process has to be stopped, the vacuum chamber has to be opened and the wire replaced, which leads to a variation in the coating conditions. To overcome this limitation, we are using an electron source producing electrons out of an argon plasma. This filament free technique lowers the risk of having to stop the process.

The homogeneity of the coating layer is directly linked to the distance between the sample position (the sample is fixed on a calotte, see figure 7.5) and crucibles as well as oxygen ion source. For that reason we are using a relatively large chamber of 700 L, which corresponds to a sample-to-target distance of approximately 800 mm. The calotte itself can be rotated, which allows the coating of several samples with identical optical characteristics. Above the calotte is enough space to place samples with a length of more than 10 cm, which is necessary to produce end facet coatings on long samples. Behind the samples a thermal heater stabilises the temperature during the evaporation process. A key feature of high quality coatings is an optical monitor-

ing, which allows the monitoring during the evaporation process. The optical monitoring can be done directly on the substrate, if the substrate allows a measurement in transmission. If this isn't possible, e.g. for end facet coatings on thin KTP and LN samples, the calotte rotation facilitates the monitoring on a test glass situated beside the sample position. Due to the fact that there is no geometrical conversion necessary, the optical monitoring allows for precise monitoring and switching off of the coating process.

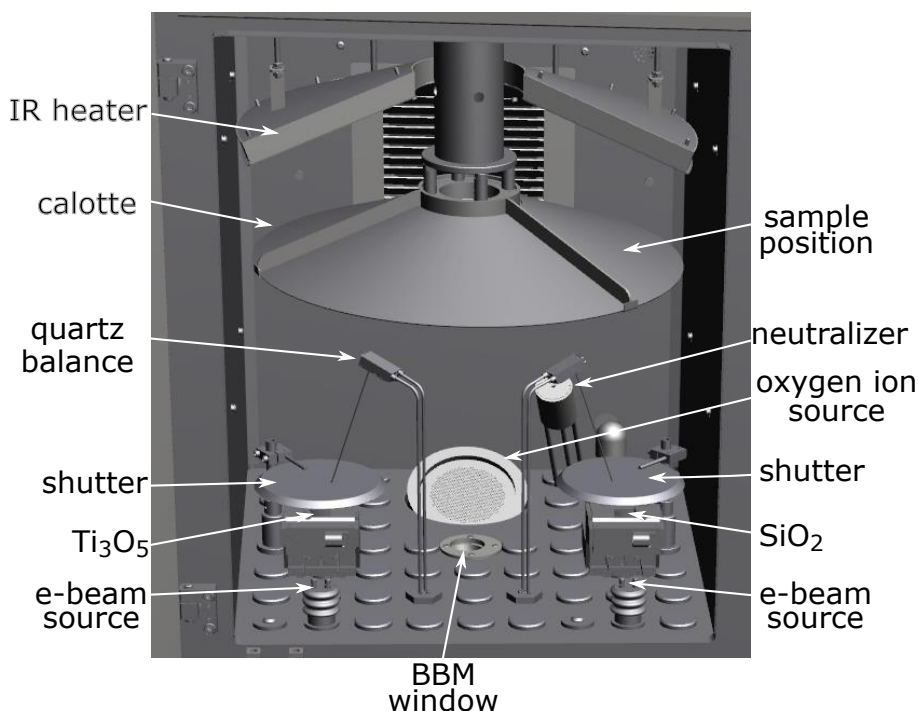


Figure 7.5 – CAD drawing of the IAD coating machine Marquis M700 [147].

7.4.1 Broad Band Monitoring

Optical monitoring is essential for high-precision coatings. Simple systems use only one wavelength to measure the transmission value of a coating during evaporation. A more precise way is an optical broad band monitoring (BBM), which we are using for our coatings. Here, the full spectrum is used to measure the optical characteristics of the coating during evaporation. The operation is based on the determination of the actual layer thickness by measuring changes in transmission through the substrate being coated (see figure 7.6).

A predefined coating design and the number of the actual layer are used as the basis for process-tracing calculations of the layer thickness, the deposition rate and finally, the time until the deposition has to be terminated. As a light source, we are using a halogen lamp, emitting a broad homogeneous spectrum from 400 nm to 1700 nm². At the bottom of the vacuum cham-

²It has to be noted, that plasma light sources show a better performance with respect to intensity, spectral emission and collimation, but hold a high failure rate by interaction with the high energy oxygen ions.

ber, the light is coupled into a fibre and linked to two spectrometers (see figures 7.5 and 7.6). One spectrometer measures the visible wavelength range from 400 nm to 1000 nm and a second one measures the IR spectrum from 1000 nm to 1700 nm.

The measured spectrum is fed into the BBM software to calculate the actual layer thickness and the deposition rate. During the coating process, the calotte rotates. The measurement is triggered by a rotary decoder and for each calotte rotation, three different measurements are performed. The first one is the dark spectrum to get rid of reflections inside the chamber. The second one is a light source spectrum to compensate for spectral variations during the coating process, because the light source is also in the vacuum chamber and might itself get coated with thin layers of SiO_2 and TiO_2 which influence the spectrum. The last spectrum is the actual spectrum through our sample or test glass. The BBM software calculates the layer thickness during the coating process and by using these data the best process end time for each layer.

Small errors, which occur due to deviations in the dispersion data or small errors in the end time calculations, are corrected for to achieve the best performance for each design. The software optimises the following layer to fulfill the targeted design. Beside the error correction, a conversion tool is implemented in the software to calculate the spectrum on a different material, e.g. the spectrum might be measured on a test glass (BK7), but the design is for LiNbO_3 . This is also possible if a coating is designed for fibre coupling (LN - glass) but measured during the coating process against air/vacuum. Additional to the layer thickness, the material dispersion can vary or change during the coating process. This can be compensated and corrected for in-situ, which makes reverse engineering after the coating process redundant. The optical monitoring allows for the fabrication of advanced coatings with excellent performance. Coatings which we have already realised will be discussed in the next section.

BBM system integration

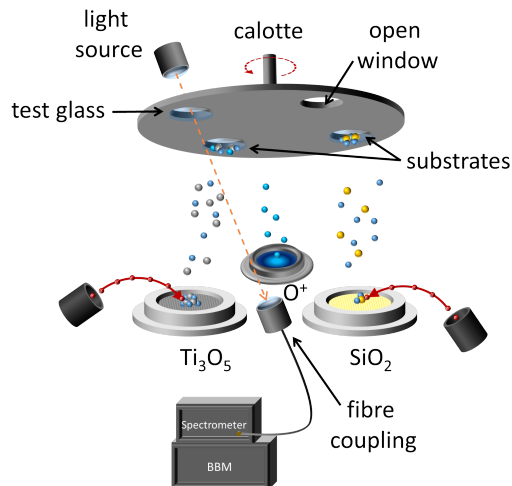


Figure 7.6 – Implementation of the BBM system into the coating machine.

7.4.2 Realised Coatings

In the previous sections we introduced our coating facility. This section is dedicated to coatings that have been realised during the course of this thesis. Depending on the design, the determination of the performance is a challenging task. Due to limitations in our equipment, we can only measure the spectral response of our coatings in transmission. For this, we use a *Cary UV-VIS-IR 5000* spectrometer, which can measure in a wavelength range between 180 nm and 3200 nm, with a maximal accuracy of 0.1 nm. This method gives high precision results for anti reflection coatings. To determine the performance of partial or high reflective coatings, also absorption and scattering effects have to be taken into account. The corresponding coefficients sum up according to

$$1 = T + R + A + S, \quad (7.7)$$

with the transmission T and reflection R . The additional parameters A and S denote the absorption and scattering for the coating, respectively. While we can measure the transmission very precisely, the estimation of reflection is a challenging task due to the unknown values of A and S . In the following, we show several coatings which have been realised so far, starting with anti reflection coatings.

AR Coatings

Anti reflection coatings usually consist only of a few layers. The end facet reflectivity depends on the refractive index of the material and, due to the dispersion, also on the wavelength. The reflectivity can be calculated using equation 7.5, which yields at 800 nm a reflectivity per end facet of about 4% for glass, 14.8% for LN and 8.8% for KTP, respectively. These values are calculated for a transmission from the substrate into air at a wavelength of 800 nm.

As an example for an anti reflection coating, we use a LN end facet coating. The measured transmission as a function of λ through LN is shown in figure 7.7. The blue curve of figure 7.7 shows the transmission through LN without AR coatings. Both end facets contribute to the reflection of 27.5%. If we deposit an AR-coating on one of the end facets, the overall transmission increases. The green line shows the transmission trough one side coated LN, the two anti reflection bands are indicated by the orange bars. The opposite side (or back-side) still leads to a reflection at the end facet. If we correct the reflectivity for back-side reflection (red line in figure 7.7), we determine a transmission of more than 99%. These coatings consist of four layers with an overall thickness of 440 nm.

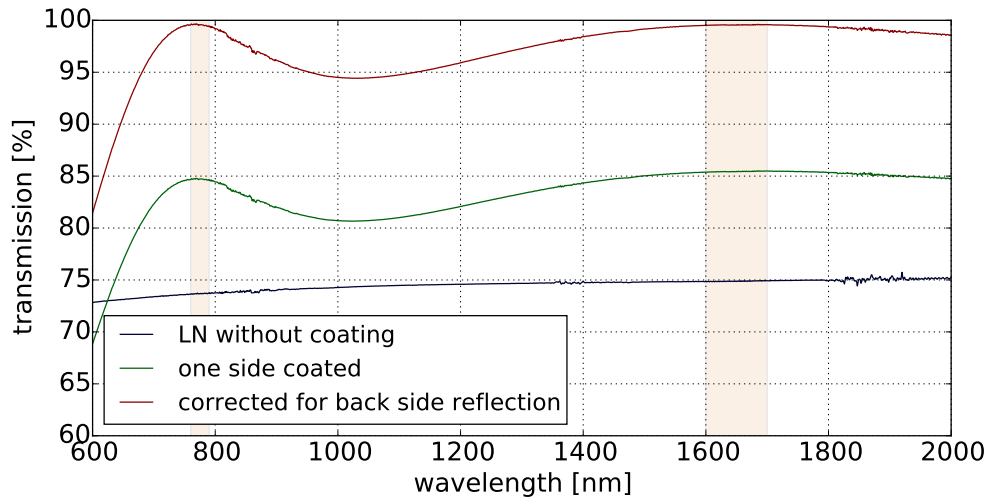


Figure 7.7 – Spectrum of an anti reflection coating for two wavelength regions at 800 nm and 1600 nm (orange bars), deposited on a LN sample. The blue line shows the transmission through an uncoated LN sample. The green and the red curve indicate the transmission through a one side AR coated LN sample and transmission through a sample with one side coated and the other side corrected for Fresnel losses, respectively.

This coating was used for the monolithic integration of a Hong-Ou-Mandel Experiment in a titanium indiffused LN waveguide [7]. We can increase the number of reflection bands by applying more advanced layer stacks. Doing this, we also fabricated coatings for three wavelength regions (AR for 550 nm, 860 nm and 1550 nm) on both sides of a LN sample [42–44]. Furthermore, anti reflection coatings on KTP play an important role to improve the performance of the devices. We deposited a four layer coating with a thickness of 420 nm on both sides of a KTP waveguide chip, which was used for generating entangled quantum states. The residual end facet reflectivity was below the measurement uncertainty of 0.06% and increased the entangled state fidelity from roughly 86% without a coating to a fidelity of 99.9% with both faces coated [31].

HR coatings

High reflective coatings play an important role for mirrors. Especially, dielectric coatings predict a higher reflectivity, and therefore introduce less losses, in comparison to metallic mirrors. For loss sensitive quantum experiments, this can be the bottleneck for a reliable experiment [45]. Due to the fact that most of the light is reflected in the dielectric material, the coating is insensitive to the substrate material, however the flatness of the material is an important parameter. Thus, these HR coatings could also be deposited on glass substrates. We used a BK7 glass substrate with a flatness of $\frac{\lambda}{4}$. The coatings consists of 21 layer and has a thickness of about

5250 nm. Figure 7.8 shows the transmission characteristics. The orange bar indicates the target reflections band. The inset indicates the reflectance with an optimised y-scale. Measurement of the transmission yield values of about 0.02%. In our experiments, a reflectivity of 99.3% was determined. Thus, the effects of absorption and scattering can be estimated to be on the order of 0.68% according to equation 7.7.

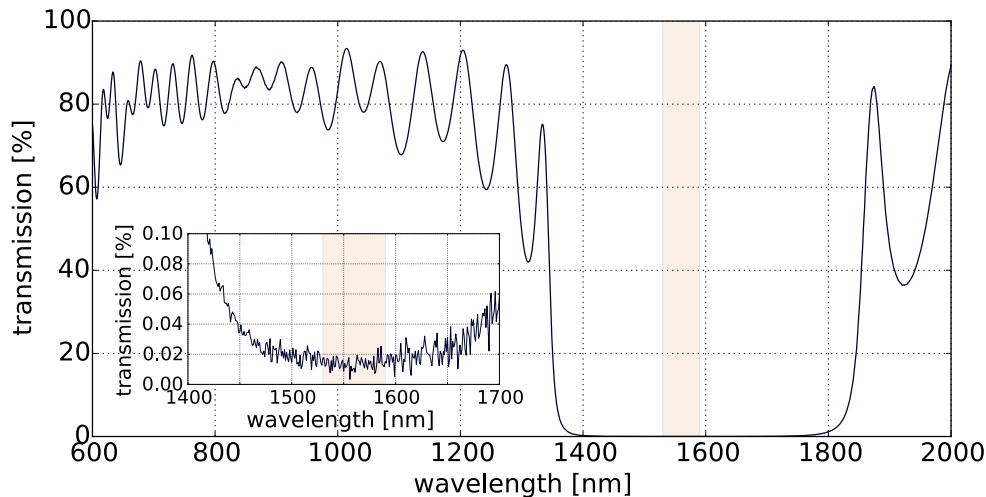


Figure 7.8 – Spectrum of a high reflective coating for 1400 nm to 1600 nm (target reflection band indicated by the orange bar) on a BK7 substrate. The inset shows a detailed view of the reflection band.

AR-HR coatings

A more advanced coating is given by a combination of anti reflective and high reflective coatings. As an example, we use the two-channel, spectrally degenerated polarisation entangled source on chip [41]. This device is pumped at a wavelength of 775 nm, which requires an anti reflection coating on the input side, as described in the previous section. The more interesting coating is on the output side of the sample. The device generates degenerated photon pairs at 1550 nm, which, on the one hand, requires an AR coating to improve the performance of the pair generation. On the other hand, we were also aiming for pump suppression, by applying an high reflective coating for 775 nm [41].

Furthermore, we created a sophisticated coating with three wavelength bands, including an AR band at 560 nm and two high reflective regions around 900 nm and 1650 nm (compare to orange bars in figure 7.9). The coating was used to enhance the performance of a quantum pulse gate, which allows for a full control over the spatiotemporal structure of quantum states of light [42, 148, 149]. This type of design requires 22 layers with a total thickness of 4750 nm. Using this coating, we achieved a transmission of more than 95% at 560 nm and a transmission of 1% at 900 nm and <1% at 1650 nm for this design.

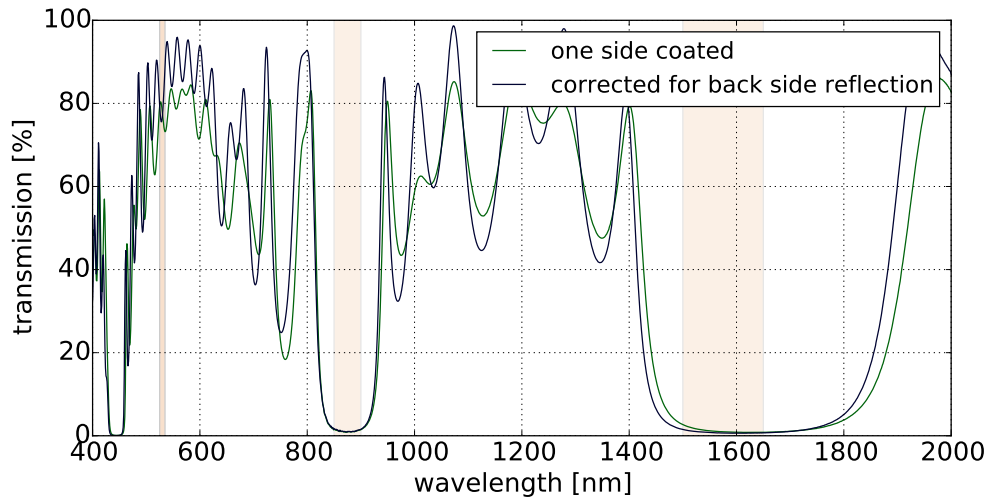


Figure 7.9 – Spectrum of a more sophisticated coating combining an AR and two HR reflection bands on a LN sample.

Partial Reflecting Coatings

Up to now, we discussed only AR and HR coatings. However, more sophisticated designs allow to create coatings with distinct partial reflection. As an example, we choose a resonator design which is pumped at 775 nm and creates squeezed light at 1550 nm [45]. For that reason, the pump light of 775 nm on the input side is transmitted via an AR coating. On the output side, the pump light is reflected back into the sample and leaves the sample on the input side (see green bar in figure 7.10). The generated light at 1550 nm interacts on the input side with a HR coating and a partial reflective coating of roughly 85% reflectivity on the output side (compare to orange bar in figure 7.10). Using this concept, we created a resonator for the generated PDC photons and achieved an optical squeezing of 4.9 dB [45]. Additionally, we also created a high-power waveguide resonator second harmonic device with external conversion efficiency up to 75% [46], by using this technique. In this experiment, the device is pumped at 1550 nm and generates SH light at 775 nm. The pump is resonant and creates stable output power of 70 mW, the laser feedback scheme locks to the maximum power immediately and has been locked stably for more than 6 hours.

Phase and GDD Optimised Coatings

In addition to the amplitude modification, we can selectively alter other parameters, such as phase and group delay dispersion (GDD). Both cannot be measured in a simple way with our spectrometer. For that reason, we present the theoretical calculations. Beginning with phase adjustments, which allows the creation of an optimised resonator. We can set the added phase during the transmission to any value between 0 and π .

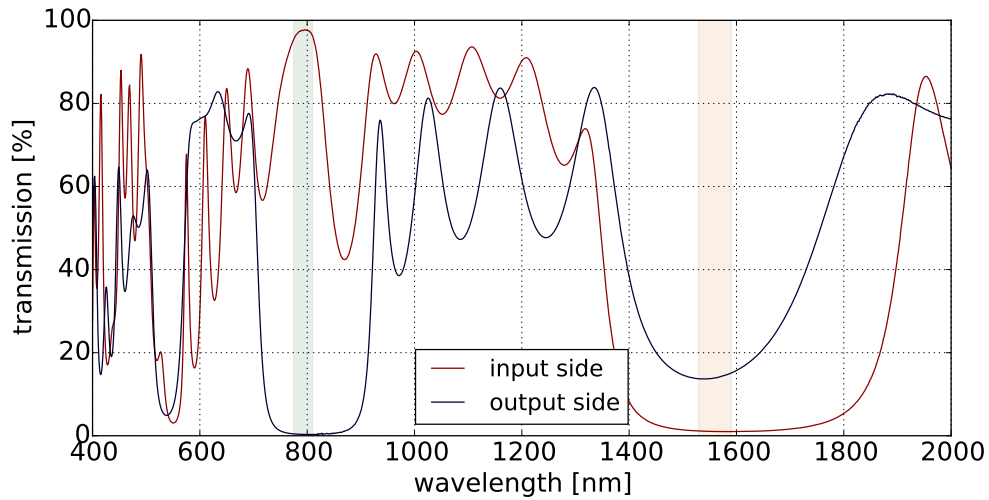


Figure 7.10 – Spectra for the input and output coating to build a resonator. The light is resonant at 1550 nm, and partially out-coupled on the output side.

For femtosecond-duration laser pulses, a pulse chirping occurs by using an unoptimised coating. By optimising the design, we can set the GDD to zero or even to negative values to compensate for chirps induced by other components in the optical setup.

All these different kinds of dielectric coatings improve the performance of the KTP and LN devices and facilitate the fabrication of tailored dielectric mirrors for optimised optical setups. Beside these applications, we developed new kinds of coating designs and applications, which we describe in the following section.

7.4.3 Novel Types of Dielectric Coatings

All previously described dielectric coatings are ideal for homogeneous deposition over the full substrate area. Our novel approach is a (linear) gradient coating, with varying optical properties that depend on the position of the impinging light. We achieve this by tilting the substrate in the calotte position.

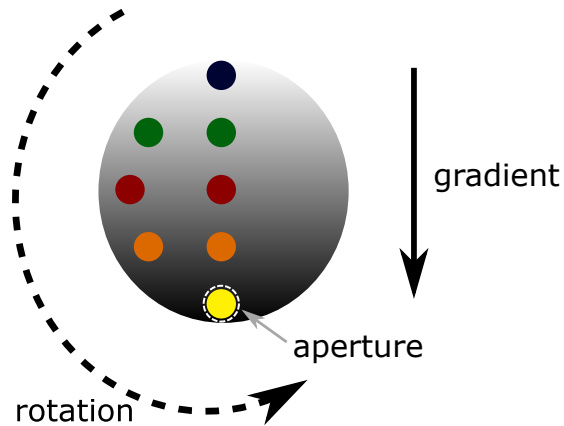


Figure 7.11 – Gradient along the filter substrate leads to a position dependent transmission and reflection characteristic of the coating. Thus, by rotating the substrate, transmission and reflection can be tuned without changing the beam direction.

The gradient is caused by two main effects. On the one hand the layer thickness variation is induced by different distances to the electron beam evaporator. On the other hand a shading by the sample holder changes the deposition rate in a position-dependent manner. Due to the fact, that the calotte rotates, the gradient occurs only in one direction of the substrate (compare to figure 7.11). With this technique, we created two different kind of devices, which will be described in the following.

Wavelength Dependent Transmission by Rotation of the Substrate

For the first application, we have to specify the requirements of the coating. The idea is to create coatings which leave one wavelength unaffected, e.g. AR coating at 775 nm, while the transmittance of a second wavelength, e.g. 1550 nm, changes. To achieve this, a broad AR coating around 775 nm and a cut-on or cut-off filter at 1550 nm is the design of choice (compare to figure 7.12). To vary the transmittance for a classical (homogeneous) coating, the filter has to be tilted which changes the transmission at the cut-on wavelength but not at the AR wavelength region. The drawback of this method is a beam displacement induced by the tilting of the substrate, which makes a re-optimisation, e.g. of fibre couplings, mandatory. This can be overcome by a linear grating filter, which can be rotated to change the optical characteristic without tilting or displacing the beam (see figure 7.11).

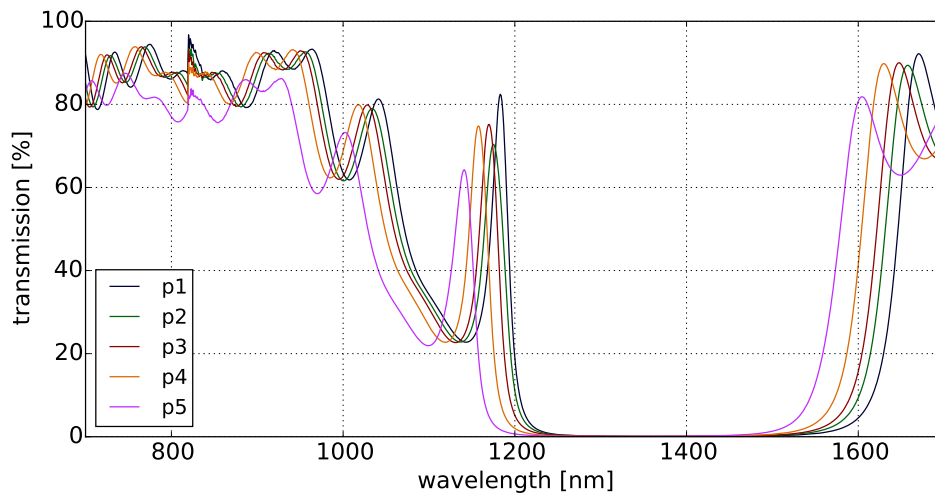


Figure 7.12 – Transmission characteristics at different positions through a gradient coating.

In our prototype we achieved a transmission contrast of 0.87 at 1605 nm, while the transmission at a wavelength of 743 nm varies less than 2% (see figure 7.13). By optimising the coating process the performance of these kinds of coatings can be further increased. This technique can be used for, more or less, any wavelength combination and can be used as well for other parameters like GDD and phase.

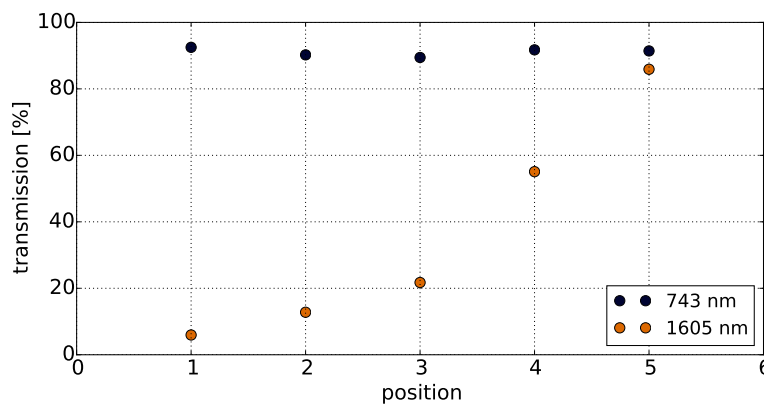


Figure 7.13 – Position dependent transmission for the target wavelengths at 743 nm (less than 2% variation) and a strong position dependent transmission at 1605 nm with a contrast of 0.87

GDD and Phase Control

The idea is not limited to transmission variation, but can also be used for phase and group delay dispersion engineering. Due to the fact, that the phase and the GDD cannot be measured in a simple way, in particular, not in our *Cary* spectrometer, it was not possible to determine the performance of such devices.

For the idea of a beam displacement free transmission variation filter and its realisation, a corresponding invention disclosure was written and submitted.

A Simple Spectrometer

The second application for a gradient coating represents a spectrometer. A needle filter, which is a very narrow bandpass, is deposited with a gradual variation in the layer thickness. This leads to a variation of the centre wavelength of the needle (compare to figure 7.14). We could achieve a variation of 30 nm over 1 inch diameter of the substrate. If we deposit this coating on a cylindrical lens and place a single line CCD behind the lens, we achieve a simple spectrometer without a slit which reduces the alignment precision (see figure 7.15). For this idea and its realisation, a second corresponding invention disclosure was written and submitted.

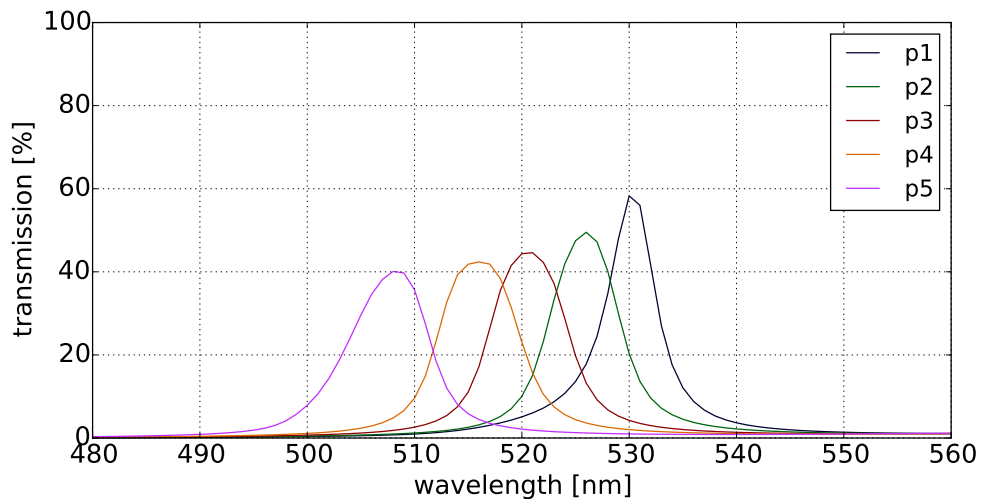


Figure 7.14 – Spectra for a needle filter on a gradient coating. The centre wavelength of the needle shifts depending on the position of the coating.

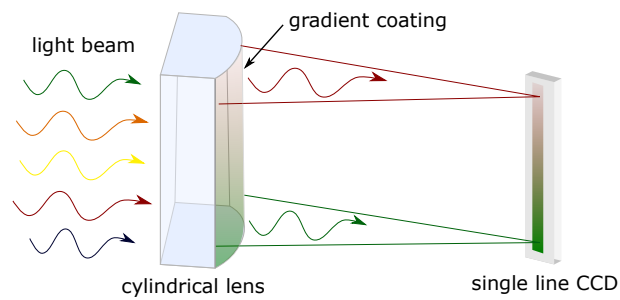


Figure 7.15 – Sketch of a simple spectrometer realisation containing a cylindrical lens with a gradient coating and a single line CCD array.

Summary

In this chapter we gave an insight into dielectric coatings. We presented the basic idea of dielectric coatings, design rules and possible ways of realising them. After the description of our coatings facility using an IAD technique in combination with a broad band monitoring, we discussed the performance of already realised dielectric coatings, mainly fabricated on the LN platform. In the end of this chapter, we described our approaches towards new coating designs in combination with an optimised deposition process, which we used to create two new kinds of devices that have been filed with the university as inventions.

Contents

8.1 Spatial Single Mode Sources at 800 nm . .	105
8.2 Ridge Waveguides	106
8.3 Channel Waveguides	119
8.4 Application Discussion	131

In chapter 6, we explained and introduced the KTP technology, which facilitates the fabrication of periodically poled waveguides in KTP. In this chapter, we demonstrate the fabrication of new kinds of devices for applications in the UV-visible wavelength regime. We start with a description of single-mode sources at

800 nm in section 8.1.1. In section 8.2 and 8.3 we describe the performance of the fabricated ridge and channel waveguides, respectively. To fully characterise the samples, we report the analysis of the linear and nonlinear optical properties.

8.1 Spatial Single Mode Sources at 800 nm

KTP is an excellent material for applications in the visible wavelength regime due to the low photorefraction and the high damage threshold. Second harmonic generation has advantages for a variety of applications. First of all, with the help of SHG it is possible to generate coherent light at wavelengths inaccessible by usual laser diode technology. Some applications require properties which cannot be accessed in laser diodes but in nonlinear conversion processes, e.g. coherence between different pulses by choosing an ideal pump light source, the pulse duration can be as low as in the fs-regime. By using resonators, the linewidth of the light source can be very small [45, 46]. The inverse process of SHG is used to generate single-mode squeezed light, which has applications in e.g. optical high-precision measurements, first of all, in laser interferometers [150].

In this thesis, we focus on a new kind of KTP device. The goal is the fabrication of a periodically poled spatially single-mode source at 800 nm. This source can be used to generate SHG around 400 nm or, conversely, to generate photon pairs via a PDC process by using a pump laser at this wavelength. The single-mode operation at 800 nm means that the PDC photons are generated in only one spatial mode. Hence, only processes involving the fundamental mode at 800 nm are allowed. This removes the necessity of spectrally filtering the downconverted photons to achieve high modal purity that is PDC emission into only one spatio-spectral mode pair. Moreover, the spatial modes of the emitted photons will match more closely the mode of a standard single-mode fibre for 800 nm, thus granting a high coupling efficiency to fibres.

8.1.1 KTP Sources in the Visible Regime

Generation and manipulation of light in the UV with reasonable power levels is still a challenging task. Many applications require photon sources at specific wavelengths with particular modal properties, i.e. polarisation, space, time and frequency. Laser diodes can address several wavelengths but the tuning range is limited to a few nanometers [151]. Moreover, for fs-pulsed operation no laser diodes are available. More advanced applications require a coherence between pump pulse and SH pulse, e.g. as a local oscillator for quantum optical applications [28]. Due to the challenging fabrication of single-mode waveguides in the visible, most of the systems employ multi-mode waveguides. These are not optimal, since they require great effort to couple light into the correct spatial mode, therefore limiting the efficiency of these devices. The only periodically poled KTP waveguide with single-mode operation at 800 nm has been realised by Huber and Laurell with femtosecond laser writing [121]. In a periodically poled bulk KTP crystal, they inscribed two double tracks close to each other, increasing the density of the crystal within the tracks and thus creating a guiding region.

Also, the performance of photon pair generation via PDC processes is limited by mode coupling. Spatial multi-modeness hindered the performance of the PDC sources in KTP waveguides generating single photons at 800nm; the different spatial modes coupled to the waveguide would generate photon pairs at different wavelengths, thus requiring spectral filtering to increase the modal purity [40].

The advantage of employing a single-mode waveguide at 800 nm would be the increase of the performance of the device. To overcome the difficulties by using multi-mode waveguides, we developed two sources, one with ridge and one with channel waveguides which operate in the single-mode regime at 800 nm.

8.2 Ridge Waveguides

One of the two types of structures investigated in this thesis are periodically poled ridge waveguides in KTP. Ridge waveguides offer a higher mode overlap between the involved fields compared to channel waveguides due to the higher mode confinement in the ridges. This is achieved by a larger refractive index step from the waveguide to the surrounding material. In the next sections, we show the state of the art of ridge waveguide fabrication. Before we started with the ridge fabrication, we modelled the ridges to reduce the parameter range for single-mode operation in the visible regime. In the following sections, we explain the fabrication of such samples and show the results we obtained in the optical characterisation.

8.2.1 State of the Art: Ridge Waveguides

The fabrication of ridge waveguides is an emerging technology. In LN, ridge waveguides represent the most efficient type of waveguide sources [152]. In KTP, Wang *et al.* fabricated the first ridge waveguide by Si-ion implantation and a subsequent ridge dicing [153]. Another promising technique is the waveguide fabrication through carbon ion irradiation followed by precise diamond blade dicing [126].

In 2017, Volk *et al.* were the first to demonstrate waveguides in KTP by ridge dicing and subsequent exchange of Rb-ions [154]. To achieve confinement along the depth, they diced grooves on the b surface of KTP crystal and subsequently performed a Rb-exchange. Due to the predominant exchange along the c-direction, the Rb-exchange takes place along the diced grooves and creates a layer of increased refractive index at the top of the crystal. A subsequent dicing creates the second edge of the ridge. To homogenise the exchange profile and achieve symmetric distribution of the refractive index, an annealing step is required [154]. Losses of 0.3 dB/cm (0.4 dB/cm) for TM (TE) polarisation were measured at 1060 nm in these waveguides. They demonstrated birefringent second harmonic generation from 1064 nm to 532 nm in b-cut KTP ridge waveguides.

However, this limits the wavelength range to a very small range. Only the combination with a periodic poling brings into reach applications in the whole transparency range of the material. The technique employed to create the birefringent KTP ridge waveguide is impractical for the realisation of poled structures, since the diced waveguides are created in b-cut crystals, while the best poling is obtained in c-cut crystals. For that reason, we decide to realise the desired poling in c-cut KTP crystal and, in a second step, fabricate the waveguides [3, 4].

8.2.2 Ridge Waveguide Modelling

The most straightforward way to fabricate ridge waveguides in c-cut crystals consists in performing a planar Rb-exchange to define the depth (confinement) of the waveguides and subsequently dice the ridges to define the width (confinement). To achieve good depth confinement, it is necessary to ensure that the height of the waveguides is greater than the exchange depth. Before starting with the fabrication, it is important to identify the main parameters that can affect the performance of such waveguides. For this reason, we simulated several structures with different sets of parameters. With the help of a finite element model software (FEMsim tool from RSoft) we were able to extract information about the guiding properties in such structures. Figure 8.1 shows an example of the structure under investigation.

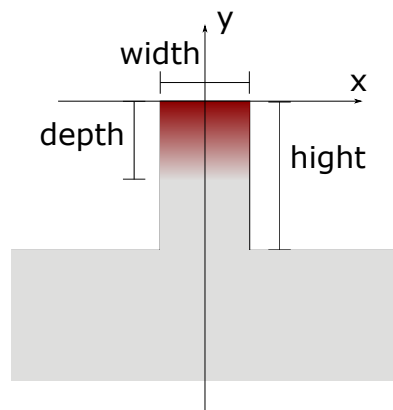


Figure 8.1 – Sketch of the simulated structures for ridge waveguides. The red area indicates the rubidium exchanged region.

The Rb-exchange on the -c face of the KTP crystal causes a refractive index increase that can be described by a complementary error function, namely:

$$\Delta n(x, y) = \Delta n_0(x, y) \cdot \operatorname{erfc}\left(\frac{y}{d}\right) \quad \text{for } y \leq 0 \quad (8.1)$$

After the dicing, the waveguides will have a width w and a height h . The overall refractive index distribution can therefore be described by

$$n^{pol}(x, y) = \begin{cases} 1 & \text{for } y > 0 \text{ or } (y > 0 \wedge |x| > \frac{w}{2}) \\ \Delta n_{\text{substrate}}^{pol}(x, y) + \Delta n_0^{pol}(x, y) \cdot \operatorname{erfc}\left(\frac{y}{d}\right) & \text{elsewhere} \end{cases} \quad (8.2)$$

As can be seen from the general expression for $n(x, y)$, in the most basic model there are at least four different parameters that can in principle influence the properties of ridge structures, namely:

- the refractive index increase at the surface Δn_0
- the Rb-exchange depth d
- the width w of the ridge
- the height h of the ridge

In the fabrication stage, we can precisely control three of these four parameters namely the width and the height of the ridge and the exchange depth of the Rb-ions. The refractive index increase Δn_0 is more difficult to control and therefore we investigated its impact on the guiding properties of the waveguide.

We simulated structures with different set of parameters $\{\Delta n_0, d, w, h\}$ to understand the guiding of our waveguides. The simulation domain was chosen to be rectangular with dimensions $[-15 \mu\text{m}, 15 \mu\text{m}] \times [-30 \mu\text{m}, 2 \mu\text{m}]$, with a grid size of $0.1 \mu\text{m}$ in both dimensions. The structure parameters were varied in the following ranges:

- $w = [1.5, 2.0, 2.5, 3.0, 3.5, 4.0, 4.5] \mu\text{m}$
- $h = [10, 15, 20] \mu\text{m}$
- $d = [6.0, 6.5, 7.0, 7.5] \mu\text{m}$
- $\Delta n_0 = [0.001 - 0.06]$

If the condition $h < d$ (the Rb-exchange is deeper than the diced ridge) is fulfilled the structure starts behaving more like a planar rather than a ridge waveguide. Therefore, we set the combination of h and d such that $h > d$. If we assume that the refractive index increase is caused only by exchanging Rb against K-ions, and neglect additional stress induced refractive index variations, the maximum refractive index increase at 800 nm is $\Delta n_{0max} = n_{\text{RTP}} - n_{\text{KTP}} = 0.06$ (n_{KTP} [113] and n_{RTP} [155]).

Simulation Results

We analysed the symmetry of the fundamental modes at 800 nm and plotted the full width at half maximum (FWHM) of the electric field of the fundamental mode depending on the different parameters (see figure 8.2). In the following, we use a refractive index increase at the surface of $\Delta n_0 = 0.011$, which gives the best mode overlap to the measured mode, as we will see later on. For the different ridge heights, we see no difference in the guiding properties. For ridge widths below 3.0 μm , we observe a cut-off behaviour that is, the waveguide isn't guiding the 800 nm light anymore.

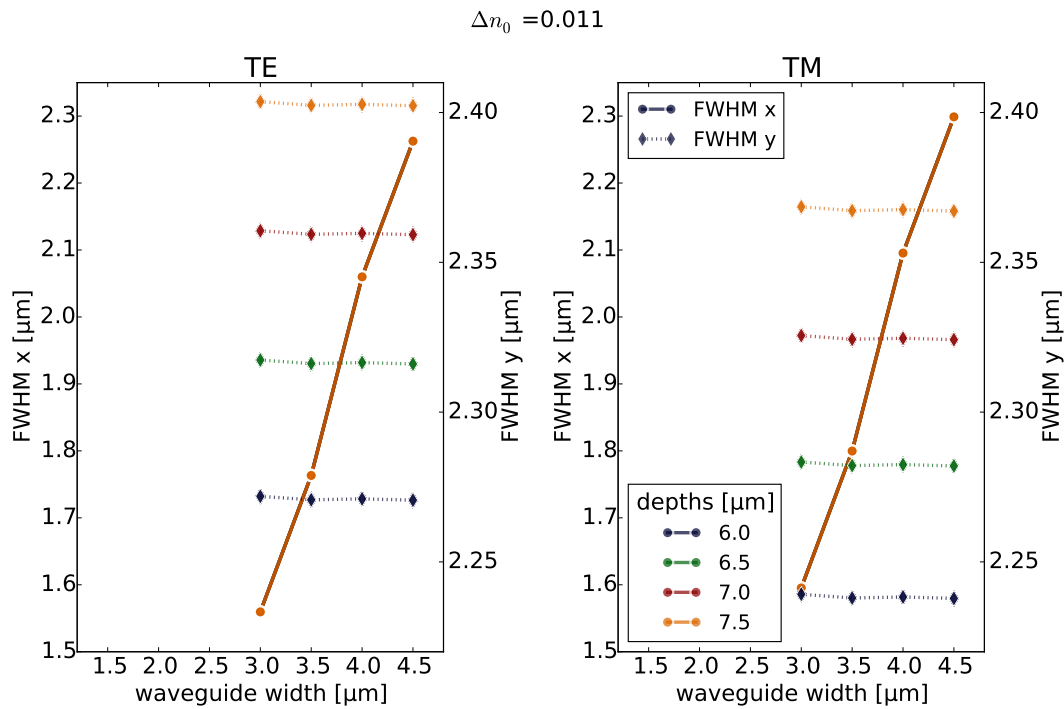


Figure 8.2 – FWHM of the simulated modes in lateral and vertical directions for a refractive index increase of $\Delta n_0 = 0.011$ and a ridge height of $h = 20 \mu\text{m}$. The waveguide width w and the exchange depth d are varied.

Moreover, it can be noted that the FWHM in x-direction depends on the width and is independent from h and d , while the FWHM in y-direction is mainly dependent on d and independent from h . Using these parameters as a starting point, it should be possible to fabricate single-mode waveguides around 800 nm. In the next section, we explain the ridge fabrication including the periodic poling and the rubidium exchange with a subsequent ridge dicing.

8.2.3 Ridge Waveguide Fabrication

We fabricated ridge waveguides in KTP samples with dimensions of $14 \times 6 \times 1 \text{ mm}^3$ along the crystallographic a, b and c axes. At first, the samples are treated in a pure KNO_3 melt to homogenize the sample composition to improve the exchange and poling homogeneity (compare to section 6.2.3.1). In a second step, the samples are periodically poled with periods from $7.2 \text{ }\mu\text{m}$ to $7.5 \text{ }\mu\text{m}$, before the waveguides are diced.

The poling period for a frequency conversion from 800 nm to 400 nm is calculated using equation 5.29; the refractive index of the bulk substrate is determined by equation 5.49 and the refractive index increase due to the rubidium exchange is estimated by equation 5.50. Details about the phase matching calculation will be discussed in section 8.2.4.3. We used the same process steps as described in section 6.2.2.4. As we do the poling before the exchange, we choose the -c face for periodic resist structuring due to the higher domain nucleation rate. After the photo resist definition and a thermal hard bake to make the photo resist more stable against the electrolyte, both sides (+c and -c) are coated with a 60 nm layer of Au/Pd to improve the electrical contact. For the electrical contact, we used an aqueous mixture of potassium chloride (KCl) and isopropyl alcohol (see section 6.2.2.3). We applied five high voltage pulses of 2.3 kV to invert the spontaneous polarisation. The pulses had a trapezoidal shape with 1 ms rise and fall time and a 2 ms plateau. To control the poling progress, we used an in-situ monitoring technique (as discussed in section 6.1.1.2) which is based on electro-optically induced polarisation rotation of a laser beam. After successful poling, we removed the metal electrodes and photo resist in an ammonia solution. This solution acts also as a weak selective etchant to visualize the domain structure, see figure 8.3 b). Next, we fabricated waveguides in the periodically poled substrates. For the mode confinement in the depth direction, a planar waveguide was formed by a maskless ion exchange in a Rb-nitrate (RbNO_3) bath. The bath consists of a mixture of 97% Rb-nitrate (RbNO_3), 2% K-nitrate (KNO_3) and 1% Ba-nitrate ($\text{Ba(NO}_3)_2$). The exchange temperature was set to $330 \text{ }^\circ\text{C}$ and the exchange time to one hour. An exchange depth of $6.2 \text{ }\mu\text{m}$ was determined (with an accuracy of up to $\pm 0.4 \text{ }\mu\text{m}$) by energy-dispersive X-ray spectroscopy (EDX) measurements of the Rb concentration with an electron beam microscope (compare section 6.1.3).

8.2.3.1 Ridge Dicing

This sample was sent to Hamburg for a subsequent ridge definition with a diamond-blade dicing saw, as shown in figure 8.3a). The detailed fabrication steps of the dicing process are described in section 6.2.5. These ridges were diced into the former -c face and parallel to the a-axis. After preparing the ridges, the end facets were also smoothed with the dicing saw, to facilitate subsequent incoupling of light.

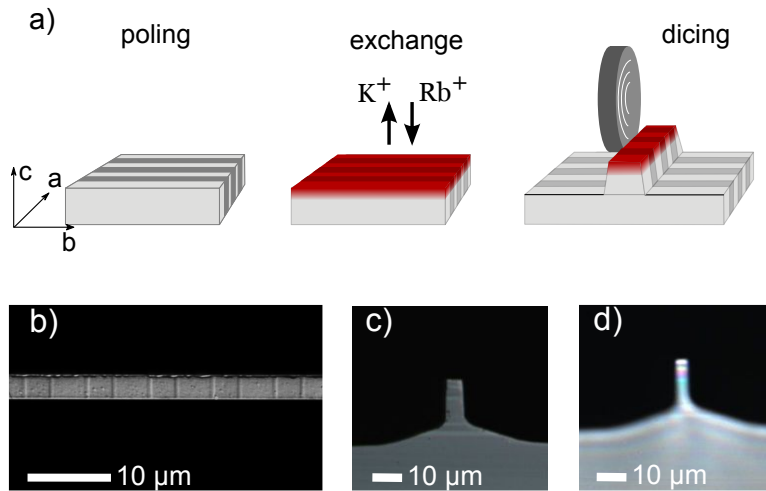


Figure 8.3 – a) Waveguides were formed in periodically poled KTP by Rb-exchange and subsequent ridge definition. SEM image of b) a selectively etched surface of a periodically poled ridge (top view) and of a c) waveguide end facet; d) light image of a waveguide end facet.

Electron microscope (SEM) images of final ridge waveguides are presented in figure 8.3b) and c), showing sharp edges and smooth surfaces. Using a white light interferometer, we measured a side wall roughness of 1-2 nm. We prepared ridges of widths between 1.9 μm and 12 μm and heights between 10 μm and 20 μm . Due to the Rb-exchange, the waveguides are brittle and can be easily damaged by mechanical stress, e.g. during the dicing process. The dicing technique is not ideal for end facet preparation because chipping reduces the end facet quality. Therefore, quantitative loss measurements and mode field analysis measurements were only possible on a few waveguides of the present sample. An improved end facet preparation technique is currently under development.

8.2.4 Optical Characterisation of Ridge Waveguides

For the SHG experiments (section 8.2.4.4) we used ridge waveguides with 2.6 μm to 3.6 μm width. For all optical characterisations, we used a similar optical setup, which is shown in figure 8.4. First, we studied their linear optical properties starting with the transmission losses of the ridge waveguides and discussing the spatial mode images of the ridge waveguides.

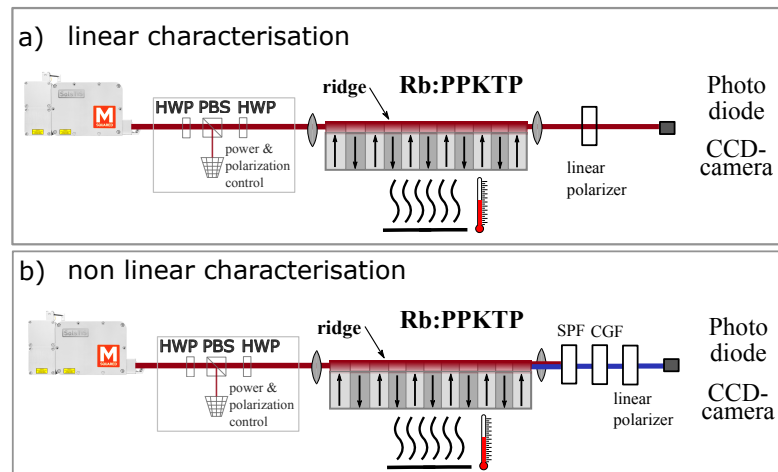


Figure 8.4 – Optical setup to investigate the optical properties of the ridge waveguides. Power and polarisation are controlled by a combination of a half wave plate (HWP), a polarising beam splitter (PBS) and an additional HWP. The light is coupled with an 8 mm lens into the waveguide. The generated light is collimated with an AR coated lens. For the linear characterisation in figure a) we use an AR coated lens at 800 nm and a linear polariser to distinguish TE and TM modes. For the nonlinear characterisation, we use an AR coated lens at 400 nm. The pump light is filtered with a short pass filter (SPF) and an additional colour glass filter (CGF). The linear polariser allows for an analysis of the SH light polarisation.

8.2.4.1 Transmission Losses in Ridge Waveguides

To estimate the transmission losses, we used different techniques. e.g. maximum through coupling, cut-back [156] and Fabry-Perot method [157]. Cut-back represents a simple method for direct measurement of transmission losses of waveguides by comparing the transmission of light in waveguides with different lengths. However, it is a challenging task to prepare waveguides with equal quality and different lengths. Thus, the measurement is done by cutting a sample into smaller pieces with different lengths to vary the waveguide lengths. Being a destructive measurement, we didn't use this technique with the sample that was intended for the final measurements. A good compromise is to perform such a measurement on samples processed in parallel with the chosen one, to have similar fabrication condition and therefore have a more trustworthy value for the losses.

The waveguide can be considered as a low finesse resonator. In 1985, Regener and Sohler showed that the contrast of the fringes, related to a change in the optical length, can be used to estimate the transmission losses of a waveguide [157]. Changing the resonator conditions can be achieved, e.g. by temperature or wavelength tuning. The Fabry-Perot technique requires exact knowledge of the end facet reflectivity. As mentioned in the fabrication section (section 8.2.3.1),

the end facet quality is not as good as in polished samples. The unknown reflectivity of the end facets impacts the loss measurement, causing an overestimation of the losses, as compared to the cut-back and the through coupling methods.

Losses at 800 nm

To measure the losses at 800 nm light, we used the Fabry-Perot technique and measured losses of 8 dB/cm. Total transmission through the waveguide was measured at a wavelength of 794 nm. The overall transmission through the sample was 29.6% (25.3%) for TE (TM), corresponding to 24.5% (21%) when corrected for Fresnel reflection on the end facets of ($R_{TE}=0.075$, $R_{TM}=0.084$), but not for the coupling efficiency. The corresponding losses are 5.9 dB/cm (6.7 dB/cm) for TE (TM) polarisation. However, we know that the quality of the end facet, and thus the coupling efficiency, has been the limiting factor of these measurements. Hence, we assume that the real waveguide losses are much lower, which could also be confirmed by characterising comparable samples, which have losses of about 1.5 dB/cm in the telecom range [3].

Losses at 1550 nm

In another sample (see [3]), which exhibits single-mode guiding at 1550 nm, we measured the losses at telecom wavelengths. We tried to use the Fabry-Perot method to measure the losses, but none of the inspected samples showed a high contrast. The corresponding attenuations were >6 dB/cm. We attribute this to the bad end facet quality, which does not allow for reliable measurements. Using the cut-back method for a sample of initial length 8.4mm (and subsequently cut into two pieces of lengths 6.9 mm and 1.4 mm), for ridges with widths larger than $9.5 \mu\text{m}$, we measured attenuation of 1.3 dB/cm (1.6 dB/cm) for TE (TM) polarisation at 1550 nm, respectively. The measured total insertion loss can be as low as 2.6 dB for both polarisations.

8.2.4.2 Spatial Modes in Ridge Waveguides

We measured the near field of the fundamental modes at 800 nm using the optical setup explained in figure 8.4a). We confirmed that some of the fabricated ridge waveguides exhibit single-mode guiding at 800 nm (compare to figure 8.5). At waveguide widths of $3.2 \mu\text{m}$ a second mode appears. The measured mode profiles are in a good agreement with the previously calculated modes. By knowing the waveguide width ($3.1 \mu\text{m}$) and exchanged depth ($5.7 \mu\text{m}$), we used a finite element method program (FEMSim tool from RSoft) to model the expected mode. The waveguides used to characterise the nonlinear behaviour of the ridge waveguides have a width between $2.2 - 3.1 \mu\text{m}$ and guide only one mode at 800 nm.

The fitting parameter was the refractive index increase at the surface. For the refractive index increase at the surface we thereby estimated $\Delta n_{TE} = 0.011 \pm 0.005$ for TE and $\Delta n_{TM} = 0.011 \pm 0.005$ for TM polarisation, as well. The field overlap of the calculated and the measured mode was above 0.96, for both TE and TM modes, indicating a good fit. Using this model as a starting point, we calculated the estimated phase matching spectrum for a type-II process.

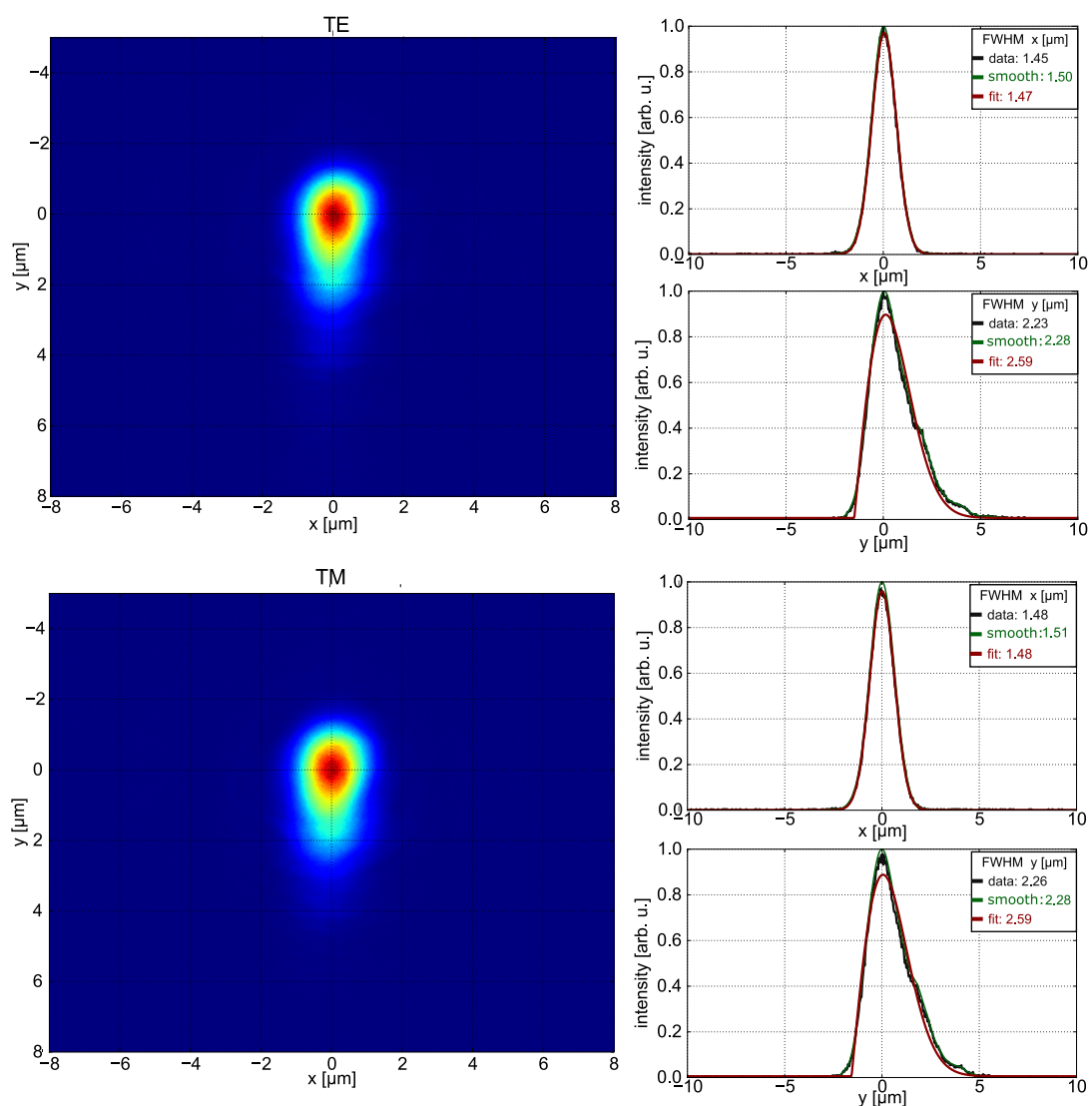


Figure 8.5 – Experimentally measured near field of the spatial modes at 800 nm for TE and TM polarisation. On the right hand side, we plot an x - and y -cut, passing through the peak. The mode symmetry in lateral and vertical directions are calculated for raw, smoothed (averaged over 4 data-points) and fit data. For the lateral direction we fit a Gaussian and in the vertical direction a Hermite-Gaussian function.

8.2.4.3 Phase Matching in Ridge Waveguides

To estimate the poling period, which is required for a type-II SH conversion from 800 nm to 400 nm we calculated the phase matching spectrum using equation 8.3.

$$\Delta k = \frac{2\pi \cdot n_{y\text{-eff}}(\lambda_{\text{SH}})}{\lambda_{\text{SH}}} - \frac{2\pi \cdot n_{y\text{-eff}}(\lambda_{\text{pump}})}{\lambda_{\text{pump}}} - \frac{2\pi \cdot n_{z\text{-eff}}(\lambda_{\text{pump}})}{\lambda_{\text{pump}}} - \frac{2\pi}{\Lambda} \quad (8.3)$$

For the indices $n_i(\lambda)$ we used the Sellmeier equations for bulk KTP $n_{i(\text{bulk})}(\lambda)$ [113] and a modification to describe the refractive index increase of the Rb-exchange $\Delta n_{i(\text{waveguide})}(\lambda)$ [105]

$$n_i(\lambda) = n_{i(\text{bulk})}(\lambda) + \Delta n_{i(\text{waveguide})}(\lambda). \quad (8.4)$$

It has to be noted, that we are using the refractive index increase at the surface Δn_0 instead of the n_{eff} . This model is optimised for conversion processes at telecom wavelengths around 1550 nm. Thus, we are using a second model, assuming a constant refractive index increase $\Delta n_{i(\text{waveguide})}$ in the waveguide, which shows dispersion only in the bulk refractive index. The refractive index for a constant increase can be written as

$$n_{i(\text{const})}(\lambda) = n_{i(\text{bulk})}(\lambda) + \Delta n_{i(\text{const})}. \quad (8.5)$$

Combining equation 8.4 for the dispersive waveguide model as well as equation 8.5 for the constant model in equation 8.3 and considering a poling period of 7.35 μm , it is possible to determine the phase matching curves for bulk and the two waveguide models (see figure 8.6).

The dispersion model predicts the phase matching for rubidium exchanged channel waveguides, guiding in a single-mode regime at 1550 nm very well [37]. As seen in figure 8.6, the model predicts SHG at 386 nm and 401 nm for the bulk and waveguide model, respectively. As we will show in section 8.2.4.4, the measured wavelength is 393 nm, which is marked by the blue cross in figure 8.6. We found that the best model to match the measured data assumes a dispersionless refractive index increase Δn_0 , that provides the phase matching curves in red in figure 8.6.

8.2.4.4 Second Harmonic Generation in Ridge Waveguides

We used waveguides with poling periods in the range of 7.35 - 7.50 μm and widths of 2.6 - 3.6 μm to probe the nonlinear behaviour via second harmonic generation. Linearly polarised light from a Ti:Sapphire laser (M2 SolsTis) at 800 nm with a rotation of 45° with respect to the c-axis is coupled to the ridge waveguide via lens coupling (compare to figure 8.4b)). Power and polarisation were controlled with a polarising beam splitter and a half-wave plate. In the waveguide, horizontally polarised light was generated in a type-II phase-matched process at half of the pump wavelength. After the waveguide, we used a short-pass and a colour glass filter to suppress the pump light. We used a power meter to measure the generated output power as function of the fundamental wavelength. A measured phase matching curve is shown in figure 8.7a) (blue line). Measurements essentially showed the expected sinc-function, with superimposed Fabry-Perot type oscillations. We attribute deviations of the envelope of the measured phase-matching from an ideal sinc-function to inhomogeneities in the poling and the waveguide itself.

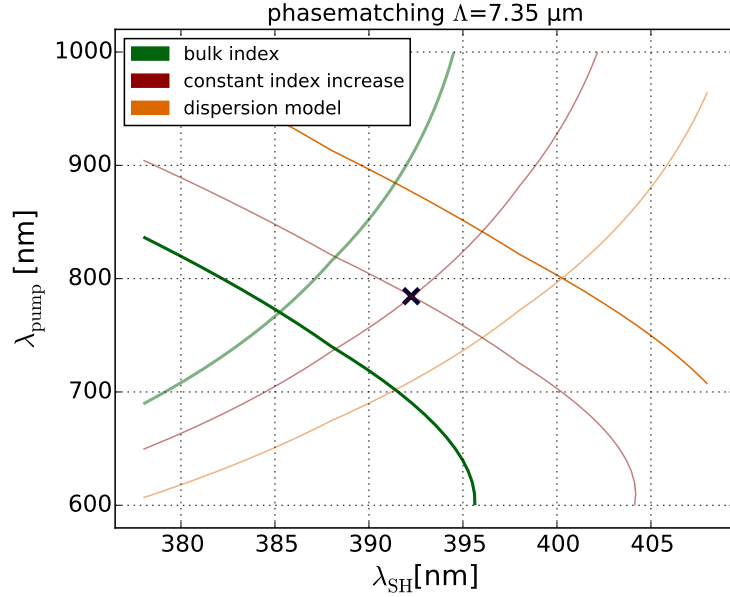


Figure 8.6 – Calculated phase matching function for bulk KTP [104] (green line), bulk index with constant index increase of $\Delta n_0 = 0.015$ (red line), and for the dispersion model [105] (orange line). The blue cross indicates the phase matching we obtained during our experiments.

We fit a sinc function

$$P_{\text{SHG, norm}} = \text{sinc}^2 \left(\Delta k \frac{l}{2} \right) \quad (8.6)$$

to the measured data. Here Δk represents the phase mismatch (compare to equation 8.3). It has to be noted that we are using the refractive index increase at the surface of the waveguide Δn_0 instead of the n_{eff} , for the bandwidth calculation. The maximum of the sinc function was set to the maximum of the data, and the fitting parameter was the effective length l_{eff} , which is reduced compared to the length of the periodically poled area. Longer poling lengths lead to a smaller phase matching bandwidth. Any error in the poling (e.g. missing domains) or the waveguide symmetry broadens it. We obtained the best fit for an effective length of 2.75 mm (figure 8.7a, red line).

We measured the temperature dependence of the phase matching to be 53 pm/K in a range from 20 °C to 60 °C (see figure 8.7b), which is in good agreement with temperature dependent phase matching measurements in PPKTP bulk crystals (60 pm/K) [158]. The device showed a temperature insensitive behaviour which allows for stable operation, independently of the ambient conditions.

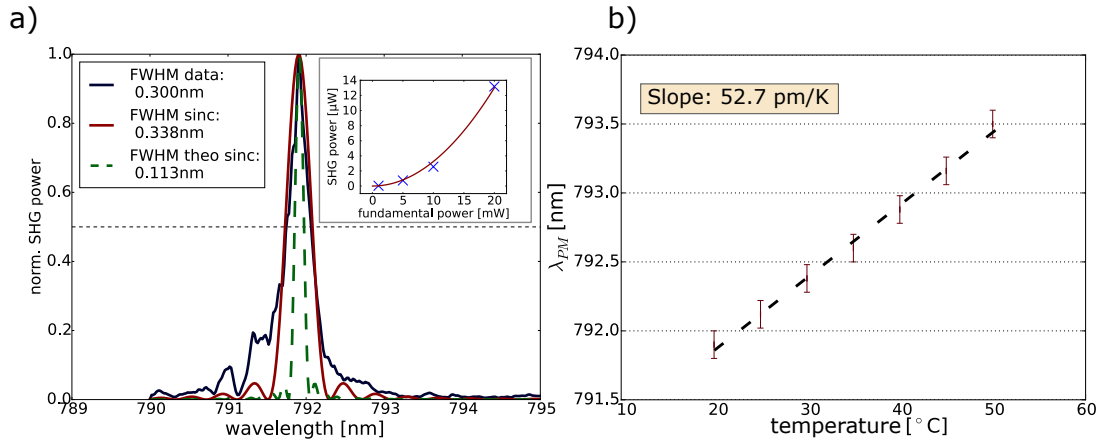


Figure 8.7 – a) Measured (blue) and calculated (red) phase matching curve of a 2.6 μm wide and 7.9 mm long ridge waveguide for type-II conversion; the calculated curve (green) corresponds to a poling length equal to the sample length of 7.9 mm. The inset shows the Input-Output curve of fundamental to second harmonic power. b) Temperature dependence of the phase matching.

The highest conversion efficiency of $\eta_{\text{exp}} = 6.6 \text{ \%}/\text{W} \cdot \text{cm}^2$ was found for a 2.6 μm wide ridge of length $l=7.9$ mm, a poling period of 7.35 μm , a pump wavelength of 792.2 nm and a pump power of 11.3 mW. The SHG efficiency was calculated as

$$\eta_{\text{exp}} = \frac{P_{\text{SHG}}}{P_{\text{pump}}^2 \cdot l^2} \cdot 100\% = 6.6 \frac{\%}{\text{W} \cdot \text{cm}^2}, \quad (8.7)$$

where P_{SHG} is the second harmonic power, P_{pump} is the pump power behind the waveguide and l is the length of the poled fraction of the crystal. The efficiency was corrected for end facet reflection losses and transmission losses of the short-pass filter and the colour glass filter (see figure 8.8).

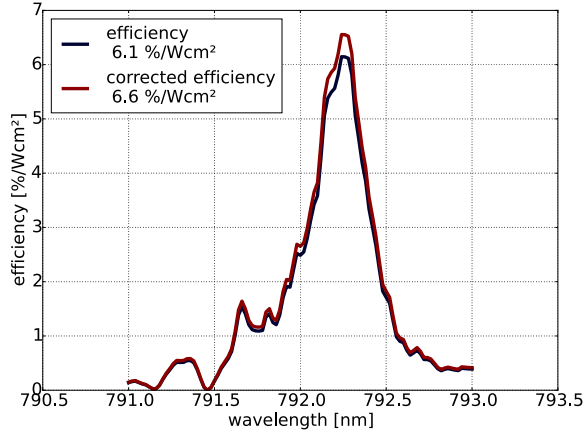


Figure 8.8 – Measured (blue line) and corrected (red line) SHG conversion efficiency in the ridge waveguide.

We also determined the theoretically expected efficiency. Therefore, we calculated the overlap integral S by integrating the scalar amplitude of the electric field distributions of the two pump fields ($E_{\text{pump-TE}}$, $E_{\text{pump-TM}}$) and the SH field ($E_{\text{SH-TE}}$). We obtained these values from calculated modes in RSoft using the same refractive index increase for fundamental and second harmonic mode. The obtained value of $S = 0.34 \mu\text{m}^{-1}$ was used to calculate a theoretically expected efficiency of

$$\eta_{\text{theo}} = \frac{8\pi^2 d_{\text{QPM}}^2 S^2}{n^3 c \epsilon_0 \lambda_{\text{pump}}^2} = 12.4 \frac{\%}{\text{W} \cdot \text{cm}^2}. \quad (8.8)$$

Here c is the speed of light, $n = 1.84$ is the refractive index of the SH wave [113], λ_{pump} is the pump wavelength, and $d_{\text{QPM}} = 2/\pi \cdot d_{24} = 2/\pi \cdot 1.9 \text{ pm/V}$ [159]. The deviation by a factor of 2 between experimental and theoretical efficiency is expected to be caused partially by waveguide losses and inhomogeneities, which arise especially for the SH modes, and eventually by deviations of the simulated mode overlap from the real one.

8.2.4.5 Ridge Waveguide Summary

Using a diamond-blade dicing saw and Rb-exchange, we have fabricated periodically poled ridge waveguides in c-cut KTP with low surface roughness, which allows for relatively low losses. Furthermore, we successfully demonstrated type-II second harmonic generation in a periodically poled (7.35 μm poling period) ridge waveguide. We analysed the performance of the ridge waveguides and demonstrated efficient second harmonic generation (SHG) from 792.2 nm to 396.1 nm with normalised conversion efficiency of 6.6 $\%/\text{W} \cdot \text{cm}^2$. The measured bandwidth of 0.34 nm and the low temperature dependence of 53 pm/K pave the way towards further exploration of a class of devices suitable for a broad range of environmental conditions. Such c-cut ridge waveguides are good candidates for highly-efficient nonlinear frequency conversion devices.

8.3 Channel Waveguides

The second type of devices we developed are rubidium exchanged channel waveguides. Channel waveguides promise a higher flexibility in the guiding design than ridge waveguides. In channel waveguides, straight channels, tapers and couplers can be realised [160–162]. We focus on periodically poled channel waveguides operating in a single-mode regime around 800 nm. Before we started with the waveguide fabrication, we modelled the waveguides using a finite element method. In the further sections, we explain the fabrication of such samples and show the results we obtained in the optical characterisation.

8.3.1 Channel Waveguide Modelling

Before starting with the fabrication, we simulated several structures with different sets of parameters, comparable to the ridge waveguide structures. Figure 8.9 shows an example of the

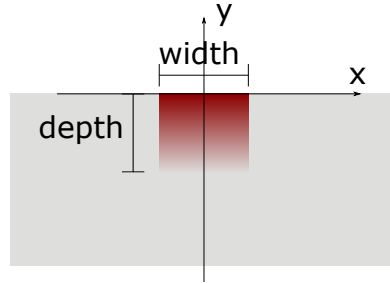


Figure 8.9 – Sketch of the simulated structures of the channel waveguides.

structure under investigation. The Rb-exchange on the $-c$ face of the KTP crystal causes a refractive index increase that can be described by a complementary error function, compare to formula 5.46. After exchange, the waveguides will have a width w and an exchange depth d . The overall refractive index distribution can therefore be described by

$$n^{pol}(x, y) \begin{cases} 1 & \text{for } y > 0 \\ n_{\text{substrate}}^{pol}(x, y) & (y < 0 \wedge |x| > \frac{w}{2}) \\ n_{\text{substrate}}^{pol}(x, y) + \Delta n_0^{pol}(x, y) \cdot \text{erfc}\left(\frac{y}{d}\right) & \text{elsewhere} \end{cases} \quad (8.9)$$

As can be seen from the general expression for $n(x, y)$, in the most basic model there are at least three different parameters that can, in principle, influence the properties of channel waveguides, namely:

- the refractive index increase at the surface Δn_0 ,
- the Rb-exchange depth d ,
- the width w of the channel.

During the fabrication of channel waveguide structures, we can control properly two of these three parameters, namely, the width and the exchange depth of the Rb-exchange. The refractive

index increase Δn_0 is more difficult to control and therefore we analysed this behaviour to understand how much a variation can affect the guiding properties. The structure parameters were varied over the following ranges:

- $w = [1.5, 2.0, 2.5, 3.0, 3.5, 4.0, 4.5] \mu\text{m}$
- $d = [6.0, 6.5, 7.0, 7.5] \mu\text{m}$
- $\Delta n_0 = [0.001 - 0.06]$ in steps of 0.001.

As in the ridge waveguide simulations, we assume the maximum refractive index increase by $\Delta n_{0max} = n_{RTP} - n_{KTP} = 0.06$ (n_{KTP} [113] and n_{RTP} [155]) at 800 nm wavelength.

Simulation Results

We analysed the symmetry of the fundamental modes and plotted the FWHM of the electric field of the fundamental mode depending on the different parameters (compare to figure 8.10). In the following, we use a refractive index increase at the surface of $\Delta n_0 = 0.010$. In the analysed parameter range, waveguides which have depths less than $7 \mu\text{m}$ and widths less than $4 \mu\text{m}$ show single-mode guiding behaviours at 800 nm.

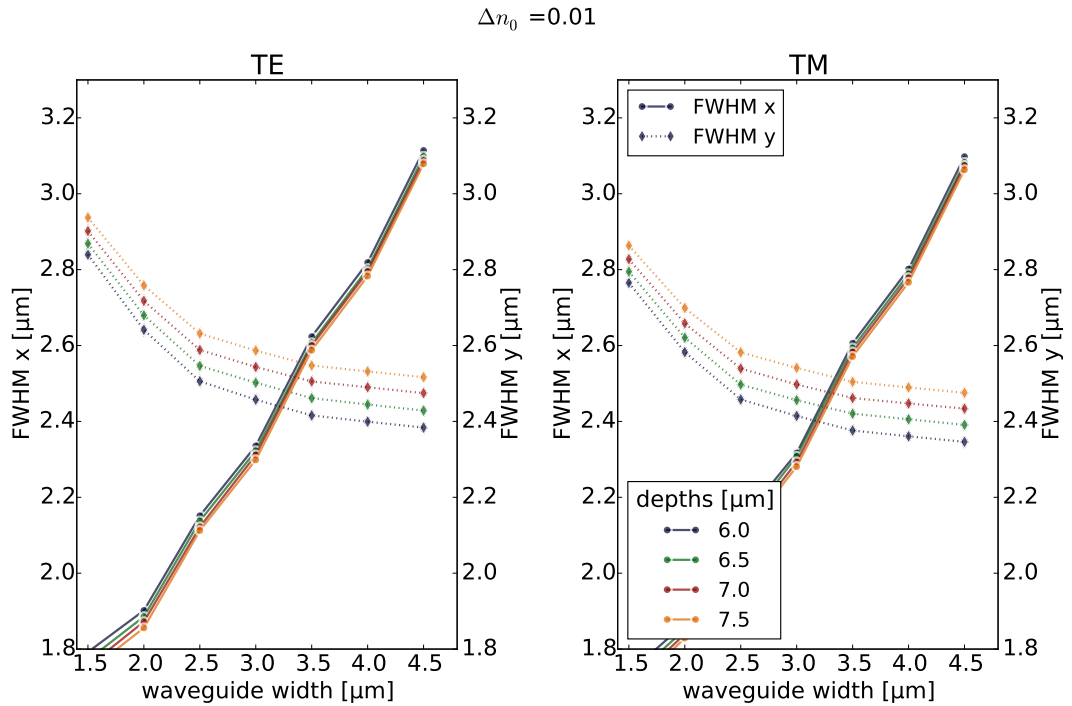


Figure 8.10 – FWHM of the simulated modes in lateral and vertical directions for an refractive index increase of $\Delta n_0 = 0.010$. The waveguide width w and the exchange depth d are varied.

Moreover, it can be noted that the FWHM in x-direction depends on the width and is independent from the exchange depth d , while the FWHM in y-direction is mainly dependent on the exchange depth d . In comparison to the ridge waveguides, the channel waveguides show a stronger dependency of the mode diameter (FWHM) in the x-direction than on the waveguide width. In smaller waveguides, the mode diameter increases, which can be an indicator for being in cut-off. Using these parameters, the fabrication of single-mode waveguides at 800 nm should be possible. In the next section, we explain the waveguide fabrication including the periodic poling and the rubidium exchange.

8.3.2 Channel Waveguide Fabrication

We fabricated channel waveguides in KTP samples with dimensions of $10 \times 6 \times 1 \text{ mm}^3$ along the crystallographic a-axis. These samples are immersed in the KNO_3 melt to homogenise the sample composition to improve the exchange and poling homogeneity (compare to section 6.2.3.1). We chose to periodically pole the KTP substrates first, and fabricated the waveguides in a subsequent step. Before preparing the samples, we polished the end facets of the samples to achieve a high signal-to-noise ratio in the optical monitoring signal. To improve the homogeneity of the photo resist layer, we had to use the double lithography technique as explained in section 6.2.2.1. We observed a shift of the phase matching to shorter wavelengths compared to the prediction of the dispersive model in ridge waveguides. Thus, the poling periods vary from $8.2 \text{ }\mu\text{m}$ to $8.6 \text{ }\mu\text{m}$ to shift the phase matching to longer wavelengths (compare to section 8.3.3.3). The samples had a Au/Pd metal contact on both sides (+c and -c) to increase the electrical contact over the whole sample. The liquid electrode sample holder (see section 6.2.2.3) was used in combination with an electrolyte of 1% KCl, 10% isopropyl alcohol and 89% H_2O . We applied five high voltage pulses of 2.7 kV/mm to invert the spontaneous polarisation. To control the poling progress, we used the in-situ monitoring technique (compare to section 6.1.1.2). After successful poling, we removed the metal electrodes and photo resist in an ammonia solution. This solution acts also as a weak selective etchant to visualise the domain structure, see figure 8.11.

We fabricated rubidium exchanged waveguides in the poled material. The exchange was done in the fabrication sequence explained in section 6.2.3.3 at a temperature of $331 \text{ }^\circ\text{C}$ for 5 minutes. For a reduction of the annealing effect during the removal of the sample from the crucible, we lifted the sample in one step up to the upper edge of the crucible. The temperature gradient is roughly $20 \frac{^\circ\text{C}}{\text{min}}$, which is a relatively large gradient, that could potentially lead to samples breaking. After the exchange, the sample surface has to be cleaned to remove residual salt and the titanium mask from the surface. To protect the surface for the following polishing step, we deposited a 200 nm layer of SiO_2 on top of the waveguides. The polishing of the end facets was performed with an additional photoresist layer between the SiO_2 protection layer and the second sample (details about the polishing process can be found in section 6.2.4.2). We measured the exchange depth of the waveguides by EDX spectroscopy. A comparison of channel waveguides exchanged at $330 \text{ }^\circ\text{C}$ for 5 min and 60 min are shown in figure 8.12.

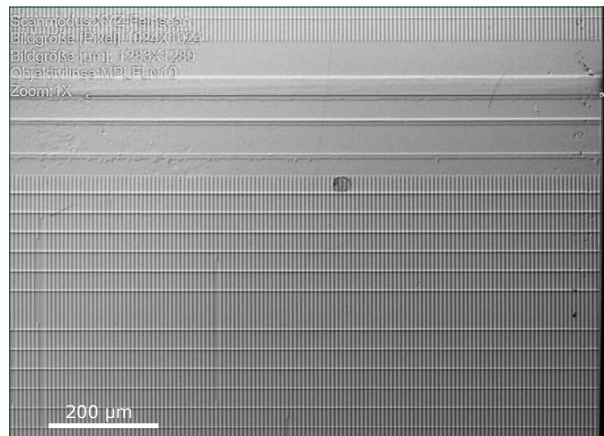


Figure 8.11 – Selectively etched surface of a periodically poled KTP sample. On the top the control section is shown (compare to region C in figure 6.13). In the horizontal direction, one group of 1.5 μm to 4.5 μm (from top to bottom) wide waveguides can be seen.

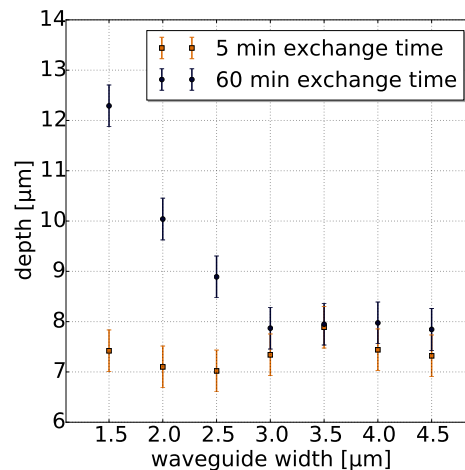


Figure 8.12 – EDX measurements of the exchange depth of channel waveguides at 330 $^{\circ}\text{C}$ for exchange times of 5 min and 60 min.

Surprisingly, the effect of varying exchange depths at different waveguide widths, which we see after a 60 min exchange (see section 6.3.3.3) is not observable after 5 min exchange. One explanation could be a clogging of the one-dimensional channels by rubidium ions near the surface, which circumvent a further exchange in the depth. However, this offers the possibility to optimise the mode profile with respect to the symmetry in an easy way, by varying the waveguide width. In the next section, we analyse the optical properties of the 5 min exchanged waveguides.

8.3.3 Optical Characterisation of Channel Waveguides

In this section, we characterise the linear and nonlinear optical properties of the 5 min exchanged waveguides. We start with a linear loss characterisation and the analysis of the mode profile. In the second part, we concentrate on the nonlinear characterisation by SHG and PDC. For all optical characterisations, we used a similar optical setup, which is shown in figure 8.13.

As a light source, we used a cw Ti-sapphire laser (M2 SolsTis) for measurements between

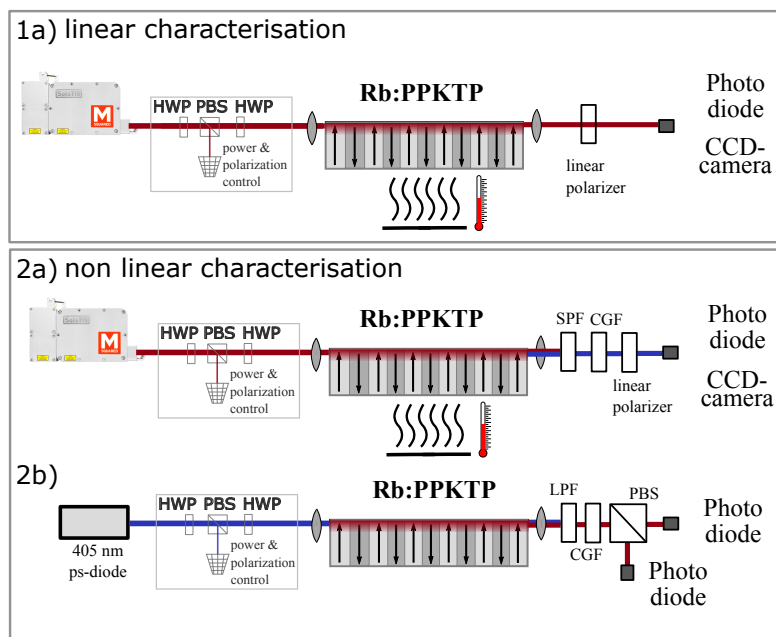


Figure 8.13 – Optical setup to investigate the optical properties of the channel waveguides. The linear 1a) and the nonlinear characterisation setups 2a) are similar to the one used for ridge waveguide analysis. In figure 2b), we show the setup for PDC experiments. The incoupling lens is AR coated for 400 nm, while the outcoupling lens is AR coated for 700 nm-1000 nm. And additional PBS is used to split the orthogonally polarised PDC photons.

700 nm and 1000 nm and a picosecond pulsed laser diode at 405 nm (PicoQuant). Power and polarisation were controlled by a combination of a half-wave plate, a polarising beam splitter and an additional half-wave plate. The light is coupled to the waveguide via lens coupling. After the waveguide, we measure the modes at different wavelengths on a CCD camera. The transmitted power was detected on a photo diode. Different types of filters, like short-pass or long-pass filters and colour glass filters can be added to suppress the pump light and an additional linear polariser was used to determine the polarisation of the generated light.

8.3.3.1 Spatial Modes in Channel Waveguides

For the first optical characterisation, we measured the mode size of waveguides with slit widths between 1.5 μm and 4.5 μm width varying in steps of 0.5 μm . The waveguide end facets were imaged onto a CCD camera with an aspheric lens. The polarisation was chosen with a linear polariser and set by the half-wave plate before the waveguide. The residual mode images are shown in figure 8.15.

We fitted a Gaussian profile to the measured data in the width direction and a Hermite-Gaussian for the depth direction, due to the large index increase to air at the surface. For TE and TM polarisation we compared the mode size which can be found in figure 8.14.

It can be seen that for all modes the minimum of the mode size is at roughly 3 μm waveguide width. For broader waveguides we saw an increase in the mode size. However, also for smaller widths we observed an increase of the mode size. This effect can be explained by going into cut-off in smaller waveguides. In addition to the mode shape, we calculate the field overlap and the coupling efficiency into a single-mode fibre (Type S630-HP, Thorlabs) with a mode field diameter of 4.2 μm . We calculated a field overlap of 95.7% and a theoretical coupling efficiency of up to 92% for a 3 μm wide waveguide. Beside the spatial modes, which define the overlap integral, we are interested in the transmission losses of the waveguides, which we analyse in the next section.

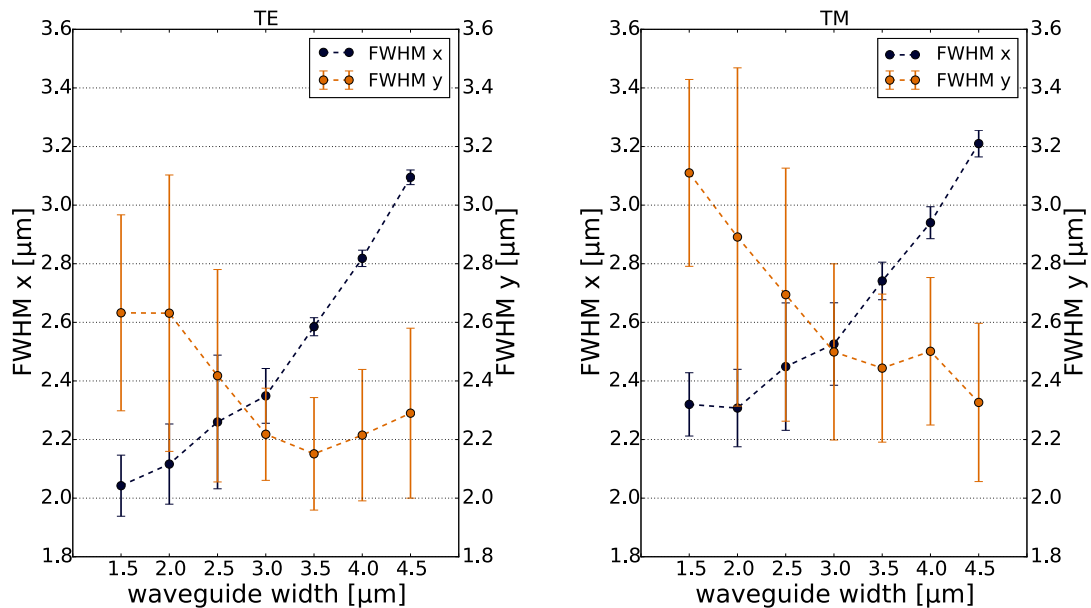


Figure 8.14 – Measurements of the FWHM in lateral and vertical direction for TE and TM polarisation depending on the waveguide width.

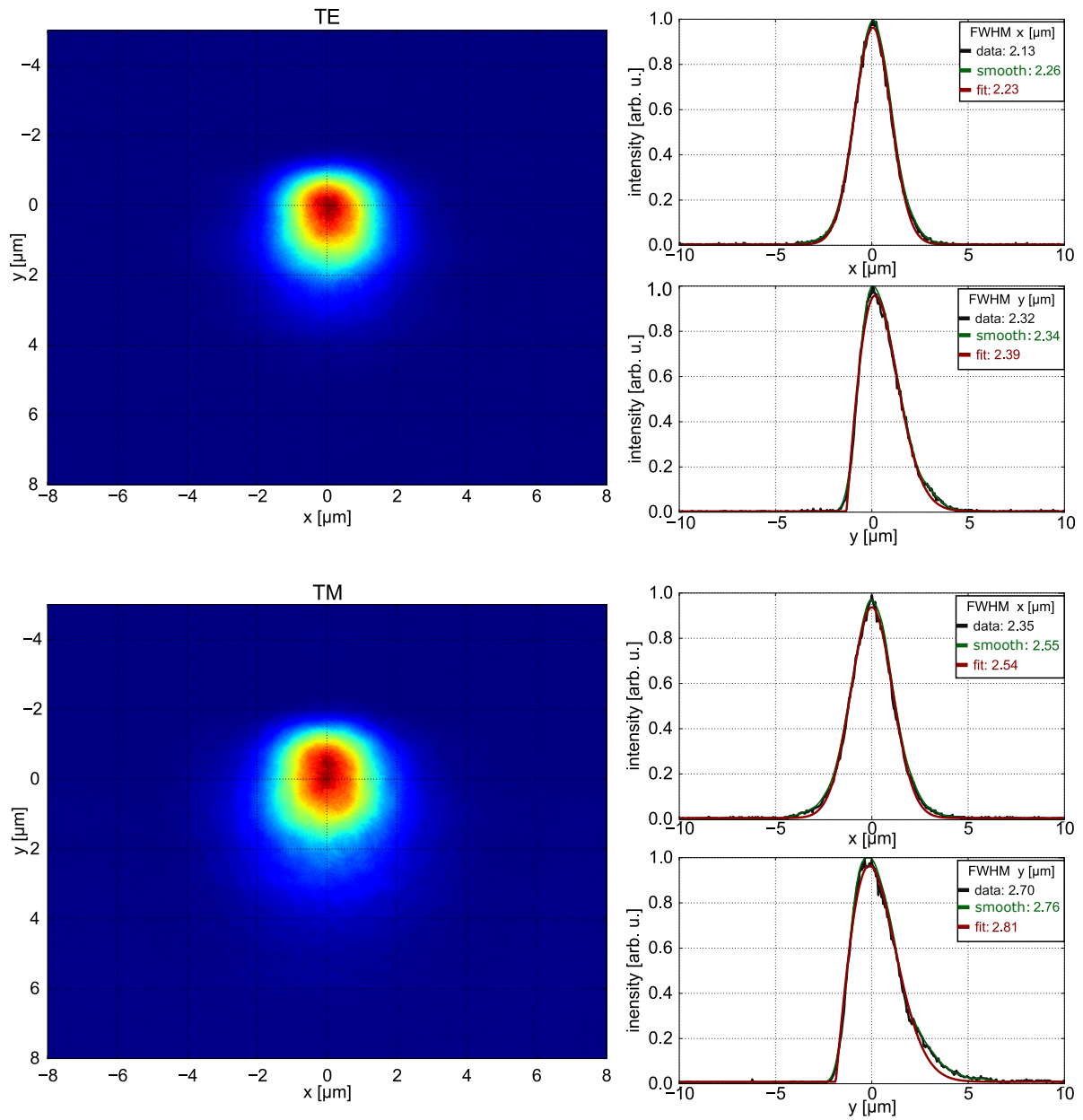


Figure 8.15 – Experimentally measured near field of the spatial modes at 800 nm for TE and TM polarisation. On the right hand side, we plot an x- and y-cut, passing through the peak. The mode symmetry in the lateral and vertical directions are calculated for raw, smoothed (averaged over 4 data-points) and fit data. For the lateral direction we fit a Gaussian and in the vertical direction a Hermite-Gaussian function.

8.3.3.2 Transmission Losses in Channel Waveguides

We measured the losses of KTP waveguides at a wavelength of 888 nm, using the Fabry-Perot method [157]. We realised the scanning of the resonator length by varying the sample temperature between 20 °C and 60 °C. From the contrast of the Fabry-Perot oscillations, we calculated the transmission losses of our waveguides. We could achieve attenuation coefficients of $1.3 \frac{\text{dB}}{\text{cm}}$ ($1.5 \frac{\text{dB}}{\text{cm}}$) for TE (TM) polarisation in 10 mm-long samples (see figure 8.16). These propagation losses are comparable to losses obtained for periodically poled samples at 1550 nm.

It has to be noted, that such low losses could be achieved only in samples with an additional SiO₂ protection layer on top of the sample. Typical losses without such a protection layer were around $3 \frac{\text{dB}}{\text{cm}}$ to $5 \frac{\text{dB}}{\text{cm}}$ (compare to section 6.2.4.2). After the linear characterisation, we performed the nonlinear optical characterisation by estimating the phase matching spectrum for a type-II process.

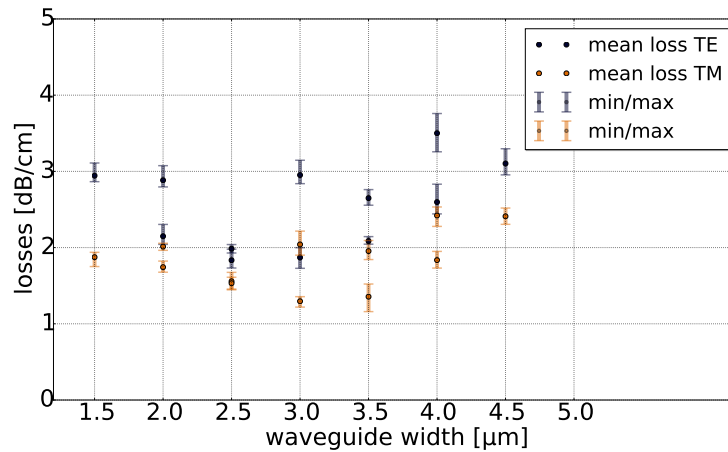


Figure 8.16 – Loss measurements in channel waveguides for different waveguide widths in several groups of the sample. The dots indicate the mean value for the losses, the error bar corresponds to the minimum and maximum value of the measured losses for each waveguide width.

8.3.3.3 Phase Matching in Channel Waveguides

Like we had observed the phase matching shift in ridge waveguides, the poling period in channel waveguides was shifted to longer poling periods of $\Lambda = 8.56 \mu\text{m}$. We use the same equations as in the ridge waveguide calculations in section 8.2.4.3. As seen in figure 8.17, the models predict SHG at 395 nm (for the bulk) and 412 nm (for the waveguide model). As we will show in section 8.3.3.4, the measured wavelength is 401 nm, which is marked by the blue cross in figure 8.17. We added the phase matching wavelength obtained in the PDC section to the plot (see red cross in figure 8.17). As in the ridge waveguide section, we used a dispersionless refractive index increase Δn_0 , that provides the best match of the phase matching curves in red in figure 8.17.

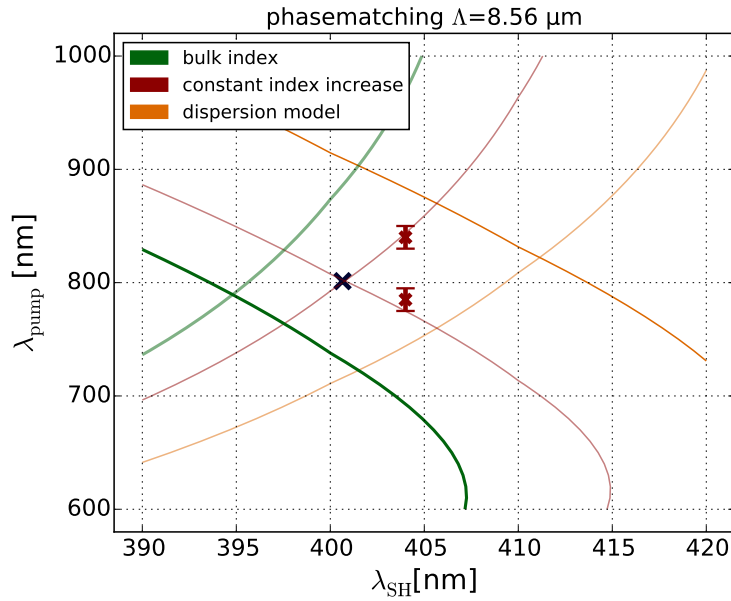


Figure 8.17 – Calculated phase matching function for bulk KTP [104] (green line), bulk index with constant index increase of $\Delta n_0 = 0.011$ (red line), and for the dispersion model [105] (orange line).

8.3.3.4 Second Harmonic Generation in Channel Waveguides

We used waveguides with poling periods of $8.56 \mu\text{m}$ and $8.64 \mu\text{m}$ and widths of $1.5 - 4.5 \mu\text{m}$ to measure the second-harmonic generations response. Linearly polarised light from a cw Ti-sapphire laser (M2 SolsTis) at 800 nm with a rotation of 45° with respect to the c-axis is coupled to the channel waveguide via lens coupling (compare to figure 8.13). Power and polarisation were controlled with a half-wave plate, a polarising beam splitter and an additional half-wave plate. In the waveguide, horizontally-polarised light was generated in a type-II phase-matched process at half of the pump wavelength. After the waveguide, we used a short-pass and a colour glass filter to suppress the pump light. We used a power meter to measure the generated SH power as a function of the pump wavelength. A measured phase matching spectrum is shown in figure 8.18.

Two peaks can be clearly identified. The pump beam is guided only in the fundamental mode because of the single-mode guiding properties; for the second harmonic light higher order modes can appear. We measured the second harmonic modes depending on the pump wavelength (see figure 8.18 inset).

Measurements essentially showed the expected sinc-function, with superimposed Fabry-Perot type oscillations (compare to figure 8.19a)). We attribute deviations from the envelope sinc function to inhomogeneities in the poling and the waveguide itself. The spectrum in figure 8.19a) shows fast oscillations arising from resonances within our setup.

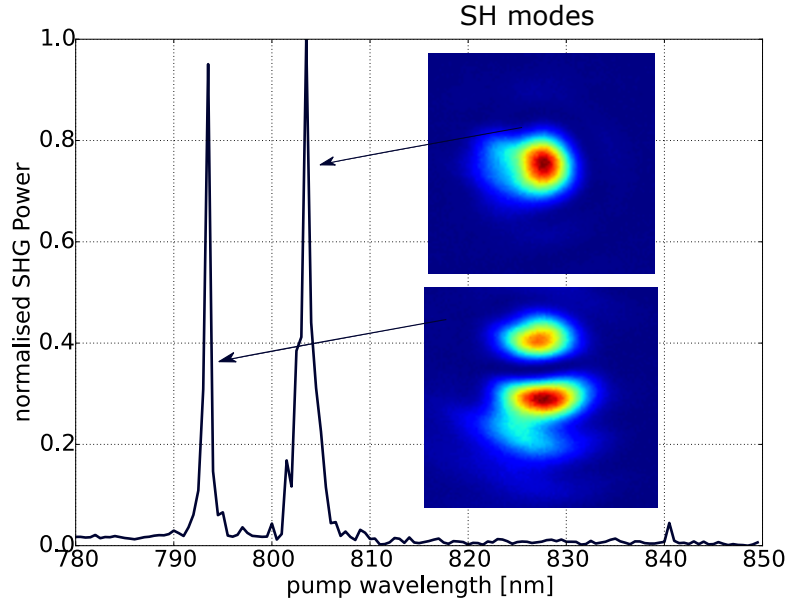


Figure 8.18 – Second harmonic spectrum with two different SH modes. The pump light remains in the fundamental mode due to the single-modeness of the waveguide.

The inset of figure 8.19a) shows the expected quadratic power dependency of the phase matched process. It has to be noted that we are using the refractive index increase at the surface of the waveguide Δn_0 , for the bandwidth calculation. We calculated the bandwidth comparable to the ridge waveguide and obtained the best fit for an effective length of 10 mm (compare to figure 8.19a), red line). The discrepancy to a calculated curve for the actual poling length of $l = 14$ mm (see figure 8.19a), green dashed line) can be explained by inhomogeneous poling and variation of the exchange profile along the waveguide.

The SHG efficiency was calculated as

$$\eta_{\text{exp}} = \frac{P_{\text{SHG}}}{P_{\text{pump}}^2 \cdot l^2} \cdot 100\% = 2.3 \frac{\%}{\text{W} \cdot \text{cm}^2}, \quad (8.10)$$

where P_{SHG} is the second harmonic (SH) power, P_{pump} is the pump power and l is the length of the poled fraction of the crystal. The efficiency was corrected for end facet reflection losses and transmission losses of the two coloured glass filters ($T=0.80$). The highest conversion efficiency of $\eta_{\text{exp}} = 2.3 \frac{\%}{\text{W} \cdot \text{cm}^2}$ was found for a $2.5 \mu\text{m}$ wide waveguide of length $l = 10$ mm, a poling period of $8.64 \mu\text{m}$, a pump wavelength of 801.3 nm and a pump power of 245 mW, resulting in a second harmonic power of $36 \mu\text{W}$. The pump power was corrected for end facet reflection losses, transmission losses ($1.8 \frac{\text{dB}}{\text{cm}}$ for a 14 mm long waveguide), and a coupling efficiency of 34% . The coupling efficiency was calculated from the maximum through coupled power corrected for Fresnel reflections and transmission losses (compare to section 8.3.3.2).

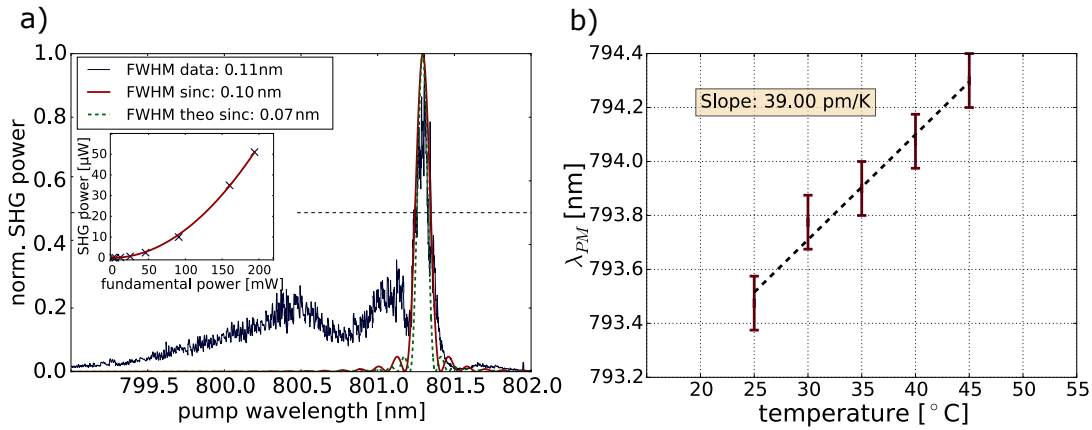


Figure 8.19 – a) Measured (blue) and calculated (red) phase matching curve of a 3.0 μm wide and 10 mm long channel waveguide for type-II conversion; the calculated curve (green) corresponds to a poling length equal to the sample length of 12 mm. b) Temperature dependence of the phase matching.

We also determined the theoretically expected efficiency comparably to the ridge waveguides (see section 8.2.4.4). The obtained value of the overlap integral is $S = 0.25 \mu\text{m}^{-1}$ for channel waveguides and was used to calculate a theoretically expected efficiency of

$$\eta_{\text{theo}} = \frac{8\pi^2 d_{\text{QPM}}^2 S^2}{n^3 c \epsilon_0 \lambda_{\text{pump}}^2} = 6.8 \frac{\%}{\text{W} \cdot \text{cm}^2}. \quad (8.11)$$

The deviation by a factor of 3 between experimental and theoretical efficiency is expected to be caused partially by waveguide losses, which arise especially for the SH modes, and eventually by inaccuracy of the mode overlap calculation.

We measured the temperature dependence of the phase matching to be 39 pm/K in a range from 25 °C to 45 °C (see figure 8.19b), which is in good agreement with temperature dependent phase matching measurements in PPKTP bulk crystals (60 pm/K) [158]. The device showed temperature insensitive behaviour which allows stable operation, independent of the ambient conditions.

8.3.3.5 Parametric Down Conversion in Channel Waveguides

In addition to the second harmonic generation, we performed measurements on parametric down conversion for a type-II photon pair generation with orthogonally polarised photons. We used a pico-second pulsed laser diode (Picoquant LDH-P-C-400B) at 405 nm to pump the waveguide. The setup is shown in figure 8.132b). The power and polarisation are controlled by a half-wave plate, a polarising beam splitter and an additional half-wave plate. The light is coupled into the waveguide via lens coupling ($f=4.5$ mm). The pump light is blocked by a colour glass filter and a long-pass filter, while the PDC photon pair is split up on a polarising beam splitter and measured either on a spectrometer (Andor iKon-M SR-303i-A), or on single photon detectors

(PerkinElmer SPCM-AQR-13FC). Figure 8.20 shows the spectrum for different pump mode combinations. The generated PDC photons are in the fundamental mode, which narrows the bandwidth in comparison to multi-mode waveguides [40].

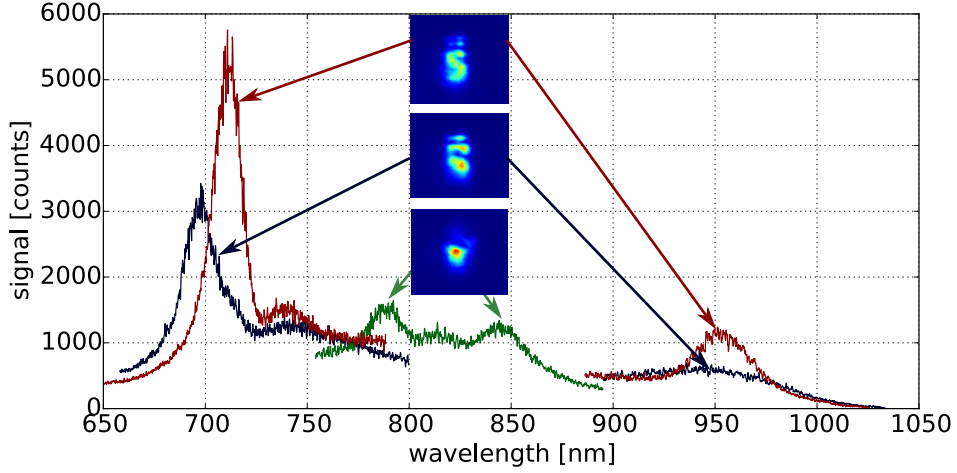


Figure 8.20 – Measured PDC spectra for different pump mode combinations. The spatial mode images for the 405 nm mode are shown in the insets.

By usage of the single photon detectors, we measured the Klyshko efficiencies to be 8.6% and 7.2% for signal and idler photons, respectively. The Klyshko efficiency can be calculated as

$$\eta_{\text{signal}} = \frac{\text{coincidence rate}}{\text{idler rate}} \quad (8.12)$$

and

$$\eta_{\text{idler}} = \frac{\text{coincidence rate}}{\text{signal rate}}. \quad (8.13)$$

These values are in a reasonable range due to the low detection efficiency of the detectors ($\eta_{\text{det signal}} < 65\%$ and $\eta_{\text{det idler}} < 25\%$) and the lossy optical filters ($> 50\%$). If we calculate an upper bound for the achievable maximum Klyshko efficiency, taking into account detector efficiencies ($\eta_{\text{det}} < 65\%$), waveguide losses (8%), end facet reflections (8.8%), losses in optical components (20%) and transmission losses in filters (55%), we estimated a maximum reachable value of 20% for idler and 9% for signal Klyshko efficiencies.

The achieved Klyshko efficiencies are comparable to values measured in multi-mode waveguides (9% [40] and 16.5% [163]), in which a much larger amount of filtering was necessary. The efficiencies in our waveguides can be easily improved by using nanowire detectors ($\eta > 90\%$) instead of APD detectors with low detection efficiency. Furthermore, the optimisation of bandpass filters to a higher transmission grade can lead to an improved Klyshko efficiency.

Finally, we measured the quantum character of our PDC photons by normalised correlation function measurements. In Particular, we demonstrate that the value of the $g^{(1,1)}$ cross-correlation function, which is a measure for the strength of the signal-idler photon number correlation, exceeds the classical limit. The $g^{(1,1)}$ function can be calculated from

$$g^{(1,1)} = \frac{\text{coincidence rate}}{\text{singal rate} \cdot \text{idler rate}} \cdot \text{trigger rate}. \quad (8.14)$$

For an exemplary measurement we find

$$g^{(1,1)} = \frac{151 \text{ Hz}}{2429 \text{ Hz} \cdot 1932 \text{ Hz}} \cdot 1 \text{ MHz} = 32 \pm 4 > 1 \text{ (classical bound)} \quad (8.15)$$

This result conclusively demonstrates that our source generates high-quality photon pairs, which can serve as basis for more advanced quantum applications such as entangled-state generation or quantum sensing protocols based on time-frequency correlated biphotons.

8.3.3.6 Channel Waveguide Summary

For the realisation of a single-mode converter, operating at 800 nm, we have fabricated periodically poled channel waveguides in c-cut KTP. The device shows relatively low transmission losses and symmetric mode profiles. Furthermore, we successfully demonstrated type-II second harmonic generation from 801.3 nm to 400.6 nm with normalised conversion efficiency of 2.3 %/W·cm². The measured bandwidth of 0.1 nm and the low temperature dependence of 39 pm/K pave the way for further exploration of a class of devices suitable for varying environments. First investigations on photon pair generations via PDC in periodically poled channel waveguides in KTP were successfully performed. Such c-cut channel waveguides are good candidates for highly-efficient nonlinear frequency conversion devices.

8.4 Application Discussion

Through applying the technology we introduced in chapter 6, we created two different types of devices to expand the applicability of KTP to NIR applications around 800 nm operating in a single-mode regime. We successfully demonstrated the application of a nonlinear conversion between UV and NIR wavelengths around 800 nm. A comparison of normalised efficiencies with previous demonstrations of SHG in PPKTP waveguides is shown in table 8.5.

Our ridge waveguides show the highest conversion efficiency for such type of conversion in PPKTP structures due to the larger overlap integral compared to channel waveguides. As already discussed in the technology section, the erasing of the domains during the rubidium exchange probably reduces the efficiency dramatically. We reduced the waveguide losses by a factor of 5 to 10 over the last year. A further improvement can be achieved by optimising the polishing procedure, especially in the ridge structure.

Table 8.5 – Comparison of efficiencies for periodically poled bulk or waveguides in KTP.

	material	type	pump	second harmonic wavelength [nm]	efficiency
1	this work ridge waveguides [4]	II	cw	396.1	6.6 %/W·cm ²
2	this work channel waveguides	II	cw	400.6	2.3 %/W·cm ²
3	laser written waveguides in PPKTP [164]	II	cw	471	4.6 %/W·cm ²
4	PPKTP wg [165]	II	pulsed	398.3	4.78 %/W·cm ²
5	bulk KTP [166]	II	pulsed	398	1.79 %/W·cm
6	segmented KTP waveguides [121]	I	cw	425	122 %/W·cm ²

The waveguide rubidium exchange is still not fully understood and needs to be investigated in more detail. The exchange depth seems to be the same in 5 min and 60 min exchanged waveguides, which could be an indication for a surface-near crystallographic modification, e.g. induced by the surface polishing. This has to be investigated by crystal structure analysis methods, i.e. atomic force microscopy, scanning tunnelling microscopy, X-ray diffractometry, or X-ray reflectometry. Various sum-frequency generation measurements for different poling periods and processes can help to build a more precise model to adapt this kind of waveguides to other wavelengths and applications.

However, this represents only small challenges on the way to more complex applications. We succeeded in adapting a working KTP technology to gain new kinds of applications in KTP.

Summary

In this chapter, we demonstrated the highly interesting application of UV-NIR wavelength conversion, for which KTP is the material of choice. We fabricated single-mode waveguides at 800 nm in ridge and channel configuration and characterised the linear and nonlinear properties. Both devices show symmetric mode profiles and have low losses, which can be as low as $1.3 \frac{\text{dB}}{\text{cm}}$. Both show high nonlinear conversion efficiencies up to $\eta = 6.6 \frac{\%}{\text{W}\cdot\text{cm}^2}$. Additionally, we characterised the channel waveguides with respect to photon pair generation via a PDC process and reached Klyshko efficiencies up to 8.6%.

Summary and Outlook

9.1 Summary

This thesis gave us the possibility to investigate the material platform of potassium titanyl phosphate to pave a way towards novel integrated and quantum optical applications. Integrated optical devices comprise several functional components that are interconnected by waveguides; they offer various functionalities such as amplitude and phase modulation, frequency and polarisation conversion, lasing, and photo detection. The development of new devices for integrated applications was the driving force behind investigating a technology for the fabrication of integrated structures in KTP. The three parts of the thesis represent the KTP technology, the coating facility and the demonstration of an application, in which we convert light in single-mode waveguides from 800 nm into the UV regime.

In the framework of technology, we gave an overview over the current state-of-the-art in fabricating periodically poled waveguides in KTP and explained our solutions to overcome challenges combining rubidium exchanged waveguide structures and a periodic poling. The first experiments on this material platform brought a deeper understanding of the material properties and its poling behaviour. We investigated two different fabrication sequences, namely the poling of Rb-exchanged waveguides and the diffusion of Rb into periodically poled substrates. We critically compared our results for both techniques and identified the fabrication of waveguides in previously poled material as the most promising way towards achieving periodically poled waveguides in KTP.

The coating part gave insight into dielectric coating techniques and their advantages for integrated optical devices. We presented the basic concepts underlying dielectric coatings, and elucidated our design procedure and fabrication. We described our coating facility, being based on IAD techniques, which, when combined with our broadband monitoring system, offers the possibility to realise tailored dielectric coatings. Such coatings improved the performance of different kinds of devices and modules and allowed us to investigate new kinds of coating designs and compositions. Using this technology, we fabricated different types of devices, e.g. resonators [45, 46] and photon pair sources [31, 41]. We gave an overview about the performance of selected dielectric coatings that we realised, mainly established on the LN platform. Further, we described our approach towards new coating designs in combination with an optimised deposition process. The idea of wavelength dependent coatings, which allows the wavelength dependent manipulation of transmission, phase or group delay dispersion without the drawback

of varying beam displacement as well as the grid-less spectrometer using a gradient needle filter coating were demonstrated and an invention disclosure is submitted.

In the applications part of the thesis, we showed two different realisations of a frequency converter. For both devices we started with theoretical calculations of the expected spatial mode profiles, to minimize the parameter range for single-mode guiding in the NIR regime and know the expected poling period. We fabricated ridge waveguides, guiding only one single spatial mode around 800 nm and poled them with a period of 7.35 μm , which provides quasi-phase matching for a type-II frequency conversion from 796 nm to 398 nm. These devices are the first periodically poled and NIR single-mode ridge waveguides in KTP. We measured a conversion efficiency of $6.6 \frac{\%}{\text{W}\cdot\text{cm}^2}$, which is in a good agreement with theoretical expectations. The second device is geared towards the same application, but is based upon different fabrication techniques. We realised NIR single-mode, rubidium-exchanged, periodically poled channel waveguides as a new kind of nonlinear device in KTP. We succeeded in fabricating waveguides that guide light with a symmetric mode shape in the fundamental mode. The optimised polishing technique, using an SiO_2 and a photo resist protection layer, yields losses as low as $1.3 \frac{\text{dB}}{\text{cm}}$. Further, we characterised the nonlinear properties, performing second harmonic generation experiments from 801.5 nm to 400.5 nm with an efficiency of $2.3 \frac{\%}{\text{W}\cdot\text{cm}^2}$.

In conclusion, we developed and established a technology, which facilitates the fabrication of periodically poled waveguide structures in KTP during this thesis. We gained a profound understanding of the material properties and the diffusion and domain inversion processes. We developed new techniques to periodically pole KTP structures, thereby generating intellectual property, filed patents for the underlying ideas and procedures [142]. In addition to KTP technology, we set up a coating facility that has enhanced the performance of integrated optical devices and produced tailored dielectric coatings for LN and KTP devices, as well as dielectric filters and mirrors on glass substrates. We then made use of our new technology to fabricate different tailored single-mode waveguides in KTP that served as frequency converters connecting NIR and UV wavelengths [4].

9.2 Outlook

Applying the insights gained and techniques developed during this thesis, yields new possibilities for future applications. During this thesis we have encountered a challenge connected to the high conductivity of pure KTP. This was a limiting factor for poling waveguide structures. Also, the electric field distribution in the inhomogeneous material mixture of rubidium exchanged and pure KTP complicates the understanding and forecast of poling dynamics in different samples. Using a relatively new substrate material, containing a small amount of rubidium ($\frac{\text{Rb}}{\text{K}} < 1\%$), we were able to equalize the strong variations and render the fabrication process more reliable and predictable. However, nevertheless new challenges will arise in the novel material. The increased coercive field strength adds technical complexity to the poling process, especially to the shielding to prevent arcs. Furthermore, the diffusion process, with all of its optimised parameters, has to be adapted and optimised for the new material platform. In this material, the direct poling of waveguide structures is a promising approach, which can be further optimised by expanding the optical monitoring developed during this work to wavelength regions in which

a single-mode guiding is possible. This promises an increased degree of control over the poling dynamics and a better understanding of the poling process. The optical monitoring can also be interesting for other materials.

During the final year of this thesis, a novel material platform became available: thin-film potassium titanyl phosphate or KTP on insulator (KTPOI). This material belongs to the material family of thin films e.g. SOI (silicon on insulator) or LNOI (lithium niobate on insulator) and is an emerging research field [167, 168]. Such thin film devices provides a much larger refractive index increase compared to indiffused or exchanged waveguides and promises a significant increase in mode overlap between different fields, as well as single-mode guiding over a large wavelength range. This enables frequency conversion processes in which all involved fields propagate in the fundamental spatial waveguide mode, leading to an increase in conversion efficiency. In addition, owing to the large index difference, minimum feature sizes can be decreased, which facilitates a tremendous increase in packing density. First investigations on realising waveguide structures have been conducted, but the resulting devices were of limited applicability since they relied on birefringent phase matching. By adapting our knowledge and our poling technology to this new material, it would be possible to open the field to new wavelength combinations, in particular in the visible and UV range. Especially, optical monitoring in waveguides has the potential to solve the technological problem of monitoring the poling dynamics in thin films.

A hybrid approach combining silicon photonics, whereas a wafer-scale technology compatible with the semiconductor industry for the fabrication is available with the advantages of KTP thin films predicts an applicability for integrated optical computer and ultra-high bandwidth electro optical modulators for the next generation of systems on chip.

Acknowledgements

I have had the possibility to spend a large amount of time on developing the technology to bring a truly fascinating material from a raw substrate to an application. This was possible thanks to the support of my supervisor Professor Christine Silberhorn, who believed in my abilities. Her guidance and her advice over the many years since I joined her group as a student helper have been invaluable.

I would also like to thank Professor Artur Zrenner for acting as second reviewer.

Next, I would like to highlight two people without whom this work would not have been possible. Raimund Ricken, who assisted in a considerable part of the sample preparation; and Victor Quiring, with whom I spent a large part of my time setting up the excellent coating facility.

Many thanks to my colleagues Laura Padberg, Matteo Santandrea, Felix vom Bruch, Helge Rütz and Sebastian Lengeling for the many years of working together in the area of technology. Each of them helped and supported me with their respective expertise and strengths.

In addition to the technology, I was also able to get to know the field of optical characterisation. I was always able to rely on the support of my colleagues Vahid Ansari, Regina Kruse, Matteo Santandrea and Michael Stefszky. Thanks to you, I understood an exciting, but at the same time, very complex subject area in a short time.

On to two persons, whose long-standing experience and deep knowledge contributed significantly to my work. Hubertus Suche and Harald Herrmann, who answered all questions at any time and helped me with fruitful ideas.

It is an honour for me to know Benjamin Brecht and to have had the opportunity to work with him. With his ideas and support, I was able to grow beyond myself. Thank you for your help and your tireless explanations.

Many thanks to my proofreaders Tim Bartley, Benjamin Brecht, Michael Stefszky, Evan Meyer-Scott, Laura Padberg, Matteo Santandrea and Felix vom Bruch, for their tireless reading and their very helpful correctionssss and suggestions.

A huge thank you goes to all other colleagues Markus Allgaier, Sonja Barkhofen, Tim Bartley, Sebastian Brauner, Andreas Christ, Melanie Engelkemeier, Georg Harder, Stephan Krapick, Jano Lopez, Kai Hong Luo, Marcello Massaro, Nicola Montaut, Thomas Nitsche, Linda Sansoni and Johannes Tiedau for the outstanding working atmosphere. They always provide a helpful hand and a good advice

Two people have contributed to this work in a special way. Many thanks to Rita Prevor, without you I would be completely lost in the maze that is administration.

Simone Schmücker always supported me. She always gave me new courage when I was feeling low, and kept pushing me on to new heights.

Last but not least I want to thank all members of my family. Thank you for giving me the opportunity to study physics and the support during that time.

A

Appendix

A.1 Patents

(1) Herstellung von Wellenleitern aus Materialien der KTP-Familie

Christof Eigner, Matteo Santandrea, Laura Padberg und Christine Silberhorn
Az. 10 2018 108 636.9. (2018)

(2) Gradientenfilter zur strahlversatzfreien, wellenlängenselektiven Modifikation der Lichteigenschaften

Christof Eigner, Laura Padberg, Viktor Quiring, Johannes Tiedau und Christine Silberhorn
Erfindungsmeldung eingereicht (2018)

(3) Prototyp eines gitterlosen, justagefreien Spektrometers

Christof Eigner, Benjamin Brecht, Laura Padberg, Viktor Quiring und Christine Silberhorn
Erfindungsmeldung eingereicht (2018)

A.2 Publications

(1) Nonlinear integrated quantum electro-optic circuits

Kai-Hong Luo, Sebastian Brauner, Christof Eigner, Polina R. Sharapova, Raimund Ricken, Torsten Meier, Harald Herrmann, Christine Silberhorn
Science Advances 5, 1451 (2019)

(2) Periodically poled ridge waveguides in KTP for second harmonic generation in the UV regime

Christof Eigner, Matteo Santandrea, Laura Padberg, Martin F. Volk, Christian E. Rüter, Harald Herrmann, Detlef Kip, and Christine Silberhorn
Opt. Express 26(22), 28827-28833 (2018)

- (3) High-performance source of indistinguishable entangled photon pairs based on hybrid integrated-bulk optics**
Evan Meyer-Scott, Nidhin Prasannan, Christof Eigner, Viktor Quiring, John M. Donohue, Sonja Barkhofen, Christine Silberhorn
Opt. Express 26(25), 32475-32490 (2018)
- (4) High-power waveguide resonator second harmonic device with external conversion efficiency up to 75%**
M. Stefszky, R. Ricken, C. Eigner, V. Quiring, H. Herrmann, C. Silberhorn
J. Opt. 20, 065501 (2018)
- (5) Heralded generation of high-purity ultrashort single photons in programmable temporal shapes**
Vahid Ansari, Emanuele Rocchia, Matteo Santandrea, Mahnaz Doostdar Kejdehi, Christof Eigner, Laura Padberg, Ilaria Gianani, Marco Sbroscia, John M. Donohue, Luca Mancino, Marco Barbieri, Christine Silberhorn
Opt. Express 26(3), 2764-2774 (2018)
- (6) Streak camera imaging of single photons at telecom wavelength**
Markus Allgaier, Vahid Ansari, Christof Eigner, Viktor Quiring, Raimund Ricken, John Matthew Donohue, Thomas Czerniuk, Marc Aßmann, Manfred Bayer, Benjamin Brecht, Christine Silberhorn
Appl. Phys. Lett. 112, 031110 (2018)
- (7) Fabrication of low-loss Rb-exchanged ridge waveguides in z-cut KTiOPO₄**
Martin F. Volk, Christian E. Rüter, Matteo Santandrea, Christof Eigner, Laura Padberg, Harald Herrmann, Christine Silberhorn, and Detlef Kip
Opt. Mater. Express 8(1), 82-87 (2018)
- (8) Fast time-domain measurements on telecom single photons**
Markus Allgaier, Gesche Vigh, Vahid Ansari, Christof Eigner, Viktor Quiring, Raimund Ricken, Benjamin Brecht, and Christine Silberhorn
Quantum Sci. Technol. 2, 034012 (2018)
- (9) Waveguide Cavity Resonator as a Source of Optical Squeezing**
M. Stefszky, R. Ricken, C. Eigner, V. Quiring, H. Herrmann, and C. Silberhorn
Phys. Rev. Applied 7, 044026 (2018)
- (10) Imaging of 180° ferroelectric domain walls in uniaxial ferroelectrics by confocal Raman spectroscopy: Unraveling the contrast mechanism**
M Rüsing, S Neufeld, J Brockmeier, C Eigner, P Mackwitz, K Spychala, C Silberhorn, W G Schmidt, G Berth, A Zrenner, S Sanna
Physical Review Materials 2 (10), 103801 (2018)
- (11) A two-channel, spectrally degenerate polarization entangled source on chip**
Linda Sansoni, Kai Hong Luo, Christof Eigner, Raimund Ricken, Viktor Quiring, Harald Herrmann and Christine Silberhorn
Quantum Information 3, 5 (2017)

(12) Highly efficient frequency conversion with bandwidth compression of quantum light

Markus Allgaier, Vahid Ansari, Linda Sansoni, Christof Eigner, Viktor Quiring, Raimund Ricken, Georg Harder, Benjamin Brecht and Christine Silberhorn
Nat. Commun. 8, 14288 (2017)

(13) Identification of ferroelectric domain structure sensitive phonon modes in potassium titanyl phosphate: A fundamental study

M. Rüsing, C. Eigner, P. Mackwitz, G. Berth, C. Silberhorn, A. Zrenner
J. Appl. Physics 119, 044103 (2016)

Preprints

(14) Pulse shaping using dispersion-engineered difference frequency generation

Markus Allgaier, Vahid Ansari, John Matthew Donohue, Christof Eigner, Viktor Quiring, Raimund Ricken, Benjamin Brecht, Christine Silberhorn
arxiv.org/abs/1812.07904

(15) Counter-propagating photon pair generation in a nonlinear waveguide

Kai-Hong Luo, Vahid Ansari, Marcello Massaro, Matteo Santandrea, Christof Eigner, Raimund Ricken, Harald Herrmann, Christine Silberhorn
in preparation (2019)

A.3 Conference Contributions

- ECIO, Valencia, 2018 *talk*
- DPG spring meeting, Erlangen, 2018 *talk*
- IQO² meeting, Bielefeld, 2018 *talk*

- Invited group seminar talk, Oxford (group of Prof. Ian Walmsley), 2017 *talk*
- Invited group seminar talk, Southampton (group of Prof. Peter Smith), 2017 *talk*
- Europhotonics, Barcelona, 2017 *poster*
- DPG spring meeting, Mainz, 2017 *poster*

- Europhotonics, Porquerolle, 2016 *poster*
- DPG spring meeting, Hannover, 2016 *poster*
- Heraeus Seminar, Bad Honnef, 2016 *poster*

- DPG spring meeting, Heidelberg, 2015 *talk*
- GRK convention, Paderborn, 2015 *talk*

- DPG spring meeting, Berlin, 2014 *poster*

- [1] M. Rüsing, S. Neufeld, J. Brockmeier, et al. “Imaging of 180° ferroelectric domain walls in uniaxial ferroelectrics by confocal Raman spectroscopy: Unraveling the contrast mechanism”. *Physical Review Materials* **2**, (2018).
- [2] M. Rüsing, C. Eigner, P. Mackwitz, et al. “Identification of ferroelectric domain structure sensitive phonon modes in potassium titanyl phosphate: A fundamental study”. *Journal of Applied Physics* **119**, 044103 (2016).
- [3] M. F. Volk, C. E. Rüter, M. Santandrea, et al. “Fabrication of low-loss Rb-exchanged ridge waveguides in z-cut KTiOPO₄”. *Optical Materials Express* **8**, 82 (2017).
- [4] C. Eigner, M. Santandrea, L. Padberg, et al. “Periodically poled ridge waveguides in KTP for second harmonic generation in the UV regime”. *Optics Express* **26**, 28827 (2018).
- [5] N. C. Harris, G. R. Steinbrecher, M. Prabhu, et al. “Quantum transport simulations in a programmable nanophotonic processor”. *Nature Photonics* **11**, 447–452 (2017).
- [6] P. Cheben, R. Halir, J. H. Schmid, H. A. Atwater, and D. R. Smith. “Subwavelength integrated photonics”. *Nature* **560**, 565–572 (2018).
- [7] K.-H. Luo, S. Brauner, C. Eigner, et al. “Nonlinear integrated quantum electro-optic circuits”. *Science Advances* **5**, eaat1451 (2019).
- [8] H. Rütz, K.-H. Luo, H. Suche, and C. Silberhorn. “Quantum Frequency Conversion between Infrared and Ultraviolet”. *Physical Review Applied* **7**, (2017).
- [9] M. Schwaerzle, K. Seidl, U. T. Schwarz, O. Paul, and P. Ruther. “Ultrapact optrode with integrated laser diode chips and SU-8 waveguides for optogenetic applications”. In: *2013 IEEE 26th International Conference on Micro Electro Mechanical Systems (MEMS)*. IEEE, 2013.
- [10] J. P. Sprengers, A. Gaggero, D. Sahin, et al. “Waveguide superconducting single-photon detectors for integrated quantum photonic circuits”. *Applied Physics Letters* **99**, 181110 (2011).
- [11] W. Sohler, H. Hu, R. Ricken, et al. “Integrated Optical Devices in Lithium Niobate”. *Optics and Photonics News* **19**, 24 (2008).
- [12] S. A. Maier. “Plasmonics: The Promise of Highly Integrated Optical Devices”. *IEEE Journal of Selected Topics in Quantum Electronics* **12**, 1671–1677 (2006).

- [13] R. Kaiser, H. Schroeter-Janßen, H. Heidrich, et al. “Monolithically integrated polarisation diversity heterodyne receivers on GaInAsP/InP”. *Electronics Letters* **30**, 1446–1447 (1994).
- [14] W. M. Green, M. J. Rooks, L. Sekaric, and Y. A. Vlasov. “Ultra-compact, low RF power, 10 Gb/s silicon Mach-Zehnder modulator”. *Optics Express* **15**, 17106 (2007).
- [15] G. Schreiber. “Quasi-phasenangepaßte Frequenzkonversion mit periodisch gepoltem Ti:LiNbO₃ Wellenleitern”. Phd. Thesis. Universität Paderborn, 2001.
- [16] L. Bi, J. Hu, P. Jiang, et al. “On-chip optical isolation in monolithically integrated non-reciprocal optical resonators”. *Nature Photonics* **5**, 758–762 (2011).
- [17] A. Orioux and E. Diamanti. “Recent advances on integrated quantum communications”. *Journal of Optics* **18**, 083002 (2016).
- [18] Y. Shen, N. C. Harris, S. Skirlo, et al. “Deep learning with coherent nanophotonic circuits”. *Nature Photonics* **11**, 441–446 (2017).
- [19] M. Cramer, M. B. Plenio, S. T. Flammia, et al. “Efficient quantum state tomography”. *Nature Communications* **1**, 149 (2010).
- [20] M. P. da Silva, O. Landon-Cardinal, and D. Poulin. “Practical Characterization of Quantum Devices without Tomography”. *Physical Review Letters* **107**, (2011).
- [21] T. D. Ladd, F. Jelezko, R. Laflamme, et al. “Quantum computers”. *Nature* **464**, 45–53 (2010).
- [22] N. Spagnolo, C. Vitelli, M. Bentivegna, et al. “Experimental validation of photonic boson sampling”. *Nature Photonics* **8**, 615–620 (2014).
- [23] S. Barz, J. F. Fitzsimons, E. Kashefi, and P. Walther. “Experimental verification of quantum computation”. *Nature Physics* **9**, 727–731 (2013).
- [24] J. Wang, S. Paesani, R. Santagati, et al. “Experimental quantum Hamiltonian learning”. *Nature Physics* **13**, 551–555 (2017).
- [25] S. Debnath, N. M. Linke, C. Figgatt, et al. “Demonstration of a small programmable quantum computer with atomic qubits”. *Nature* **536**, 63–66 (2016).
- [26] R. Barends, J. Kelly, A. Megrant, et al. “Superconducting quantum circuits at the surface code threshold for fault tolerance”. *Nature* **508**, 500–503 (2014).
- [27] B. J. Smith, P. Mahou, O. Cohen, J. S. Lundeen, and I. A. Walmsley. “Photon pair generation in birefringent optical fibers”. *Optics Express* **17**, 23589 (2009).
- [28] K. Wakui, H. Takahashi, A. Furusawa, and M. Sasaki. “Photon subtracted squeezed states generated with periodically poled KTiOPO₄”. *Optics Express* **15**, 3568 (2007).
- [29] S. Krapick, H. Herrmann, V. Quiring, et al. “An efficient integrated two-color source for heralded single photons”. *New Journal of Physics* **15**, 033010 (2013).
- [30] J. W. Silverstone, D. Bonneau, K. Ohira, et al. “On-chip quantum interference between silicon photon-pair sources”. *Nature Photonics* **8**, 104–108 (2013).

-
- [31] E. Meyer-Scott, N. Prasanna, C. Eigner, et al. “High-performance source of spectrally pure, polarization entangled photon pairs based on hybrid integrated-bulk optics”. *Optics Express* **26**, 32475 (2018).
- [32] Z. Yao, K. Wu, B. X. Tan, et al. “Integrated Silicon Photonic Microresonators: Emerging Technologies”. *IEEE Journal of Selected Topics in Quantum Electronics*, 1–1 (2018).
- [33] F. Nakamura, K. Muramatsu, K. Suzuki, et al. “Integrated silicon photonic wavelength-selective switch using wavefront control waveguides”. *Optics Express* **26**, 13573 (2018).
- [34] M. Lawrence. “Lithium niobate integrated optics”. *Reports on Progress in Physics* **56**, 363–429 (1993).
- [35] K. Kato. “Temperature insensitive SHG at 0.5321 μm in KTP”. *IEEE Journal of Quantum Electronics* **28**, 1974–1976 (1992).
- [36] G. Harder, V. Ansari, B. Brecht, et al. “An optimized photon pair source for quantum circuits”. *Optics Express* **21**, 13975 (2013).
- [37] V. Ansari, E. Roccia, M. Santandrea, et al. “Heralded generation of high-purity ultrashort single photons in programmable temporal shapes”. *Optics Express* **26**, 2764 (2018).
- [38] J. D. Bierlein and H. Vanherzeelen. “Potassium titanylphosphate: properties and new applications”. *Journal of the Optical Society of America B* **6**, 622 (1989).
- [39] H. Karlsson and F. Laurell. “Electric field poling of flux grown KTiOPO_4 ”. *Applied Physics Letters* **71**, 3474–3476 (1997).
- [40] K. Laiho, K. N. Cassemiro, and C. Silberhorn. “Producing high fidelity single photons with optimal brightness via waveguided parametric down-conversion”. *Optics Express* **17**, 22823 (2009).
- [41] L. Sansoni, K. H. Luo, C. Eigner, et al. “A two-channel, spectrally degenerate polarization entangled source on chip”. *npj Quantum Information* **3**, (2017).
- [42] M. Allgaier, V. Ansari, L. Sansoni, et al. “Highly efficient frequency conversion with bandwidth compression of quantum light”. *Nature Communications* **8**, 14288 (2017).
- [43] M. Allgaier, G. Vigh, V. Ansari, et al. “Fast time-domain measurements on telecom single photons”. *Quantum Science and Technology* **2**, 034012 (2017).
- [44] M. Allgaier, V. Ansari, C. Eigner, et al. “Streak camera imaging of single photons at telecom wavelength”. *Applied Physics Letters* **112**, 031110 (2018).
- [45] M. Stefszky, R. Ricken, C. Eigner, et al. “Waveguide Cavity Resonator as a Source of Optical Squeezing”. *Physical Review Applied* **7**, (2017).
- [46] M. Stefszky, R. Ricken, C. Eigner, et al. “High-power waveguide resonator second harmonic device with external conversion efficiency up to 75%”. *Journal of Optics* **20**, 065501 (2018).
- [47] R. W. Boyd and B. R. Masters. “Nonlinear Optics, Third Edition”. *Journal of Biomedical Optics* **14**, 029902 (2009).

- [48] B. E. A. Saleh and M. C. Teich. *Fundamentals of Photonics (Wiley Series in Pure and Applied Optics)*. John Wiley & Sons, 1991. ISBN: 0-471-83965-5.
- [49] G. S. Lifante. *Integrated Photonics: Fundamentals*. JOHN WILEY & SONS INC, 2003. 198 pp. ISBN: 0470848685.
- [50] D. C. P. N. Butcher. “The elements of nonlinear optics.” *Crystal Research and Technology* **26**, 802–802 (1991).
- [51] H. Hora. “Y. R. Shen, The Principles of Nonlinear Optics, John Wiley & Sons, New York, 1984, 576 pages.” *Laser and Particle Beams* **4**, 318 (1986).
- [52] W. Voigt. *Lehrbuch der Kristallphysik*. Vieweg+Teubner Verlag, 1966.
- [53] M. M. Fejer, G. A. Magel, D. H. Jundt, and R. L. Byer. “Quasi-phase-matched second harmonic generation: tuning and tolerances”. *IEEE Journal of Quantum Electronics* **28**, 2631–2654 (1992).
- [54] L. E. Myers, R. C. Eckardt, M. M. Fejer, et al. “Quasi-phase-matched optical parametric oscillators in bulk periodically poled LiNbO₃”. *Journal of the Optical Society of America B* **12**, 2102 (1995).
- [55] J. A. Armstrong, N. Bloembergen, J. Ducuing, and P. S. Pershan. “Interactions between Light Waves in a Nonlinear Dielectric”. *Physical Review* **127**, 1918–1939 (1962).
- [56] S. Somekh and A. Yariv. “Phase matching by periodic modulation of the nonlinear optical properties”. *Optics Communications* **6**, 301–304 (1972).
- [57] W. P. Risk, T. R. Gosnell, and A. V. Nurmikko. *Compact Blue-Green Lasers*. CAMBRIDGE UNIV PR, 2003. 552 pp. ISBN: 0521521033.
- [58] C. Canalias, J. Hirohashi, V. Pasiskevicius, and F. Laurell. “Polarization-switching characteristics of flux-grown KTiOPO₄ and RbTiOPO₄ at room temperature”. *Journal of Applied Physics* **97**, 124105–9 (2005).
- [59] M. L. Ouvrard. “Recherches sur les phosphate double de titane, d’étain et de cuivre”. *Comptes Rendus* **111**, 177–179 (1890).
- [60] F. C. Zumsteg, J. D. Bierlein, and T. E. Gier. “K_xRb_{1-x}TiOPO₄: A new nonlinear optical material”. *Journal of Applied Physics* **47**, 4980–4985 (1976).
- [61] R. Masse and J. C. Grenier. “Study of the monophosphates of type M₁TiOpO₄ where M₁=K, Rb and Tl”. *Bulletin de la Société Française de Minéralogie et de Crystallographie* **94**, 437 (1971).
- [62] I. Tordjman, R. Masse, and J. C. Guitel. “Structure cristalline du monophosphate KTiPO₅”. *Zeitschrift für Kristallographie* **193**, 103 (1974).
- [63] N. Hansen, P. Protas, and G. Marnier. “The electron-density distribution in KTiOPO₄”. *Acta Crystallographica, Section B: Structural Science, Crystal Engineering and Materials* **47**, 660 (1991).
- [64] B. V. Andreev, V. A. D’yakov, and N. I. Sorokina. “n-irradiated KTiOPO₄: Precise structure studies”. *Solid State Communications* **80**, 777–903 (1991).

-
- [65] K. Momma and F. Izumi. “VESTA 3 for three-dimensional visualization of crystal, volumetric and morphology data”. *Follow J. Appl. Cryst.* **44**, 1272–1276 (2011).
- [66] J. R. Gandhi, B. Vijayalakshmi, M. Rathnakumari, and P. Sureshkumar. “Growth of Pure and Mo Doped Potassium Titanyl Phosphate (KTP) Crystals: Influence of KTP/Flux Ratios on the Growth Morphology”. *Journal of Minerals & Materials Characterization & Engineering* **10**, 683–691 (2011).
- [67] P. F. Bordui and J. C. Jacco. “Viscosity and density of solutions used in high-temperature solution growth of KTiOPO_4 (KTP)”. *Journal of Crystal Growth* **82**, 351–355 (1987).
- [68] P. Morris, A. Ferretti, J. Bierlein, and G. Loiacono. “Reduction of the ionic conductivity of flux grown KTiOPO_4 crystals”. *Journal of Crystal Growth* **109**, 361–366 (1991).
- [69] V. Kugel, G. Roseman, N. Angert, E. Yaschin, and M. Roth. “Domain inversion in KTiOPO_4 crystal near the Curie point”. *Journal of Applied Physics* **76**, 4823–4826 (1994).
- [70] M. G. Roelofs. “Identification of Ti^{3+} in potassium titanyl phosphate and its possible role in laser damage”. *Journal of Applied Physics* **65**, 4976–4982 (1989).
- [71] A. H. Reshak, I. V. Kityk, and S. Auluck. “Investigation of the Linear and Nonlinear Optical Susceptibilities of KTiOPO_4 Single Crystals: Theory and Experiment”. *The Journal of Physical Chemistry B* **114**, 16705–16712 (2010).
- [72] M. Roth. “Stoichiometry and Domain Structure of KTP-Type Nonlinear Optical Crystals”. In: *Springer Handbook of Crystal Growth*. Springer Berlin Heidelberg, 2010, 691–723.
- [73] C. Canalias. “Domain engineering in KTiOPO_4 ”. QC 20100930. PhD thesis. KTH, Laser Physics, 2005, 108. ISBN: 91-7178-152-8.
- [74] C. Canalias, J. Hirohashi, V. Pasiskevicius, and F. Laurell. “Polarization-switching characteristics of flux-grown KTiOPO_4 and RbTiOPO_4 at room temperature”. *Journal of Applied Physics* **97**, 124105 (2005).
- [75] O. Driesner. “Vergrabene Lichtwellenleiter in Kalium Titanyl Phosphat”. MA thesis. Paderborn University, 2014.
- [76] G. Rosenman, A. Skliar, D. Eger, M. Oron, and M. Katz. “Low temperature periodic electrical poling of flux-grown KTiOPO_4 and isomorphic crystals”. *Applied Physics Letters* **73**, 3650–3652 (1998).
- [77] B.-C. Choi, B. K. Moon, H.-J. Seo, J.-H. Park, and C.-S. Kim. “Impedance spectroscopy of KTiOPO_4 single crystal in the temperature range -100 to 100°C”. *Applied Physics A: Materials Science & Processing* **78**, 745–748 (2004).
- [78] Q. Jiang, M. N. Womersley, P. A. Thomas, et al. “Ferroelectric, conductive, and dielectric properties of KTiOPO_4 at low temperature”. *Physical Review B* **66**, (2002).
- [79] W. Känzig. *Solid State Physics: Advances in Research and Applications, Vol. 4*. Academic Press, 1957. ISBN: 978-0-12-607704-9.
- [80] M. E. Lines and A. M. Glass. *Principles and Applications of Ferroelectrics and Related Materials*. OXFORD UNIV PR, 2001. 696 pp. ISBN: 019850778X.

- [81] M. N. Satyanarayan, A. Deepthy, and H. L. Bhat. “Potassium Titanyl Phosphate and Its Isomorphs: Growth, Properties, and Applications”. *Critical Reviews in Solid State and Materials Sciences* **24**, 103–191 (1999).
- [82] A. Bussmann-Holder and N. Dalal. “Order/Disorder Versus or with Displacive Dynamics in Ferroelectric Systems”. In: *Structure and Bonding*. Springer Berlin Heidelberg, 2006, 1–21.
- [83] J. Valasek. “Piezo-Electric and Allied Phenomena in Rochelle Salt”. *Physical Review* **17**, 475–481 (1921).
- [84] D. Xue and S. Zhang. “The origin of nonlinearity in KTiOPO_4 ”. *Applied Physics Letters* **70**, 943–945 (1997).
- [85] M. Rüsing. “In depth Raman analysis of the ferroelectrics KTiOPO_4 and LiNbO_3 Role of domain boundaries and defects”. PhD thesis. Universität Paderborn, 2018.
- [86] R. A. Stolzenberger and M. P. Sripsick. “Recent advancements in the periodic poling and characterization of RTA and its isomorphs”. In: *Laser Material Crystal Growth and Nonlinear Materials and Devices*. Ed. by K. I. Schaffers and L. E. Myers. SPIE, 1999.
- [87] G. Rosenman, A. Skliar, M. Oron, and M. Katz. “Polarization reversal in crystals”. *Journal of Physics D: Applied Physics* **30**, 277–282 (1997).
- [88] D. R. Allan, J. S. Loveday, R. J. Nelmes, and P. A. Thomas. “A high-pressure structural study of potassium titanyl phosphate (KTP) up to 5 GPa”. *Journal of Physics: Condensed Matter* **4**, 2747–2760 (1992).
- [89] P. A. Thomas, R. Duhlev, and S. J. Teat. “A comparative structural study of a flux-grown crystal of $\text{K}_{0.86}\text{Rb}_{0.14}\text{TiOPO}_4$ and an ion-exchanged crystal of $\text{K}_{0.84}\text{Rb}_{0.16}\text{TiOPO}_4$ ”. *Acta Crystallographica Section B Structural Science* **50**, 538–543 (1994).
- [90] W. Jost. *Diffusion in Solids, Liquids, Gases*. Academic Press, 1952. ISBN: 9780123907509.
- [91] J. Crank. *The Mathematics of Diffusion*. Oxford University Press, 1975. ISBN: 0198533446.
- [92] L. Padberg. “Analysis and optimisation of rubidium in-diffused waveguides in KTP”. MA thesis. Universität Paderborn, 2017.
- [93] G. Hansson, H. Karlsson, S. Wang, and F. Laurell. “Transmission measurements in KTP and isomorphous compounds”. *Applied Optics* **39**, 5058 (2000).
- [94] B. Boulanger, J. P. Fève, G. Marnier, et al. “Relative sign and absolute magnitude of $d^{(2)}$ nonlinear coefficients of KTP from second-harmonic-generation measurements”. *Journal of the Optical Society of America B* **11**, 750 (1994).
- [95] L. K. Cheng, L. T. Cheng, J. Galperin, P. A. M. Hotsenpiller, and J. D. Bierlein. “Crystal growth and characterization of KTiOPO_4 isomorphs from the self-fluxes”. *Journal of Crystal Growth* **137**, 107–115 (1994).
- [96] B. Boulanger, I. Rousseau, J. P. Fève, et al. “Optical studies of laser-induced gray-tracking in KTP”. *IEEE Journal of Quantum Electronics* **35**, 281–286 (1999).
- [97] Q. Zhang, G. Feng, J. Han, et al. “High repetition rate laser pulse induced damage in KTP crystal: Gray-tracking and catastrophic damage”. *Optik - International Journal for Light and Electron Optics* **122**, 1313–1318 (2011).

-
- [98] V. A. Maslov, V. A. Mikhailov, O. P. Shaunin, and I. A. Shcherbakov. “Nonlinear absorption in KTP crystals”. *Quantum Electronics* **27**, 356–359 (1997).
- [99] G. M. Loiacono, D. N. Loiacono, T. McGee, and M. Babb. “Laser damage formation in KTiOPO_4 and KTiOAsO_4 crystals: Grey tracks”. *Journal of Applied Physics* **72**, 2705–2712 (1992).
- [100] M. P. Sripsick, G. J. Edwards, L. E. Halliburton, R. F. Belt, and G. M. Loiacono. “Effect of crystal growth on Ti^{3+} centers in KTiOPO_4 ”. *Journal of Applied Physics* **76**, 773–776 (1994).
- [101] G. J. Edwards, M. P. Sripsick, L. E. Halliburton, and R. F. Belt. “Identification of a radiation-induced hole center in KTiOPO_4 ”. *Physical Review B* **48**, 6884–6891 (1993).
- [102] Y. Zhang, Y. Leng, J. Liu, et al. “Mechanism of hydrogen treatment in KTiOPO_4 crystals at high temperature: experimental and first-principles studies”. *CrystEngComm* **17**, 3793–3799 (2015).
- [103] K. Terashima, M. Takena, and M. Kawachi. “Transparency Improvement of Potassium Titanyl Phosphate (KTP) Crystals by Annealing under Oxygen Atmosphere”. *Japanese Journal of Applied Physics* **30**, 497–499 (1991).
- [104] K. Kato and E. Takaoka. “Sellmeier and thermo-optic dispersion formulas for KTP”. *Applied Optics* **41**, 5040 (2002).
- [105] P. T. Callahan, K. Safak, P. Battle, T. D. Roberts, and F. X. Kärtner. “Fiber-coupled balanced optical cross-correlator using PPKTP waveguides”. *Optics Express* **22**, 9749 (2014).
- [106] J. Chiles, S. Khan, J. Ma, and S. Fathpour. “High-contrast, all-silicon waveguiding platform for ultra-broadband mid-infrared photonics”. *Applied Physics Letters* **103**, 151106 (2013).
- [107] H. Qiao, J. Xu, G. Zhang, et al. “Ultraviolet photorefractivity features in doped lithium niobate crystals”. *Physical Review B* **70**, (2004).
- [108] J. Capmany, V. Bermúdez, and E. Diéguez. “Bulk periodically poled lithium niobate doped with Yb^{3+} ions: Growth and characterization”. *Applied Physics Letters* **74**, 1534–1536 (1999).
- [109] C. Baron, H. Cheng, and M. C. Gupta. “Domain inversion in LiTaO_3 and LiNbO_3 by electric field application on chemically patterned crystals”. *Applied Physics Letters* **68**, 481–483 (1996).
- [110] M. C. Gupta, W. Kozlovsky, and A. C. G. Nutt. “Second-harmonic generation in bulk and waveguided LiTaO_3 with domain inversion induced by electron beam scanning”. *Applied Physics Letters* **64**, 3210–3212 (1994).
- [111] F. Laurell, M. G. Roelofs, W. Bindloss, et al. “Detection of ferroelectric domain reversal in KTiOPO_4 waveguides”. *Journal of Applied Physics* **71**, 4664–4670 (1992).
- [112] H. Karlsson, F. Laurell, and L. Cheng. “Periodic poling of RbTiOPO_4 for quasi-phase matched blue light generation”. *Applied Physics Letters* **74**, 1519–1521 (1999).

- [113] K. Kato and E. Takaoka. “Sellmeier and thermo-optic dispersion formulas for KTP”. *Applied Optics* **41**, 5040–5044 (2002).
- [114] M. Taya, M. C. Bashaw, and M. M. Fejer. “Photorefractive effects in periodically poled ferroelectrics”. *Optics Letters* **21**, 857–859 (1996).
- [115] R. Ricken. *Private Communications*. 2018.
- [116] L. Zhang, P. J. Chandler, P. D. Townsend, Z. T. Alwahabi, and A. J. McCaffery. “Second-harmonic generation in ion-implanted KTiOPO_4 planar waveguides”. *Electronics Letters* **28**, 1478 (1992).
- [117] P. Bindner, A. Boudrioua, J. C. Loulergue, and P. Moretti. “Formation of planar optical waveguides in potassium titanyl phosphate by double implantation of protons”. *Applied Physics Letters* **79**, 2558–2560 (2001).
- [118] T. Doumuki, H. Tamada, and M. Saitoh. “Phase-matched second-harmonic generation in a $\text{Ta}_2\text{O}_5/\text{KTiOPO}_4$ waveguide”. *Applied Physics Letters* **65**, 2519–2521 (1994).
- [119] V. Boutou, A. Vernay, C. Félix, et al. “Phase-matched second-harmonic generation in a flux grown KTP crystal ridge optical waveguide”. *Optics Letters* **43**, 3770 (2018).
- [120] D. Homoelle, S. Wielandy, A. L. Gaeta, N. F. Borrelli, and C. Smith. “Infrared photosensitivity in silica glasses exposed to femtosecond laser pulses”. *Optics Letters* **24**, 1311 (1999).
- [121] F. Laurell, T. Calmano, S. Müller, et al. “Laser-written waveguides in KTP for broadband Type II second harmonic generation”. *Optics Express* **20**, 22308 (2012).
- [122] S. Nolte, M. Will, J. Burghoff, and A. Tuennermann. “Femtosecond waveguide writing: a new avenue to three-dimensional integrated optics”. *Applied Physics A: Materials Science & Processing* **77**, 109–111 (2003).
- [123] S. M. Eaton, H. Zhang, M. L. Ng, et al. “Transition from thermal diffusion to heat accumulation in high repetition rate femtosecond laser writing of buried optical waveguides”. *Optics Express* **16**, 9443 (2008).
- [124] J. D. Bierlein, A. Ferretti, L. H. Brixner, and W. Y. Hsu. “Fabrication and characterization of optical waveguides in KTiOPO_4 ”. *Applied Physics Letters* **50**, 1216–1218 (1987).
- [125] F. Schrepel, T. Opfermann, J.-P. Ruske, U. Grusemann, and W. Wesch. “Properties of buried waveguides produced by He-irradiation in KTP and Rb:KTP”. *Nuclear Instruments and Methods in Physics Research Section B: Beam Interactions with Materials and Atoms* **218**, 209–216 (2004).
- [126] C. Chen, C. E. Rüter, M. F. Volk, et al. “Second harmonic generation of diamond-bladed KTiOPO_4 ridge waveguides”. *Optics Express* **24**, 16434 (2016).
- [127] M. Paturzo. “Investigation of optical birefringence at ferroelectric domain wall in LiNbO_3 by phase-shift polarimetry”. *Applied Physics Letters* **88**, 151918 (2006).
- [128] S. Hofmann. “Sputter-depth profiling for thin-film analysis”. *Philosophical Transactions of the Royal Society A: Mathematical, Physical and Engineering Sciences* **362**, 55–75 (2004).

-
- [129] U. Littmark and K. G. Tschersich. “All about SIMS: Secondary Ion Mass Spectrometry. Basic Concepts, Instrumental Aspects, Applications and Trends. Von A. Benninghoven, F. G. Rüdener und H. W. Werner. John Wiley”. *Nachrichten aus Chemie, Technik und Laboratorium* **35**, 1262–1262 (1987).
- [130] J. I. Goldstein, D. E. Newbury, P. Echlin, et al. *Scanning Electron Microscopy and X-ray Microanalysis*. Springer US, 2003.
- [131] M. Minsky. “Memoir on inventing the confocal scanning microscope”. *Scanning* **10**, 128–138 (1988).
- [132] *AgCu-elastomer constant conductive elastomer*. Datasheet. Micro Tech Components GmbH, 2013.
- [133] K.-H. Luo, V. Ansari, M. Massaro, et al. “Counter-propagating photon pair generation in a nonlinear waveguide”. *in preparation*, (2019).
- [134] L. Limited. *Datasheet SF1*. 2018.
- [135] J. C. Jacco and G. M. Loiacono. “Nature of the infrared spectrum in band-edge region of KTiOPO_4 ”. *Applied Physics Letters* **58**, 560–561 (1991).
- [136] L. K. Cheng, J. D. Bierlein, and A. A. Ballman. “Crystal growth of KTiOPO_4 isomorphs from tungstate and molybdate fluxes”. *Journal of Crystal Growth* **110**, 697–703 (1991).
- [137] R. Sole, X. Ruiz, R. Cabre, et al. “ KTiOPO_4 single crystals grown from neodymium modified fluxes”. *Journal of Crystal Growth* **167**, 681–685 (1996).
- [138] C. Eigner. “Periodically Poled Waveguides in Potassium Titanyl Phosphate for Applications in Quantum Optics”. Master Thesis. Paderborn University, 2013.
- [139] J. Hirohashi, K. Yamada, H. Kamio, and S. Shichijyo. “Embryonic Nucleation Method for Fabrication of Uniform Periodically Poled Structures in Potassium Niobate for Wavelength Conversion Devices”. *Japanese Journal of Applied Physics* **43**, 559–566 (2004).
- [140] H. F. Wang, Y. Y. Zhu, S. N. Zhu, and N. B. Ming. “Investigation of ferroelectric coercive field in LiNbO_3 ”. *Applied Physics A: Materials Science & Processing* **65**, 437–438 (1997).
- [141] M. Santandrea, M. Stefszky, V. Ansari, and C. Silberhorn. “Fabrication limits of waveguides in nonlinear crystals and their impact on quantum optics applications”. *arxiv.org*, (2018).
- [142] C. Eigner, L. Padberg, M. Santandrea, and C. Silberhorn. “Patent - Herstellung von Wellenleitern aus Materialien der KTP-Familie”. Az. 10 2018 108 636.9. 2018.
- [143] P. Mackwitz. “Nonlinear analysis of periodically poled waveguides in KTP: A fundamental study”. MA thesis. Paderborn University, 2017.
- [144] L. Martinu and D. Poitras. “Plasma deposition of optical films and coatings: A review”. *Journal of Vacuum Science & Technology A: Vacuum, Surfaces, and Films* **18**, 2619–2645 (2000).
- [145] B. Rauschenbach and J. W. Gerlach. “Texture Development in Titanium Nitride Films Grown by Low-Energy Ion Assisted Deposition”. *Crystal Research and Technology* **35**, 675–688 (2000).

- [146] K. Wasa. *Handbook of Sputter Deposition Technology: Fundamentals and Applications for Functional Thin Films, Nano-Materials and Mems*. WILLIAM ANDREW INC, 2012. 660 pp. ISBN: 1437734839.
- [147] H. Eberhardt. *Hochvakuumbeschichtungsanlage M700 - Anlagenaufbau*. Marquis Automatisierungstechnik GmbH. 2014.
- [148] A. Eckstein, B. Brecht, and C. Silberhorn. “A quantum pulse gate based on spectrally engineered sum frequency generation”. *Optics Express* **19**, 13770 (2011).
- [149] B. Brecht, A. Eckstein, A. Christ, H. Suche, and C. Silberhorn. “From quantum pulse gate to quantum pulse shaper - engineered frequency conversion in nonlinear optical waveguides”. *New Journal of Physics* **13**, 065029 (2011).
- [150] S. Dwyer, L. Barsotti, S. S. Y. Chua, et al. “Squeezed quadrature fluctuations in a gravitational wave detector using squeezed light”. *Optics Express* **21**, 19047 (2013).
- [151] K. Tsuzuki, Y. Shibata, N. Kikuchi, et al. “Full C-Band Tunable DFB Laser Array Copackaged With InP Mach-Zehnder Modulator for DWDM Optical Communication Systems”. *IEEE Journal of Selected Topics in Quantum Electronics* **15**, 521–527 (2009).
- [152] T. Umeki, O. Tadanaga, and M. Asobe. “Highly Efficient Wavelength Converter Using Direct-Bonded PPZnLN Ridge Waveguide”. *IEEE Journal of Quantum Electronics* **46**, 1206–1213 (2010).
- [153] J.-H. Zhao, X.-F. Qin, F.-X. Wang, et al. “Thermal annealing property of KOTiPO_4 planar and ridge waveguides formed by MeV Si ion implantation”. *Optical Materials Express* **3**, 426 (2013).
- [154] M. F. Volk, C. E. Rüter, and D. Kip. “Rb/Ba side-diffused ridge waveguides in KTP”. *Optics Express* **25**, 19872 (2017).
- [155] J. J. Carvajal, P. Segonds, A. Pena, et al. “Structural and optical properties of $\text{RbTiOPO}_4\text{:Nb}$ crystals”. *Journal of Physics: Condensed Matter* **19**, 116214 (2007).
- [156] R. G. Hunsperger. *Integrated Optics: Theory and Technology*. Springer Berlin Heidelberg, 1982.
- [157] R. Regener and W. Sohler. “Loss in low-finesse Ti:LiNbO_3 optical waveguide resonators”. *Applied Physics B Photophysics and Laser Chemistry* **36**, 143–147 (1985).
- [158] A. Arie, G. Rosenman, V. Mahal, et al. “Green and ultraviolet quasi-phase-matched second harmonic generation in bulk periodically-poled KTiOPO_4 ”. *Optics Communications* **142**, 265–268 (1997).
- [159] I. Shoji, T. Kondo, A. Kitamoto, M. Shirane, and R. Ito. “Absolute scale of second-order nonlinear-optical coefficients”. *Journal of the Optical Society of America B* **14**, 2268 (1997).
- [160] K. S. Buritskii, E. M. Dianov, V. A. Maslov, V. A. Chernykh, and E. A. Scherbakov. “Nonlinear directional coupler based on Rb:KTP-waveguides”. *Applied Physics B Photophysics and Laser Chemistry* **54**, 167–169 (1992).

-
- [161] M. A. Butt, R. Sole, M. C. Pujol, et al. “Fabrication of Y-Splitters and Mach-Zehnder Structures on (Yb,Nb):RbTiOPO₄ Epitaxial Layers by Reactive Ion Etching”. *Journal of Lightwave Technology* **33**, 1863–1871 (2015).
- [162] M. Rottschalk, J.-P. Ruske, B. Unterschütz, A. Rasch, and V. Gröber. “Single mode integrated-optical wide-band channel waveguides and junction splitters in KTiOPO₄ for visible light”. *Journal of Applied Physics* **81**, 2504–2510 (1997).
- [163] K. Laiho, K. N. Cassemiro, D. Gross, and C. Silberhorn. “Probing the Negative Wigner Function of a Pulsed Single Photon Point by Point”. *Physical Review Letters* **105**, (2010).
- [164] S. Müller, T. Calmano, P. W. Metz, et al. “Highly efficient continuous wave blue second-harmonic generation in fs-laser written periodically poled Rb:KTiOPO₄ waveguides”. *Optics Letters* **39**, 1274 (2014).
- [165] R. Machulka, J. Svozilik, J. Soubusta, J. Perina, and O. Haderka. “Spatial and spectral properties of fields generated by pulsed second-harmonic generation in a periodically poled potassium-titanyl-phosphate waveguide”. *Physical Review A* **87**, (2013).
- [166] A. Zukauskas, V. Pasiskevicius, and C. Canalias. “Second-harmonic generation in periodically poled bulk Rb-doped KTiOPO₄ below 400 nm at high peak-intensities”. *Optics Express* **21**, 1395 (2013).
- [167] L. Cai, Y. Wang, and H. Hu. “Low-loss waveguides in a single-crystal lithium niobate thin film”. *Optics Letters* **40**, 3013 (2015).
- [168] M. Zhang, C. Wang, R. Cheng, A. Shams-Ansari, and M. Lončar. “Monolithic ultra-high-Q lithium niobate microring resonator”. *Optica* **4**, 1536 (2017).